Evapotranspiration of Hawaiʻi
Final Report

Thomas W. Giambelluca[1], Xiufu Shuai[1], Mallory L. Barnes[2], Randall J. Alliss[3],
Ryan J. Longman[1], Tomoaki Miura[2], Qi Chen[1], Abby G. Frazier[1], Ryan G. Mudd[1],
Lan Cuo[4], and Aaron D. Businger[1]

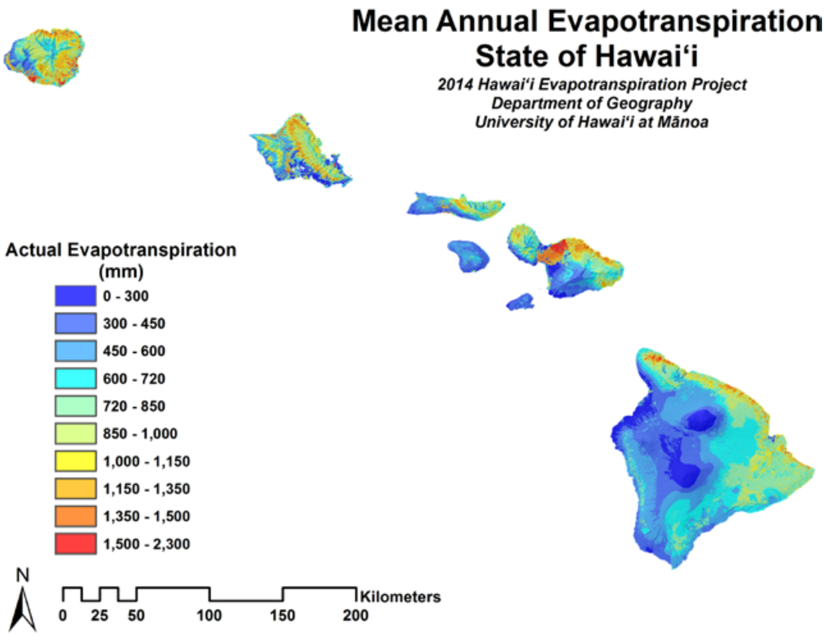

[1]Department of Geography, University of Hawaiʻi at Mānoa, Honolulu, HI, USA; [2]Department of Natural Resources and Environmental Managment, University of Hawaiʻi at Mānoa, Honolulu, HI, USA; [3]Northrop Grumman Corporation, Chantilly, VA, USA; [4]Institute for Tibetan Plateau Research, Chinese Academy of Sciences, Beijing, China

Submitted to

U.S. Army Corps of Engineers – Honolulu District
and
Commission on Water Resource Management, State of Hawaiʻi

February 2014

Acknowledgements

The Hawaiʻi Evapotranspiration Project was conducted under an agreement between the State of Hawaiʻi Commission on Water Resource Management and the U.S. Army Corps of Engineers, Honolulu District under Section 22 of the Water Resources Act of 1974. Written Agreement No. W9128A-08-D-0007 between the U.S. Army Corps of Engineers and CH2M Hill, Inc., included a task subcontracted to the Department of Geography, University of Hawaiʻi to develop evapotranspiration maps for the State of Hawaiʻi. This project was facilitated through the assistance of numerous individuals and organizations. Please see the "People" tab of the Evapotranspiration of Hawaiʻi web site for information about those who contributed to this work. We are grateful to those listed there, as well as many other individuals who contributed to Hawaiʻi's climate dataset by making and recording measurements and maintaining the data.

We thank Brett Holben and his staff for establishing and maintaining the two AeroNet sites used in this study, Christian Gueymard for providing us with an updated version of the REST2 model and for assistance in quantifying model input variables specific to Hawaii, Robert Evans of the National Oceanic and Atmospheric Administration (NOAA) for the ozone values required for the REST2 model, Jesse Acosta of the State of Hawaiʻi Division of Forestry and Wildlife for helping to maintain the RAWS network in Hawaiʻi, the Western Regional Climate Center for providing access to the RAWS climate database, and the National Renewable Energy Laboratory (NREL) Measurement and Instrument Data center (MDIC) for the use of their solar data. We are grateful to Chunxi Zhang of the International Pacific

Research Center, University of Hawaiʻi at Mānoa, for providing his 1-km albedo analysis of Hawaiʻi. We thank Lloyd Hihara and Ryan Sugamoto for providing leaf wetness data obtained under the Pacific Rim Environmental Degradation of Materials Research Program, sponsored by the U.S. Army RDECOM-ARDEC, and the Atmospheric Corrosion Research in Hawaiʻi Microclimates project, sponsored by Mandaree Enterprise Corporation and the Office of the U.S. Undersecretary of Defense. We acknowledge support for the development of digital air temperature and relative humidity maps conducted under the Pacific Rim Corrosion Research Program (Lloyd Hihara, PI), funded by the U.S. Department of Defense. We also thank Ray Anderson, of the U.S.D.A. Agricultural Research Service, Riverside, CA, and his colleagues for providing eddy covariance measurements of *ET* from the Hawaiʻi Commercial and Sugar Company plantation on Maui.

Lastly, we thank Delwyn Oki, John Engott, Adam Johnson, and Maoya Bassiouni of the Pacific Island Water Science Center, U.S. Geological Survey, Neal Fujii, Commission on Water Resource Management, State of Hawaiʻi, and Debbie Solis and Michael Wong, U.S. Army Corps of Engineers, Honolulu District, for providing highly valuable comments and suggestions on a draft version of this report.

Table of Contents

List of Figures

List of Tables

INTRODUCTION

Estimating the amount, spatial patterns, and temporal variability of evapotranspiration (ET) is necessary for many hydrological and ecological applications. Some examples of these applications are: assessment of water resource availability and management of water resources, analysis of streamflow and groundwater flow and their responses to climate variability and land cover change, and planning conservation activities to restore and preserve native ecosystems. Several efforts have been made to map the spatial patterns of potential ET (PET) and ET in Hawaiʻi. For example, patterns of mean annual pan evaporation were mapped for several islands by Ekern and Chang (1985). ET estimates based on water balance modeling have been done for portions of the State, including Southern Oʻahu (Giambelluca 1983), Oʻahu Island (Shade and Nichols 1996), North Kohala (Oki 2002), Hawaiʻi Island (Engott 2011), and the Līhuʻe Basin on Kauaʻi (Izuka et al. 2005). However, prior to this study, no effort had been made to develop a comprehensive analysis of the patterns of mean ET of the State of Hawaiʻi.

The Penman-Monteith equation (Monteith 1965) is widely used to estimate ET:

$$\lambda E_{Penman-Monteith} = \frac{sA + \frac{\rho_a C_p (e_{sat} - e)}{r_a}}{s + \gamma\left(1 + \frac{r_c}{r_a}\right)} \tag{1}$$

where λE is the latent heat flux equivalent of ET (W m^{-2}), s is slope of saturation vapor pressure versus temperature curve (mb K^{-1}), A is available energy (net radiation minus heat storage in the soil, biomass, and air layer below the reference height) (W m^{-2}), ρ_a is air density (kg m^{-3}), C_p is specific heat of air at constant pressure (J K^{-1} kg^{-1}), r_a is aerodynamic resistance (s m^{-1}), e_{sat} is saturation vapor pressure (mb), e is ambient vapor pressure (mb), γ is the psychrometric constant (mb K^{-1}), and r_c is the canopy resistance to water vapor transfer (s m^{-1}). To obtain ET in water units (mm), λE derived in Eq. (1) can be multiplied by $^{n}/_{(\lambda \cdot \rho_w)}$, where n is the number of seconds in the relevant time period, λ is the latent heat of vaporization of water (J kg^{-1}), and ρ_w is the density of water (kg m^{-3}) at the relevant temperature.

In this study, the Penman-Monteith approach was used to estimate ET with a range of input datasets and estimation techniques employed to provide the necessary input data.

METHODS

The bulk of the work in this study involved the development, implementation, and testing of methods to estimate spatially dependent (250-m resolution) and temporally dependent (for each month, 24 hourly values representing the mean diurnal cycle) maps of each input variable needed to estimate ET by the Penman-Monteith method. Below, the datasets, and methods used to estimate the parameters and time-dependent variables in Eq. (1) are described.

Datasets

The following is a brief summary of the numerous existing datasets used to conduct this study.

Meteorological Data

For a variety of purposes in this study, especially model development and testing, it was necessary to use ground-based measurements of meteorological variables. All available data were utilized. However, in most cases, a subset of observation sites was excluded from the model development (calibration) phase, and used only for model testing (validation). The meteorological station data come from various sources, including HaleNet (Haleakalā Climate Network; http://climate.socialsciences.hawaii.edu/HaleNet), HavoNet (Hawaiʻi Volcanoes National Park Network), RAWS (Remote Automatic Weather Stations; http://raws.fam.nwcg.gov), NREL (National Renewable Energy Laboratory; http://www.nrel.gov), and NCDC (National Climatic Data Center; http://www.ncdc.noaa.gov). Appendix Table A1 lists the meteorological stations used in calibrating the air temperature model in this study. Appendix Table A2 lists all other meteorological stations used in this study for calibration and validation purposes. Figures 1 and 2 show the locations of the stations. Appendix Tables A3 and A4 identify which stations were used for model development and validation for each variable.

Mean wind speed maps developed by AWS Truewind (2004) were obtained via the Hawaiian Electric Company web site (http://www.heco.com/portal/site/heco/menuitem.508576f78baa14340b4c0610c510b1ca/?vgnextoid=596c5e658e0fc010VgnVCM1000008119fea9RCRD).

Mean monthly rainfall maps used in this study were from the Rainfall Atlas of Hawaiʻi (Giambelluca et al. 2013; http://rainfall.geography.hawaii.edu). The air temperature model, which was developed several years before the start of this study and prior to the completion of the revised Rainfall Atlas of Hawaiʻi, utilized mean monthly rainfall maps from the original Rainfall Atlas of Hawaiʻi (Giambelluca et al. 1986).

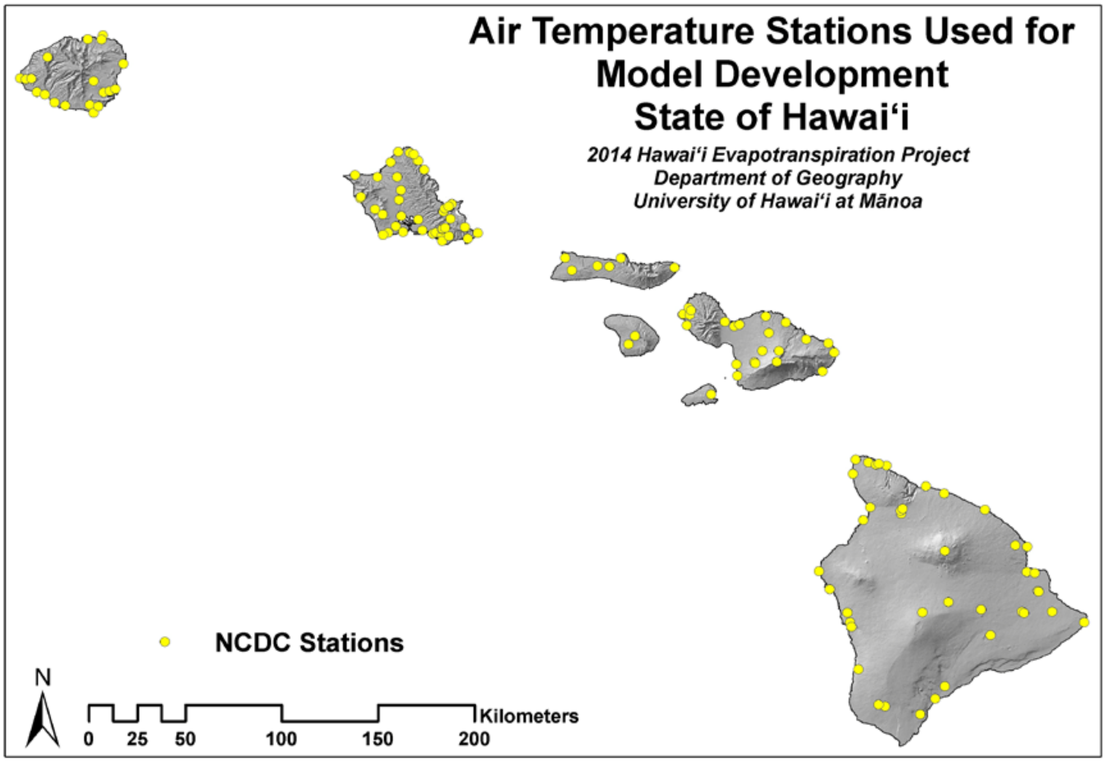

Figure 1. National Climatic Data Center (NCDC) stations used for air temperature model development.

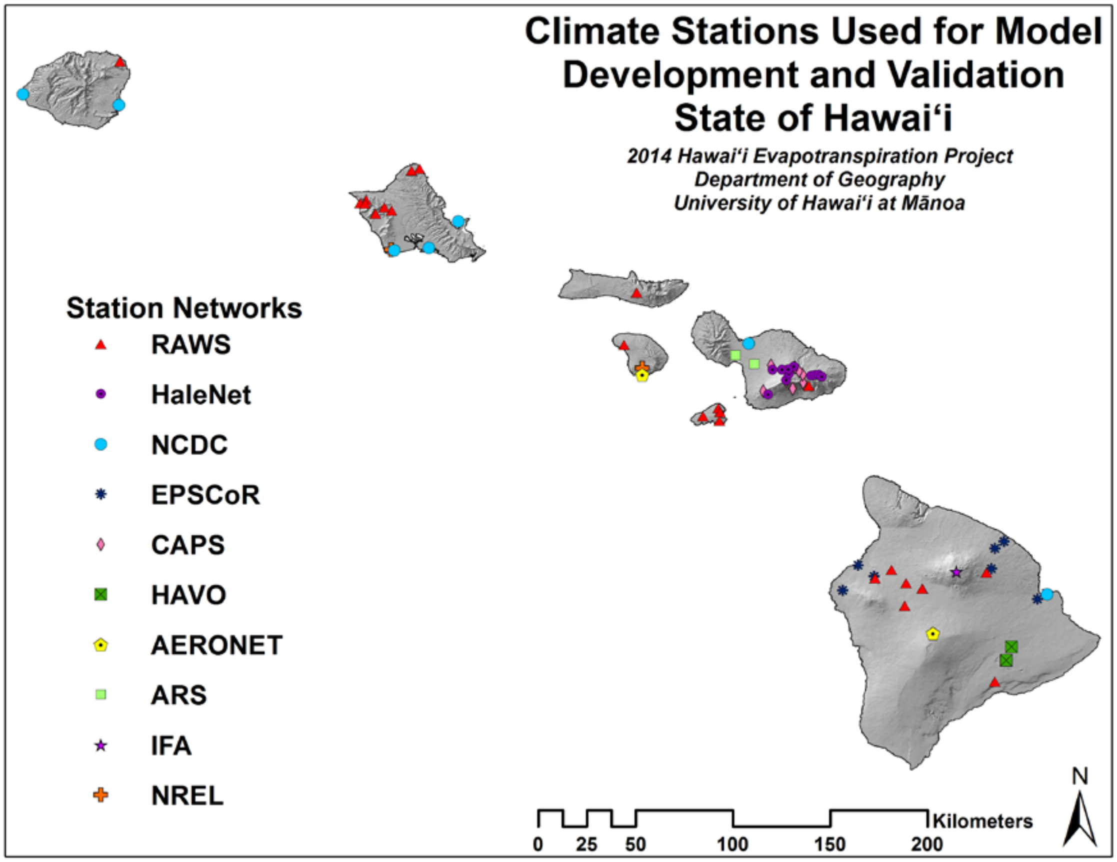

Figure 2. Climate stations used for model development and calibration.

Cloud Cover Data

The high spatial resolution MODIS (Moderate-resolution Imaging Spectroradiometer) cloud mask products MOD35 and MYD35 and high temporal resolution GOES (Geostationary Operational Environmental Satellite) imagery were used to estimate patterns of cloud frequency for Hawaiʻi.

Land Cover Characteristics

The 30-m resolution land cover characteristics, EVT (existing vegetation type) and EVH (existing vegetation height), were obtained from the 2008 version of the LANDFIRE database (Comer et al. 2003; http://landfire.gov). The EVT data set defines the spatial distribution of land cover in terms of Hawaiʻi-specific land cover types (Appendix Table A5). All agricultural areas were lumped into a single land cover category in the LANDFIRE classification. To allow more specific parameterization of some of the major agricultural crops in Hawaiʻi, agricultural areas were scrutinized using GoogleEarth (http://www.google.com/earth). Because of their distinctive appearance, it was possible to identify sugarcane, pineapple, macadamia nut, coffee, and wetland taro cultivation areas, and to differentiate them into separate land cover classes. The remaining agricultural areas were combined under "mixed agriculture" including fruit orchards, vegetables, flowers, and other crops. Significant areas on Maui identified as agricultural land in the LANDFIRE classification have since been abandoned. These areas were reclassified as Hawaiian Introduced Perennial Grassland. Additionally, because the invasive tree *Prosopis pallida* (kiawe) is known to be phreatophytic (extends roots into the saturated zone to access groundwater directly for transpiration) in dry coastal areas of Hawaiʻi, areas of coastal kiawe were estimated. For each 250-m cell classified as Hawaiian Introduced Dry Forest in the LANDFIRE classification, the number of 30-m DEM cells with an elevation of 12 m or less was counted. These 30-m cells were assumed to represent areas of coastal kiawe acting as phreatophytes. The relative number of these cells in each 250-m cell was determined. In subsequent transpiration estimates, water accessibility for the portion of each cell estimated to be coastal kiawe was increased (Figure 3). The land cover map used for this study is shown in Figure 4.

For the albedo analysis, which was done early in the project, a previous version of the land cover analysis, HIGAP (Gon, III et al. 1999; http://gis1.usgs.gov/csas/gap/viewer/land_cover/Map.aspx), was used. The HIGAP land cover analysis was mapped at 30-m resolution and used a land cover classification similar to that of the LANDFIRE analysis. The HIGAP land cover classes are given in Appendix Table A6.

Terra and Aqua MODIS daily Surface Reflectance data (MOD09GA and MYD09GA, respectively) were obtained for the period July 2002 through March 2009, screened for cloud contamination, and reduced to daily normalized difference vegetation index (*NDVI*) and enhanced vegetation index values (Huete et al., 2002), which were then temporally composited into mean monthly *NDVI* and *EVI* maps with the mean compositing technique (Vancutsem et al., 2007).

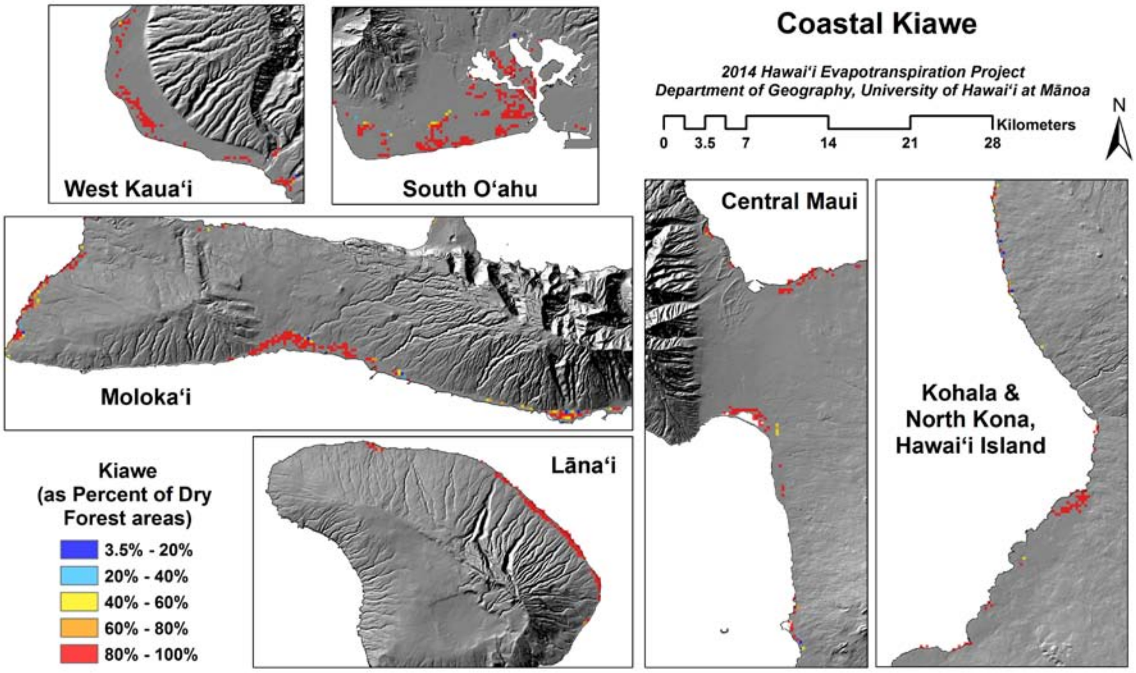

Figure 3. Selected areas of Hawaiʻi showing the percentage of each map pixel with coastal kiawe.

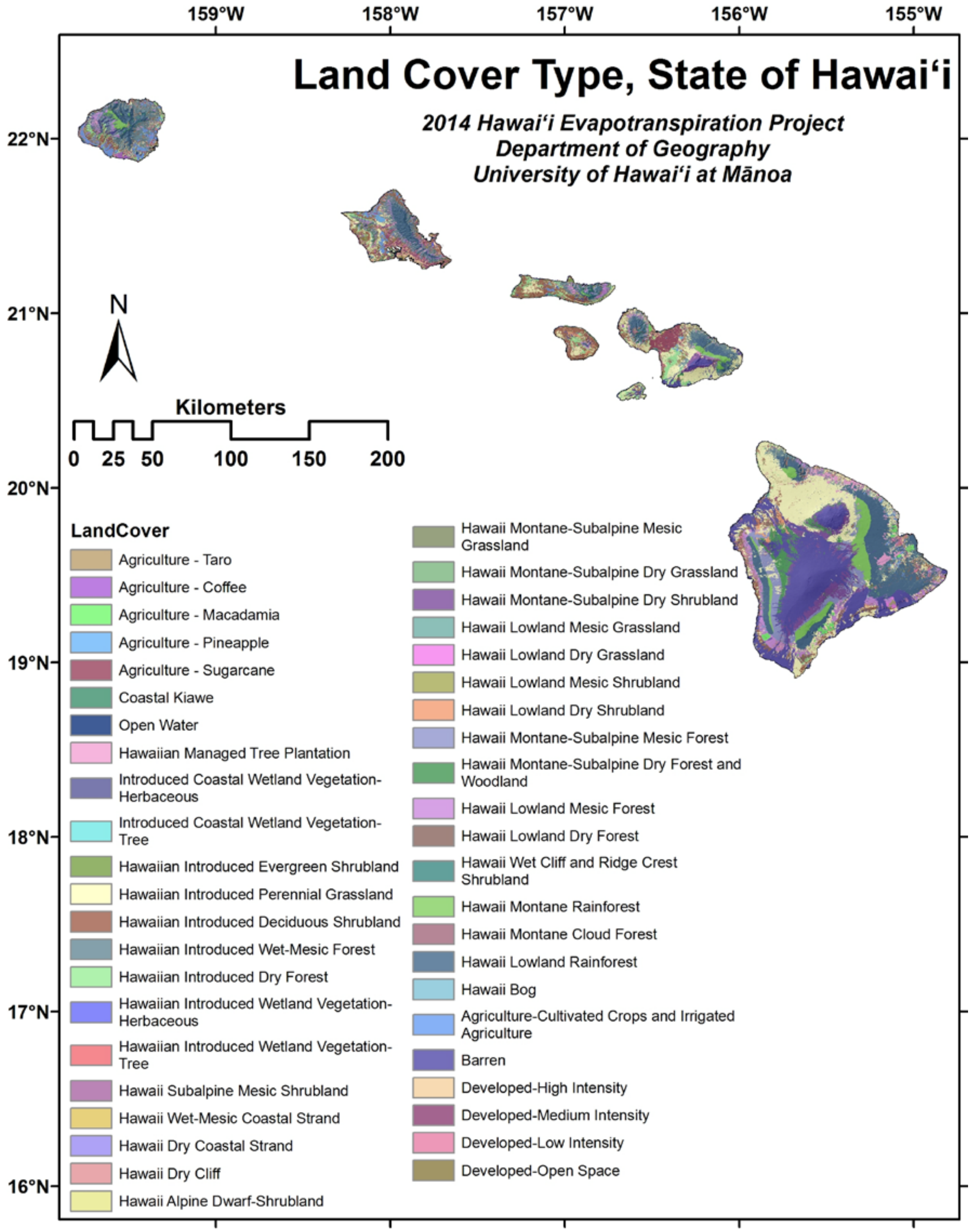

Figure 4. Land cover of the Hawaiian Islands, adapted from Comer et al. (2003; http://landfire.gov)

MODIS 4-day 1-km leaf area index (*LAI*) data (MCD15A3) were obtained for the period July 2002 and December 2012, and processed into *LAI* time series data at 4-

day intervals over the major Hawaiian islands (Yang et al., 2006). The 4-day time series were then averaged across years over every month to generate mean monthly *LAI* data.

The MODIS Filled Surface Albedo Product (derived from MOD43B3; http://modis-atmos.gsfc.nasa.gov/ALBEDO/) is available every 16 days at a 1-km resolution for cloud-free pixels. Chunxi Zhang (IPRC, University of Hawaiʻi at Mānoa, pers. comm.) compiled MODIS surface albedo data for Hawaiʻi for the period 2000-2004 to produce 1-km mean monthly albedo maps and provided them to this project for further analysis.

Base Periods of Data Used in Model Development and Validation

Whenever possible, data were obtained covering a sufficient time period to make reasonable estimates of the mean annual cycle (monthly means) or the mean diurnal cycle (mean hourly values for the diurnal cycle of each month or of the whole year). Appendix Table A7 shows the mean start, end, and mid-point of data used to develop and validate the models to estimate variables required in this study. In general, data were selected for approximately the decade 2001-2010 (see Appendix Table A7), but this differed from variable to variable according to data availability. For the mean monthly air temperature and relative humidity analyses, which were done several years prior to the start of this project and made use of all readily available data at the time, the data were mostly from periods before the early 2000s. For example, the periods of record of the monthly data used had an average range of March 1957 to January 1981 for temperature and February 1985 to January 2003 for relative humidity (Appendix Table A7). No data manipulations were done to adjust data to a common base period.

Available Energy

Available energy, A (W m^{-2}) is estimated as:

$$A = R_{net} - G - Q_b - Q_a \tag{2}$$

where R_{net} is net radiation, G is the change in sensible heat stored in the soil, Q_b is the change in sensible heat stored in the aboveground biomass, and Q_a is the change in sensible heat stored in the air layer below the reference level. All variables are in units of W m^{-2}.

Net Radiation

Net radiation R_{net} (W m^{-2}) is defined as:

$$R_{net} = K_{down} - K_{up} + L_{down} - L_{up} \tag{3}$$

where K_{down} is incident solar (shortwave) radiation, K_{up} is reflected shortwave radiation, L_{down} is down-welling longwave radiation absorbed by the surface, and L_{up} is upward longwave radiation emitted by the surface. All variables are in units of W m^{-2}.

Solar Radiation

To estimate *ET* accurately across the Hawaiian Islands, it is fundamentally important to obtain reliable estimates of the spatial patterns of solar radiation as it varies through the diurnal (24-hour) and annual (12-month) cycles. Observations of solar radiation are restricted to a relatively few locations. Hence, it was necessary to model this variable. To do so, we first estimated clear-sky radiation, i.e., the solar radiation under cloudless conditions. The clear-sky estimate was then adjusted for the effects of cloudiness (described later). Clear-sky radiation is related to sun angle and atmospheric transparency. Sun angle depends primarily on geographical location, time of day, and time of year; while atmospheric optical properties determine its transparency.

Clear-sky Solar Radiation Model

The REST2 clear-sky radiation model (Gueymard, 2008) was used to estimate the spatial pattern of solar radiation in the absence of clouds for each hour of the diurnal cycle for each month. The model estimates clear-sky radiation based on the cosine-adjusted extraterrestrial radiation (ETR) reaching the earth, and the estimated attenuation of incoming shortwave radiation as a function of optical path length and atmospheric optical properties. ETR and optical path length are determined by latitude, longitude, time of day, time of year, the geometry and timing of Earth's rotation, orbit, and the variation in the angle between the Earth's rotational axis and the plane of the ecliptic. In addition to solar geometry, the model inputs include atmospheric pressure, column water vapor, column ozone amount, column nitrogen dioxide (NO_2) amount, the two Ångström coefficients that describe the atmospheric turbidity due to aerosols, the aerosol single scattering albedo, and the far-field ground albedo.

The REST2 code was used to model hourly clear-sky solar radiation at a 250-m resolution for the State of Hawaiʻi. Hourly values were computed as the average of 60 one-minute instantaneous REST2 model estimates. In previous studies, Longman et al. (2012; 2013) used clear-sky models to accurately predict solar radiation at a range of elevations in Hawaiʻi. Their analysis showed that horizontal variation in atmospheric parameters is negligible in Hawaiʻi. Differences in optical path length cause significant vertical changes in atmospheric attenuation. Therefore, representation of spatial variations in atmospheric parameter values in the model is based solely on elevation. Aerosol optical depth, column water vapor (precipitable water) and the Ångström exponent were interpolated vertically from values measured at two AERONET sites, Lānaʻi (20 m elevation) and Mauna Loa (3397 m) (Longman et al. 2012). The spatial pattern of w, assumed constant at any location, was estimated on the basis of its vertical profile. Longman (2012) integrated radiosonde observations over Hawaiʻi to estimate the mean vertical profile, which can be represented by the following third-order polynomial:

$$w = c_0 + c_1 \cdot P + c_2 \cdot P^2 + c_3 \cdot P^3 \tag{4}$$

where c_0 = -1.342063, c_1 = 7.661469E-5, c_2 = -1.652886E-9, c_3 = 1.314835E-14, and P is atmospheric pressure (Pa), estimated as a function of elevation:

$$P = \frac{P_0}{e^{\frac{z}{8500}}} \tag{5}$$

where P_0 is sea level pressure (assumed equal to 101,500 Pa), and z is elevation (m). Ozone optical depth data were obtained for a Dobson Ozone Spectrometer operated at Mauna Loa Observatory (NOAA 2011). Following Gueymard (2012), NO_2 was set to 0.1 DU, and the single scattering albedo was fixed at 0.95 (below 0.7 μm) and 0.9 (above 0.7 μm).

In this study we use temporally averaged parameter values (from approximately November 2004-February 2007 for precipitable water and July 1995-August 2007 for aerosol optical depth and the Angström exponent; see Appendix Table A7) as model inputs for estimating clear sky radiation. Longman et al. (2012) previously analyzed the effects of temporal averaging of model atmospheric transmission parameters and showed that holding parameter settings at their mean annual value gave better results than using temporally varying (daily or monthly) parameter estimates for prediction of clear-sky radiation at a range of elevations in Hawaiʻi.

Cloud Frequency Analysis

Clouds are the major factor influencing solar radiation at any location on the earth's surface. The MODIS (Moderate-resolution Imaging Spectroradiometer) instruments aboard the Terra and Aqua satellites provide observations with the high spatial resolution necessary to determine patterns of cloud cover over the Hawaiian Islands. Each satellite makes two overpasses each per day (mean overpass times: Terra 11:10 and 22:40 HST; Aqua 13:50 and 2:20). The cloud mask products MOD35 and MYD35 provide cloud likelihood estimates in four confidence intervals: "confident cloudy", "probably cloudy", "probably clear", and "confident clear". Generation of cloud monthly frequency statistics was performed using an algorithm that determined whether a pixel was cloudy or clear using a combination of the MODIS cloud mask confidence levels, quality assessment flags, and other indicators. The MODIS cloud mask product is clear-sky conservative to minimize false clear occurrences. Therefore, obtaining an unbiased cloudiness estimate requires extensive processing (Ackerman et al. 2002, Ackerman et al. 2008). The methods used in this study are based on suggestions in the MODIS User's Guide for isolating cloudy scenes (Strabala 2005, Ackerman et al. 2002). The four MODIS cloud mask confidence levels were condensed into a binary designation: cloudy (1) or clear (0).

For daytime overpasses, pixels with ‘confident cloudy’ or ‘probably cloudy’ designations were considered cloudy, and confident clear and probably clear pixels were considered clear. Pixels flagged as sunglint regions and those with low confidence MODIS Quality Assurance flags were excluded. For a complete description of the MODIS cloud analysis, see Barnes (2013).

Using the same algorithm for nighttime data resulted in systematic overestimation of cloud occurrence over the land. False cloud detection at nighttime using solely infrared data is a known problem with the MODIS cloud mask product that, in previous studies of clouds in Hawaii, has resulted in the inability to accurately assess nighttime cloud cover (Yang et al. 2008a, b). The problem of false nighttime cloud detection is especially prevalent for land areas with elevations up to 2000 m. This false cloud detection occurs as a result of errors in the surface temperature test that compares gridded surface air temperatures from Global Data Assimilation System (GDAS) to satellite-observed 11-μm brightness temperatures at elevations up to 2000 m (Frey et al. 2008). This test does not necessarily perform well in mountainous regions with high spatial variability in nighttime surface temperature. Following recommendations of the MODIS cloud mask team, the nighttime algorithm was changed so that only the pixels designated “confident cloudy” were considered cloudy and pixels in all three other categories were considered clear. Additionally, if the surface temperature test was the only one of five tests performed designating the pixel cloudy, the pixel was considered clear. These changes significantly reduced false cloud detection over land at elevations up to 2000 m.

This approach was applied estimate mean monthly cloud frequency for each over pass time by averaging results from 2001-2011 for Terra-MODIS and from 2003-2011 for Aqua-MODIS.

A second satellite-based cloud analysis was also developed using multi-spectral imagery available from the National Oceanic and Atmospheric Administration (NOAA) Geostationary Operational Environmental Satellite (GOES) 8-15 satellites. Imagery was collected and archived for the Hawaiian Islands at 4-km, 15-min (time) resolution for the period 2001-2011. Cloud detection was based on the contrast in observed emitted and/or reflected radiation compared with a computed clear sky background (CSB) value, defined as the satellite-observed radiation emitted and/or reflected from the surface when no clouds are present, for each pixel. The CSB varies spatially and temporally and is influenced by the radiative properties of the surface, surface temperature, terrain height, soil moisture, and solar illumination angle. Because of these variations, the CSB was calculated for each pixel, for different times of day, and for each band, and was updated continuously through time. CSB was estimated for albedo (visible), reflectivity (shortwave infrared, SWIR), longwave infrared (LWIR) emission, and the fog product (bi-spectral difference variable). For each of the four variables, CSB was calculated for each pixel by averaging values for high-probability clear times over the previous 30 days at a given analysis time (e.g., 1400 UTC). Clear times were determined not only from the satellite imagery, but also ancillary observations, including those from the telescope observatory on the Haleakalā summit, Maui. Comparing satellite images with CSB values for the different spectral products, four tests of cloud presence were done, with the results combined to produce a composite probability of cloud occurrence for each pixel. The pixel was set to cloud when the estimated cloud probability exceeded 50%. The cloud algorithm was run on the entire satellite archive, consisting of nearly 500,000 images over the 2001-2011 study period.

The results of the MODIS and GOES analyses were mean cloud frequency maps, 4 times per day for each month at 1-km resolution (MODIS) and hourly (24 times per day) for each month at 4-km resolution (GOES). A method was developed to fuse the two sources of cloud cover information to exploit the advantages of high spatial resolution MODIS cloud data with high temporal resolution GOES data to produce 1-km resolution, 1-hour cloud frequency ($CF_{x,y,t}$) values for each hour of the mean diurnal cycle of each month:

$$CF_{i,j,t} = \left[\frac{interp(MODIS(x,y,i,j))}{interp(GOES(x,y,i,j))}\right] \cdot GOES(x,y,i,j) \tag{6}$$

where *interp(MODIS(x,y,i,j))* is the cloud frequency value for hour *i* and month *j* at the 1-km pixel (*x,y*) derived by temporal linear interpolation of MODIS cloud frequency between the most recent and next overpass times, *interp(GOES(x,y,i,j))* is the cloud frequency value for hour *i* and month *j* at a 1-km pixel (*x,y*) derived by temporal linear interpolation of GOES cloud frequency at the times of the most recent and next MODIS overpasses, and *GOES(x,y,i,j)* is the cloud frequency value for hour *i* and month *j* at the 1-km pixel (*x,y*). The 1-km GOES values in Eq. (6) are set equal to the cloud frequency of the 4-km GOES pixel in which it lies. This fusion process is illustrated in Figure 5. The 1-km *CF* maps were resampled to 250-m using the bilinear spatial interpolation.

Cloud-solar function. Ground-based global solar radiation measurements obtained from the HaleNet climate network were used to develop an empirical function to relate the reduction of solar radiation by clouds to the satellite cloud frequency (CF):

$$C_{solar} = f(CF) \tag{7}$$

Subsequently, solar radiation is estimated as:

$$K_{global} = C_{solar} \cdot K_{clear-sky} \tag{8}$$

where K_{global} is global solar radiation (W m^{-2}), $K_{\text{clear-sky}}$ is clear-sky solar radiation (W m^{-2}), and C_{solar} is the ratio of K_{global} to $K_{clear\text{-sky}}$, estimated as a function of satellite-derived CF.

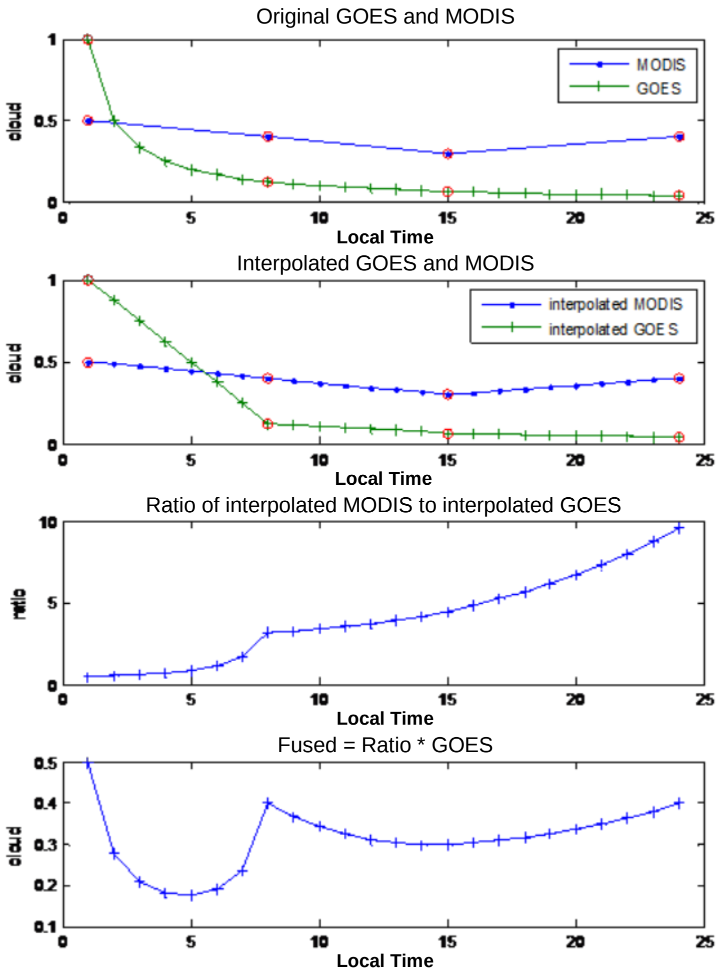

Figure 5. An example of the method for fusing 1-km, 4-times daily MODIS cloud frequency values with 1-km, hourly GOES values.

Direct and Diffuse Radiation

Global solar radiation is composed of direct (parallel-beam) radiation and diffuse radiation, solar radiation that has been scattered (reflected) by atmospheric gas molecules, aerosols, clouds, and surrounding terrain. It is important to quantify the relative amounts of direct and diffuse radiation for many purposes, including estimation of light penetration into plant canopies. It is also necessary to separate direct and diffuse radiation components when estimating terrain shading effects on solar radiation distribution (following section). Using diffuse radiation data from four sites (see Appendix Table A3), we developed an empirical diffuse radiation model as a function of K_{global} and CF. Direct radiation (K_{direct}), can be calculated as:

$$K_{direct} = K_{global} - K_{diffuse} \tag{9}$$

Terrain Shading

In mountainous areas, solar radiation is affected by elevation of the land surface and terrain shading. Terrain shading was estimated from sun angle in relation to relative elevation of terrain surrounding each pixel. The elevation angle of the local horizon for each pixel was determined for the appropriate azimuth direction for each day of the year and each hour of the day. A pixel was designated as shaded whenever the sun's elevation angle was less than the local horizon elevation angle. For shaded pixels, K_{direct} was set to zero, K_{diffuse} was assumed to be unaffected, and K_{global} was set equal to K_{diffuse}.

Reflected Shortwave Radiation

A portion of shortwave radiation (solar radiation) incident on the surface is reflected upward, the remaining portion is absorbed. The proportion of incoming radiation that is reflected depends on surface characteristics, sun angle, and the relative amount of diffuse radiation. However, a reasonably accurate estimate of reflected radiation can be obtained using a constant or seasonally-varying surface albedo (ratio of reflected to incident shortwave radiation) for each pixel:

$$K_{up\_i,j} = \alpha_j \cdot K_{down\_i,j} \tag{10}$$

where $K_{up\_i,j}$ is reflected shortwave radiation for hour i and month j, α_j is the albedo for month j, and $K_{down\_i,j}$ is incident solar radiation for hour i and month j.

We started with 1-km resolution mean monthly albedo derived from the MODIS product MOD43B3; (http://modis-atmos.gsfc.nasa.gov/ALBEDO/) and averaged for the period 2000-2004 by Chunxi Zhang (IPRC, University of Hawaiʻi at Mānoa, pers. comm.). For this study, it was necessary to estimate mean monthly albedo at 250-m resolution. To do so, the 30-m resolution HIGAP land cover data set (Gon, III et al. 1999; http://gis1.usgs.gov/csas/gap/viewer/land_cover/Map.aspx) was used as a covariate. HIGAP land cover classes are given in Appendix Table A6. (Note that this analysis was done early in the project, at a time when we were not aware of the more recent LANDFIRE land cover analysis. Also note that agricultural areas were not differentiated into specific crop types in the albedo analysis. However, the HIGAP map is very similar to the LANDFIRE map, and we believe use of the LANDFIRE map would have resulted in negligible changes in estimated albedo.) The albedo of each land cover type was assumed to be constant for a given month. Hence, the spatial variability of albedo in any month was considered to be the result of spatial land cover variation, with each land cover type having a characteristic albedo; i.e., the albedo of each 1-km MODIS pixel was assumed to be a linear combination of the albedo of each of the 30-m land cover pixels within each MODIS pixel. The albedo of each land cover type plus ocean surface was determined using a linear least-squares model:

$$\alpha\_MODIS_{h,j} = \sum_{c=1}^{38} \frac{x_{c,h} \cdot \alpha_{c,j}}{n} \tag{11}$$

where $\alpha\_MODIS_{h,j}$ is the albedo of MODIS pixel h in month j, $x_{c,h}$ is the number of 30-m HIGAP pixels of land cover type c in MODIS pixel h, $\alpha_{c,j}$ is the albedo of land cover c in month j, and n is the total number of HIGAP pixels in the MODIS pixel.

Downward Longwave Radiation

Radiation emitted by the atmosphere and clouds and absorbed at the earth's surface, "downward longwave radiation" (L_{down}), is a function of atmospheric temperature, humidity, and cloudiness. To estimate L_{down}, a model was developed of the form:

$$L_{down} = L_{down\_clear\_sky} \cdot C_{LW} \tag{12}$$

where $L_{down\_clear\text{-}sky}$ is downward longwave radiation under cloud-free conditions, C_{LW} is the ratio of L_{down} to $L_{down\_clear\text{-}sky}$, derived as a function of CF, satellite-derived cloud frequency. $L_{down\_clear\text{-}sky}$ was estimated according to the Stefan-Boltzmann equation as:

$$L_{down\_clear\_sky} = \epsilon_{atm} \sigma {T_a}^4 \tag{13}$$

where ε_{atm} is atmospheric emissivity, σ is the Stefan-Boltzmann constant (5.67 x 10^{-8} W m^{-2} K^{-4}), and T_a is air temperature (K). Following (Sugita and Brutsaert 1993), ϵ_{atm} was estimated as a function of precipitable water (w, cm):

$$\epsilon_{atm} = 0.762 + 0.055 \cdot ln(w) + 0.0031 \cdot ln(w^2) \tag{14}$$

Longman et al. (2012, 2013) showed that horizontal variations in mean w are negligible in the Hawaiʻi region. The spatial pattern of w obtained for the clear-sky radiation model, Eqs. (4) and (5), was used.

Cloud effects on L_{down} are critically important and must be accurately represented to provide adequate estimates of the spatial and temporal variability of L_{down} in Hawaiʻi. The statistical expression for estimating C_{LW} as a function of CF was derived using ground-measured L_{down} and satellite-derived CF at the sites identified in Appendix Table A3.

Upward Longwave Radiation

Emitted radiation by the surface or upward longwave radiation (L_{up}) is a function of the surface temperature and emissivity, as expressed by the Stefan-Boltzmann equation:

$$L_{up} = \epsilon_s \sigma {T_s}^4 \tag{15}$$

where ε_s is surface emissivity and T_s is surface temperature (K). In this analysis, ε_s was assumed to equal 1. T_s was estimated as a function of near-surface air temperature (T_a) plus a diurnally and seasonally varying offset:

$$T_s = T_a + \left(b_0 + b_1 \cdot e^{-\frac{(i-i_0)^2}{\sigma^2}} \right) \tag{16}$$

where i is the hour (1, 2, . . ., 24), i_0 is a parameter representing midday, and b_0, b_1, t_0, and σ are parameters derived through least squares optimization. Parameter values were determined for individual stations (see Appendix Table A3) using measured T_s and T_a data, and then averaged for three broad land cover groups: forest, grass and shrub, and barren land. Each of the land cover categories in the LANDFIRE classification was assigned to one of these three groups for the purposes of the surface temperature estimation.

Energy Storage Fluxes

Soil Heat Flux

The gain and loss of stored heat in the soil (soil heat flux; G) is an important component of the surface energy balance especially in areas with sparse or no vegetation. Spatial and temporal variations in G depend on net radiation, vegetation cover, and other variables. In this study, G was estimated using the following model:

$$G_{i,j} = R_{net\_j} \cdot (b_1 \cdot NDVI + b_0) \cdot \left(e^{\frac{(i-i_0)^2}{2\sigma^2}} - \frac{\sqrt{2\pi}\sigma}{24} \right) \tag{17}$$

where $G_{i,j}$ is soil heat flux (W m^{-2}) for hour i and month j, R_{net_j} is net radiation (W m^{-2}) for month j, $NDVI$ is the MODIS normalized difference vegetation index (Huete et al., 2002), and b_0, b_1, i_0, and σ are coefficients derived by statistical analysis of station data (Appendix Table A3). In this model, the factor ($b_0 \cdot NDVI + b_1$) provides an estimate of the diurnal amplitude of the G/R_{net} ratio, and the factor to the right of it defines the form of the diurnal cycle.

Biomass and Air Layer Energy Storage

As with G, gain and loss of stored energy in the biomass and air layer below the reference level (Q_b and Q_a, respectively) can be important components of the surface energy balance. Both variables are related to available energy (A) and aboveground biomass or vegetation height. To develop statistical models to estimate Q_b and Q_a, published studies of heat storage were sought for ecosystems similar to those in Hawaiʻi. The diurnal amplitudes of Q_b and Q_a were related to R_{net} and tree height. The shape of the diurnal cycle of these ratios was modeled after those of two field sites in Hawaiʻi with high time resolution heat storage measurements (the two HAVO towers).

Other Meteorological Variables

Air temperature

The spatial distribution of air temperature in Hawaiʻi is principally determined by local sea surface temperature, temperature of the upwind land surface, adiabatic cooling and warming of rising and sinking air, respectively, and exchanges of latent heat associated with formation and evaporation of cloud droplets. Air temperature generally decreases with elevation, as is true throughout the troposphere. However, persistent subsidence results in a temperature inversion, found about 80% of the time at an altitude of about 2200 m over Hawaiʻi (Cao et al., 2007). This so-called trade-wind inversion (TWI) is a shallow layer of air in which temperature increases with elevation. The TWI suppresses cloud development and separates moist marine air from arid upper air. Fluctuations in the height, thickness, and strength of the inversion blur its effect on the mean temperature lapse rate, and the inversion does not appear in the mean vertical temperature profile. However, the mean lapse rates differ for zones below and above the mean TWI height. Wet, fully vegetated land surfaces dispose of much of the net radiation they receive by evaporating and transpiring water, rather than heating the surface and air. Conversely, dry, more sparsely-vegetated land tends to heat up more under the same radiative input.

While numerous interactive factors influence air temperature, its spatial pattern is largely explained by elevation. The other influences tend to produce slightly higher temperatures on leeward than windward exposures at a given elevation. Hence, for this analysis, a statistical model of air temperature was developed with elevation and mean rainfall as the predictive variables.

In a previous project completed in 2005 (Pacific Rim Corrosion Research Program; Lloyd Hihara, PI; funded by the US Department of Defense), hourly air temperature was estimated for mean diurnal cycle of each month. First, monthly maximum, minimum, and mean temperature were estimated as functions of elevation, within an assumed two-layer atmosphere separated by the trade-wind inversion, and rainfall. The following piecewise (on elevation only) multiple regression model was used:

$$T = \frac{a_1(z_3 - z) + a_2(z - z_1)}{z_3 - z_1} + a_4 RF \qquad \text{for } z \le z_3$$

$$T = \frac{a_2(z_2 - z) + a_3(z - z_3)}{z_2 - z_3} + a_4 RF \qquad \text{for } z > z_3 \qquad (18)$$

where T is monthly maximum, minimum, or mean temperature (°C), z is elevation (m), RF is the corresponding mean monthly rainfall (mm), the coefficients a_1, a_2, a_3, and a_4 are derived simultaneously for the two segments of the model using least squares regression. The boundaries of the assumed two-layer atmosphere are set at z_1 = 0 m (lower boundary of lower layer), z_2 = 4200 m (upper boundary of upper layer), and z_3 = 2150 m (boundary separating lower and upper layers, set at the mean height of the trade-wind inversion base, based on Cao et al. (2007)). Model coefficients were derived using data from 131 stations distributed throughout the islands (Figure 1; Appendix Table A1). A digital elevation model (DEM) and digital rainfall maps (Giambelluca et al. 1986) were used as input to the temperature model to derive monthly minimum, maximum, and mean temperature grids at 250-m resolution (note that the more recent Hawaiʻi rainfall analysis, Giambelluca et al. 2013, was not available at the time of the air temperature analysis).

Following Feidas et al. (2002), the following equations were used to estimate the diurnal cycle of temperature:

$$T_t = T_{min} + \left[(T_{max} - T_{min}) \cdot sin\left(\pi \cdot \frac{(t - t\_sr) - b}{l + (2 \cdot (a - b))}\right)\right] \qquad \text{for } t_{Tmin} \leq t < t\_ss$$

$$T_t = T'_{min} + \left[(T_{t\_ss} - T'_{min}) \cdot exp\left(-c \cdot \frac{(t - t\_ss)}{24 - (l + b)}\right)\right] \qquad \text{for } t\_ss \leq t < 24 \qquad (19)$$

$$T_t = T'_{min} + \left[(T_{t\_ss} - T'_{min}) \cdot exp\left(-c \cdot \frac{24 + (t - t\_ss)}{24 - (l + b)}\right)\right] \qquad \text{for } 0 \leq t < t'_{Tmin}$$

where T_t is the diurnally varying temperature at time t; T_{min} and T_{max} are the monthly mean diurnal minimum and maximum temperature, respectively; T'_{min} is the minimum temperature of the next day (in this analysis set equal to T_{min}); T_{t_ss} is the temperature at sunset; t_{Tmin} is the time of day when the minimum temperature occurs; t'_{Tmin} is the time of minimum temperature of the next day (in this analysis set equal to t_{Tmin}); t_sr and t_ss are the times of sunrise and sunset respectively; l is the daylength ($l = t\_ss - t\_sr$); a is the difference between the time of maximum temperature and mid-day; b is the difference between times of minimum temperature and sunrise; and c is a decay parameter. All times are in hours local time. Times of sunrise and sunset were obtained for Kahului, Hawai‘i (20° 53’ N, 156° 28’ W), a central location within the islands, and used for the entire State (source: U.S. Naval Observatory web site; 2005 times used). Mean monthly temperature at sunset was estimated as a function of mean monthly temperature (T_{mean}) as:

$$T_{t\_ss} = d \cdot T_{mean} \qquad (20)$$

where the coefficient d was derived from station observations.

Relative Humidity

In a previous project completed in 2005 (Pacific Rim Corrosion Research Program; Lloyd Hihara, PI; funded by the US Department of Defense), hourly relative humidity was estimated for mean diurnal cycle of each month. First, monthly maximum and minimum relative humidity were each estimated as functions of elevation using a third order polynomial:

$$RH_x = a_0 + a_1 \cdot z + a_2 \cdot z^2 + a_3 \cdot z^3 \tag{21}$$

where RH_x is mean monthly minimum or maximum relative humidity (%), z is elevation (m), and a_0, a_1, a_2, and a_3 are coefficients derived from station data using least squares regression.

The diurnal cycle of was estimated for each month using the following model. First, mean hourly *RH* data at observation stations were transformed as:

$$RH_{norm\_i,j} = \frac{RH_{i,j} - RH_{\min\_j}}{RH_{\max\_j} - RH_{\min\_j}} \tag{22}$$

where $RH_{norm\_i,j}$ is the normalized mean hourly relative humidity for month j at a given station; $RH_{i,j}$ is the corresponding mean hourly relative humidity (%); and RH_{max_j} and RH_{min_j} are the mean monthly maximum and minimum relative humidity (%) for month j. A curve representing the diurnal cycle of RH_{norm} values was derived for each station/month using an expression of the form:

$$RH_{norm} = a_0 + \left(a_1 \cdot cos(t \cdot w)\right) + \left(b_1 \cdot sin(t \cdot w)\right) \tag{23}$$

where $t = (hr - 12.5)/7.071$, and hr = hour number (1, 2, 3, . . . , 24). The values of the diurnal relative humidity parameters, a_0, a_1, b_1, and w were derived as a function of elevation from station data using least squares regression.

Vapor Pressure Deficit

Vapor pressure deficit (VPD) can be estimated as:

$$VPD = e_{sat} - e \tag{24}$$

where e_{sat} = saturation vapor pressure (MPa) and e = ambient vapor pressure (MPa). Air temperature is used to estimate e_{sat} as (Lowe 1977):

$$e_{sat} = a_0 + T \cdot \left(a_1 + T \cdot \left(a_2 + T \cdot \left(a_3 + T \cdot \left(a_4 + T \cdot (a_5 + a_6 \cdot T)\right)\right)\right)\right) \tag{25}$$

where T = air temperature (°C); and the coefficients are: a_0 = 6.107799961; a_1 = 4.436518521E-1; a_2 = 1.428945805E-2; a_3 = 2.650648471E-4; a_4 = 3.031240396E-6; a_5 = 2.034080948E-8; and a_6 = 6.136820929E-11.

Wind Speed

High-resolution (200-m) resolution wind maps developed by AWS Truewind (2004) were used in this study. Using their 50-m height wind speed data set, mean wind speed was estimated for a reference level of 2 m above the vegetation height as:

$$U_{h+2} = U_{50m} \cdot \frac{ln\left(\frac{h+2-d}{z_{0m}}\right)}{ln\left(\frac{50-d}{z_{0m}}\right)} \tag{26}$$

where U_{h+2} is mean wind speed at the reference level of vegetation height (h) plus 2 m (m s^{-1}), U_{50m} is mean wind speed at 50 m above the ground (m s^{-1}), d is the mean of 12 monthly values of zero plane displacement (m), and z_{0m} is the mean of 12 monthly values of roughness length for momentum (m). The values of d and z_{0m} were estimated on the basis of vegetation height and leaf area index as (Shuttleworth 2012):

$$d_j = 1.2h \cdot ln\left[1 + \left(\frac{LAI_j}{5}\right)^{0.25}\right] \tag{27}$$

$$z_{0m\_j} = z_0' + 0.29h \cdot \left(\frac{LAI_j}{5}\right)^{0.5} \qquad \text{for LAI} \le 0.5$$
$$z_{0m\_j} = 0.24h \cdot \left(1 - \frac{d_j}{h}\right) \qquad \text{for LAI} > 0.5 \qquad (28)$$

where d_j is zero plane displacement for month j (m), h is vegetation height (m) set to the midpoint of the vegetation height ranges in the LANDFIRE EVH classification, except for the tallest category (25-50 m), for which h was set to 25 m, LAI_j is leaf area index for month j, derived from the MODIS *LAI* product, z_{0m_j} is the roughness length for month j (m), and z'_0 is roughness length of the soil surface. For this study, z'_0 was set to 0.005 m.

Ground observations at HaleNet sites indicated that the annual cycle of wind speed has a small amplitude, but the diurnal cycle is significant. Therefore, a model was developed to estimate the mean hourly wind speeds for each location, based on elevation. Station data (Appendix Table A3) were used to develop the diurnal wind speed model. The 24 mean hourly wind speed values at each station were normalized by the overall station mean. For each hour, normalized wind speed was related to elevation using linear and non-linear models (depending on the hour):

$$Norm(U_i) = \frac{a_i}{1 + e^{\frac{-(z - z_{0\_i})}{b_i}}} \qquad \text{For } i = \text{1-7 and 21-24}$$
$$Norm(U_i) = c_i + d_i \cdot z \qquad \text{For } i = \text{8-9 and 19-20} \qquad (29)$$
$$Norm(U_i) = g_i + h_i \cdot e^{-k_i \cdot z} \qquad \text{For } i = \text{10-18}$$

where $Norm(U_i)$ is the normalized wind for hour i, z is elevation (m), and the parameters a_i, b_i, z_{0_i}, c_i, d_i, g_i, h_i, and k_i were obtained for each hour by least-squares regression. Normalized hourly speed was estimated at 250-m resolution using a digital elevation map (DEM), and then applied to the mean wind speed map (resampled to 250-m) to obtain 24 hourly maps of wind speed. Hourly wind speed was estimated as:

$$U_i = Norm(U_i) \cdot U_{h+2} \tag{30}$$

where U_i is the wind speed for hour i (m s^{-1}).

Potential Evapotranspiration

Potential evapotranspiration (*PET*) is defined as the evapotranspiration rate under the existing atmospheric conditions, and with non-limiting water availability. This definition is interpreted in various ways for different purposes. For this project, *PET* was calculated using three different methods.

Priestley-Taylor Potential Evapotranspiration

Priestley and Taylor (1972) showed that the evapotranspiration of an extensive surface with abundant water availability can be estimated as:

$$\lambda E_{Priestley-Taylor} = \alpha \frac{sA}{s+\gamma} \tag{31}$$

where λE is the latent heat flux equivalent of ET (W m^{-2}) under potential (non-limiting moisture) conditions, α is the Priestley-Taylor coefficient (usually set to 1.26), s is slope of saturation vapor pressure versus temperature curve (mb K^{-1}), A is available energy (net radiation minus heat storage in the soil, biomass, and air layer below the reference height (W m^{-2})), and γ is the psychrometric constant (mb K^{-1}). λE can be divided by the latent heat of vaporization (λ, W m^{-2} per mm $hour^{-1}$), to obtain Priestley-Taylor *PET* in water units (mm $hour^{-1}$).

Penman-Monteith Potential Evapotranspiration

Monteith (1965) modified the Penman (1948) equation to develop an actual evapotranspiration model. By setting the surface resistance term equal to zero, the Penman-Monteith equation can be used to estimate *PET* as:

$$\lambda E_{Penman-Monteith\_potential} = \frac{sA+\rho_a C_p(e_{sat}-e)/r_a}{s+\gamma} \quad (32)$$

where λE is the latent heat flux equivalent of *PE* (W m^{-2}), s is slope of saturation vapor pressure versus temperature curve (mb K^{-1}), A is available energy (net radiation minus heat storage in the soil, biomass, and air layer below the reference height (W m^{-2}), ρ_a is air density (kg m^{-3}), C_p is specific heat of air at constant pressure (set to 1005 J K^{-1} kg^{-1}), r_a is aerodynamic resistance (s m^{-1}), e_{sat} is saturation vapor pressure (mb), e is ambient vapor pressure (mb), and γ is the psychrometric constant (mb K^{-1}). As in Eq. (1), the value obtained using Eq. (32) can be multiplied by $^{n}/_{(\lambda \cdot \rho_w)}$, where n is the number of seconds in the relevant time period, λ is the latent heat of vaporization of water (J kg^{-1}), and ρ_w is the density of water (kg m^{-3}) at the relevant temperature. to obtain *PE* in water units (mm). The latent heat of vaporization was approximated as a function of air temperature:

$$\lambda_{i,j} = 2500800 - 2360T_{i,j} + 1.6T_{i,j}^2 - 0.06T_{i,j}^3 \quad (33)$$

where $\lambda_{i,j}$ is the latent heat of vaporization for hour *i* and month *j*, and $T_{i,j}$ is air temperature of hour *i* and month *j*. Air density (ρ_a) is estimated as the sum of dry air density (ρ_d) and vapor pressure density (ρ_v), where:

$$\rho_d = \frac{P-e}{R_d \cdot T} \quad (34)$$

where P is air pressure (Pa), e is vapor pressure (Pa), R_d is the gas constant for dry air (287.058 J kg^{-1} K^{-1}), and T is air temperature (K); and where:

$$\rho_v = \frac{e}{R_w \cdot T} \tag{35}$$

where R_w is the gas constant for water vapor (287.058 J kg^{-1} K^{-1}).

Aerodynamic resistance, r_a, was estimated using the method described by Bonan (2008):

$$r_{a\_i,j} = \frac{1}{k^2 u_i}\left[ln\left(\frac{z-d_j}{z_{0m\_j}}\right) - \psi_m(\zeta_{i,j})\right]\left[ln\left(\frac{z-d_j}{z_{0h\_j}}\right) - \psi_h(\zeta_{i,j})\right] \tag{36}$$

where k = 0.4 is the von Kármán constant, u_i is wind speed for hour i, z is the reference height for wind velocity (m), d_j and z_{0m_j} are defined in Eqs. (27-28), and z_{0h_j}, roughness length for heat for each month j, was estimated as:

$$z_{0h\_j} = 0.1 z_{0m\_j} \tag{37}$$

$\psi_m(\zeta)$ and $\psi_h(\zeta)$ are functions that represent the effects of atmospheric stability on buoyancy for turbulent flux of momentum and heat, and are estimated as:

$$\psi_m(\zeta_{i,j}) = \begin{cases} 2ln\left(\frac{1+x_{i,j}}{2}\right) + ln\left(\frac{1+x_{i,j}^2}{2}\right) - 2\tan^{-1}(x_{i,j}) + \frac{\pi}{2} & \zeta_{i,j} < 0 \\ -5\zeta_{i,j} & \zeta_{i,j} \geq 0 \end{cases} \tag{38}$$

$$\psi_h(\zeta_{i,j}) = \begin{cases} 2ln\left(\frac{1+x_{i,j}^2}{2}\right) & \zeta_{i,j} < 0 \\ -5\zeta_{i,j} & \zeta_{i,j} \geq 0 \end{cases} \tag{39}$$

where $x_{i,j} = (1 - 16\zeta_{i,j})^{0.25}$ and where:

$$\zeta_{i,j} = \frac{z-d_j}{L_{i,j}} \tag{40}$$

where the Obukov length stability parameter ($L_{i,j}$) for hour i and month j is estimated as:

$$L_{i,j} = \frac{\theta_{i,j}\left(u_{*\_i,j}\right)^3}{gkH_{i,j}} \tag{41}$$

where $\theta_{i,j}$ is potential temperature (K) for hour i and month j, $u_{*\_i,j}$ is friction velocity (m s^{-1}) for hour i and month j, g is gravitational acceleration (m s^{-2}), and $H_{i,j}$ is sensible heat flux (W m^{-2}) for hour i and month j. Potential temperature was estimated as:

$$\theta_{i,j} = \left(273.15 + T_{i,j}\right)\left(\frac{10^5}{P}\right)^{0.285} \tag{42}$$

were P is air pressure (Pa) estimated as shown in Eq. (14). Friction velocity was estimated as:

$$u_{*\_i} = \frac{ku_i}{ln\left(\frac{z-d}{z_{0m}}\right)} \tag{43}$$

where u_i is wind velocity at reference height for hour i. Sensible heat flux (H) was initially estimated as

$$H_{i,j} = \rho_{i,j}C_p\frac{T_{s\_i,j}-T_{a\_i,j}}{r_{a\_i,j}} \tag{44}$$

where $\rho_{i,j}$ is air density (kg m^{-3}), C_p is specific heat of air at constant pressure (set to 1005 J K^{-1} kg^{-1}), $T_{s\_i,j}$ and $T_{a\_i,j}$ are surface and air temperature, respectively, and where the subscripts i and j indicate hour and month, respectively. Aerodynamic resistance, $r_{a\_i,j}$, was initially estimated using Eq. (36) with stability terms set to zero (neutral assumption). After the first iteration, stability terms could be estimated, allowing $H_{i,j}$ to be recalculated using stability-adjusted $r_{a\_i,j}$. This procedure was repeated until the estimate of $r_{a\_i,j}$ converged (typically < 10 iterations).

Grass Reference Surface Potential Evapotranspiration

The Food and Agriculture Organization (FAO) developed a standardized method for reference surface evapotranspiration (ET_0). The FAO method utilizes the Penman-Monteith approach, similar to that described above, but with several simplifications (Allen et al. 1998). In this study, we approximated the FAO method by using Eq. (32) with aerodynamic resistance (r_a) calculated without stability correction, vegetation height (h) set to 0.12 m, roughness length for momentum (z_{0_m}) set to $0.123h$, zero plane displacement (d) set to $2\ h\ /3$, and reference height (z) set to 2 m. All other inputs to Eq. (32) were as described for the Penman-Monteith PET estimates (above).

Evapotranspiration

The more general form of the Penman-Monteith equation, Eq. (1), can be used to estimate evapotranspiration (ET), sometimes referred to as actual evapotranspiration.

To calculate ET, the process was divided into three components: (1) wet-canopy evaporation (λE_{WC}); (2) transpiration (λE_{Transp}); and (3) soil evaporation (λE_{Soil}), each using a modified form of the Penman-Monteith equation. In each case, the flux calculated in latent energy flux units (W m^{-2}) can be multiplied by $^{n}/_{(\lambda\cdot\rho_w)}$, where n is the number of seconds in the relevant time period, λ is the latent heat of vaporization of water (J kg^{-1}), and ρ_w is the density of water (kg m^{-3}) at the relevant temperature, to obtain ET in water units (mm). Total latent heat flux or evapotranspiration is then calculated as the sum of the three components:

$$\lambda E = \lambda E_{WC} + \lambda E_{Transp} + \lambda E_{Soil}$$

or (45)

$$ET = E_{WC} + Transp + E_{Soil}$$

Wet-canopy Evaporation

Evaporation of water from rain-, fog-, or dew-wetted vegetation is estimated as:

$$\lambda E_{WC} = f_c \cdot f_w \cdot \frac{sA + \rho_a C_p (e_{sat} - e)/r_a}{s + \gamma\left(1 + \frac{r_{s\_water}}{r_a}\right)} \tag{46}$$

where f_c = vegetation cover fraction, f_w = canopy wetness fraction, and r_{s_water} is the surface resistance for liquid water (10 s m^{-1}, La Mer and Healy 1965, cited by van de Griend and Owe 1994). Monthly maps of f_c were derived from the Moderate Resolution Imaging Spectrometer (MODIS) Enhanced Vegetation Index (EVI) as:

$$f_c = \frac{EVI - EVI_{min}}{EVI_{max} - EVI_{min}} \tag{47}$$

where EVI_{min} and EVI_{max} were set as constants equal to 0.05 and 0.95, respectively, following Mu et al. (2007).

Maps of f_w were developed using a statistical relationship between average canopy wetness and relative humidity, derived from leaf wetness sensor data (data provided by L. Hihara, pers. comm., 2013). At each of eight sites in Hawai‘i (Appendix Table A3), a canopy wetness index time series was derived. At each time step, the leaf wetness sensor (Model 237, Campbell Scientific, Inc., Logan, UT, USA) voltage was divided by period-of-record maximum voltage to produce the index. Comparison of this index with f_w, defined as the relative frequency of periods with leaf wetness sensor signal greater than the median signal, was done for the Thurston station (Figure 6). The result indicates that the index replicates f_w

reasonably well. The coefficients for a 3-parameter sigmoid function describing the relationship between f_w and RH were set via least squares regression using 30-min RH and leaf wetness sensor data for all eight stations combined.

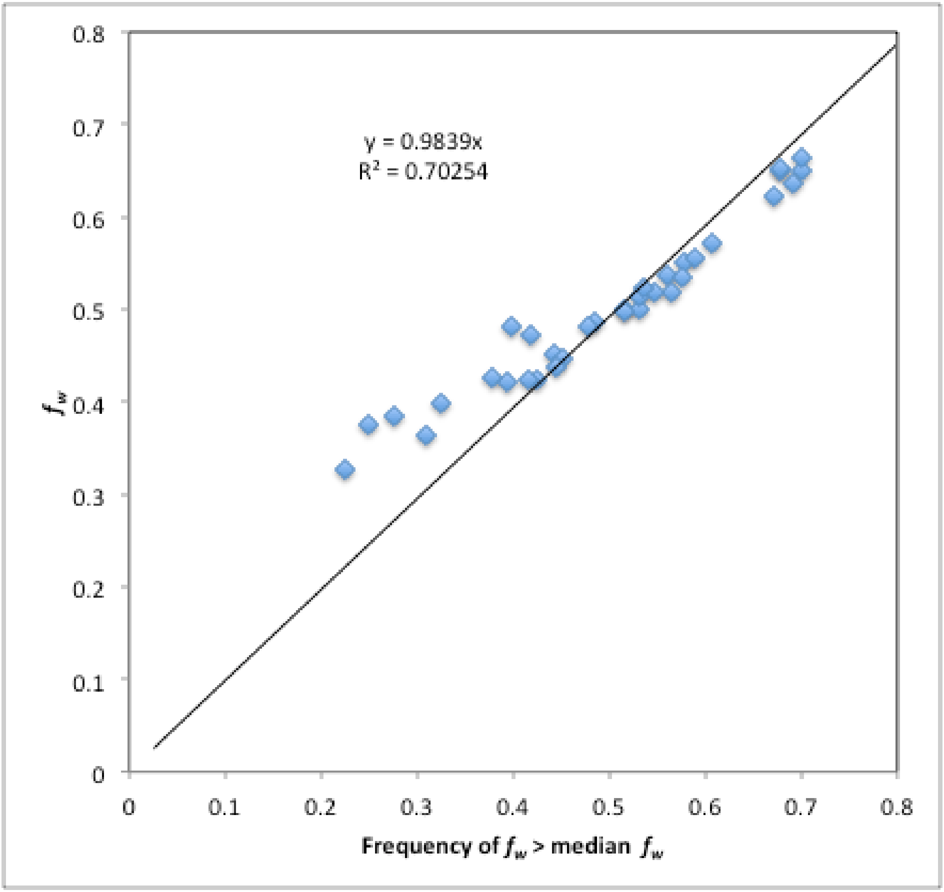

Figure 6. Scatterplot of mean monthly canopy wetness fraction (f_w), defined as the leaf wetness sensor voltage divided by the period-of-record maximum sensor voltage, versus the monthly frequency of 30-min values of f_w greater than the median, for the Thurston tower station (HVT, see Appendix Table A2).

Transpiration

The Penman-Monteith equation for transpiration is expressed as:

$$\lambda E_{Transp} = f_c \cdot (1 - f_w) \cdot \frac{sA + \rho_a C_p (e_{sat} - e)/r_a}{s + \gamma\left(1 + \frac{r_c}{r_a}\right)} \tag{48}$$

where r_c is the inverse of stomatal conductance:

$$r_c = \frac{1}{g_c} \tag{49}$$

where g_c is estimated using a Jarvis-Stewart approach (Jarvis 1976; Stewart 1988):

$$g_c = g_{c\_max} \cdot f_S \cdot f_{VPD} \cdot f_T \cdot f_\theta \tag{50}$$

where g_{c_max} is the maximum canopy conductance of a given land cover type and f_S, f_{VPD}, f_T, and f_θ are constraint factors for solar radiation, vapor pressure deficit, temperature, and soil moisture, respectively. The canopy-level parameter g_{c_max} is estimated based on the land-cover-specific leaf-level maximum stomatal conductance, g_{s_max}, as (adapted from Kelliher et al. 1995):

$$g_{c\_max} = \frac{g_{s\_max}}{0.6} \ln\left(\frac{Q+60}{Q \cdot e^{-0.6LAI}+100}\right) \tag{51}$$

where Q is photosynthetically active radiation (PAR, μmol m^{-2} s^{-1}), approximated as $2K_d$, where K_d is solar radiation (W m^{-2}), and LAI is leaf area index derived from the relevant mean monthly MODIS-based LAI map. For low values of K_d and LAI, Eq. (51) can result in a negative value for g_{c_max}. In such cases, g_{c_max} was set to 0.

The parameter g_{s_max} is important for simulating the effects of species-specific physiological characteristics of vegetation on transpiration. Although species-level specification is not possible for the statewide domain, it is possible to identify one or more key species to represent each land-cover category. In some ecosystems in Hawai'i, a single species is dominant, and can accurately represent physiological response. Based on leaf-level measurements reported in the literature and those provided through personal communication by local scientists, g_{s_max} values were obtained for as many representative species as possible. In the case of species whose g_{s_max} could not be found, a similar species was substituted. Appendix Table A8 lists representative species and g_{s_max} values used in this study.

The constraint factors for solar radiation (f_S), vapor pressure deficit (f_{VPD}), temperature (f_T), and soil moisture (f_θ) each take values ranging between 0 and 1. The solar radiation factor is estimated as (Stewart 1988):

$$f_S = \frac{1.1 \cdot K_{global}}{K_{global}+100} \qquad \text{for } K_{global} \le 1000 \text{ W m}^{-2}$$
$$f_S = 1.0 \qquad \text{for } K_{global} > 1000 \text{ W m}^{-2} \qquad (52)$$

where K_{global} is solar radiation (W m^{-2}). For the invasive tree strawberry guava (*Psidium cattleianum*), whose light response was found by Miyazawa (pers. comm. 2013) to be muted, the following model is used for the light constraint on g_c:

$$f_{S\_guava} = 0.4 + \frac{0.69 \cdot K_{global}}{K_{global}+60} \qquad \text{for } K_{global} \le 400 \text{ W m}^{-2}$$
$$f_{S\_guava} = 1.0 \qquad \text{for } K_{global} > 400 \text{ W m}^{-2} \qquad (53)$$

The *VPD* factor is estimated as (modified from Mu et al. 2011):

$$f_{VPD} = 1.0 \qquad \text{for } VPD \le VPD_{open}$$
$$f_{VPD} = 0.9\,\frac{VPD_{close}-VPD}{VPD_{close}-VPD_{open}} + 0.1 \qquad \text{for } VPD_{open} < VPD < VPD_{close} \qquad (54)$$
$$f_{VPD} = 0.1 \qquad \text{for } VPD \ge VPD_{close}$$

where VPD_{open} is the *VPD* value at which there is no water stress on transpiration, and VPD_{close} is the *VPD* value at which stomata close almost completely. The values of VPD_{open} and VPD_{close} are land cover specific. Values were assigned based on the biome property look-up table provided by Mu et al. (2011, Table 1).

The temperature factor is estimated as (modified from Mu et al. 2007):

$$f_T = 1.0 \qquad \text{for } T_{min} \ge T_{min\_close}$$
$$f_T = 0.9\,\frac{T_{min}-T_{\min\_close}}{T_{\min\_open}-T_{\min\_close}} + 0.1 \qquad \text{for } T_{min\_close} < T_{min} < T_{min\_open} \qquad (55)$$
$$f_T = 0.1 \qquad \text{for } T_{min} \le T_{min\_close}$$

where T_{open} is the air temperature at which there is no water stress on transpiration, and T_{close} is the air temperature at which stomata close almost completely. Values were assigned based on the biome property look-up table provided by Mu et al. (2011, Table 1).

Stomatal conductance is responsive to plant water status to varying degrees. Regarding its effects on stomatal conductance, leaf water potential may be the best variable to represent plant water status (Jarvis 1976). However, in most situations, leaf water potential is not known and available soil moisture content is used instead.

$$\theta = \frac{VSM - VSM_{WP}}{VSM_{FC} - VSM_{WP}} \tag{56}$$

where θ is available soil moisture, VSM is volumetric soil moisture in the upper 30 cm soil layer, VSM_{WP} is the volumetric soil moisture at the wilting point, and VSM_{FC} is the volumetric soil moisture at field capacity. Numerous empirical functions have been proposed to describe the dependency of transpiration on soil moisture (Dyer and Baier 1979). In general, for soil moisture content near field capacity, transpiration is assumed to be unaffected. As the soil dries, a critical soil moisture content is reached below which transpiration declines with further decreases in soil moisture. The decline continues until transpiration reaches zero at a soil moisture content somewhat greater than zero available water. In this study, a simple piecewise linear function was used, with the critical available soil moisture content set at 0.8 and zero transpiration at an available soil moisture content of 0.1:

$$\begin{aligned} f_\theta &= 0.0 && \text{for } \theta \leq 0.1 \\ f_\theta &= \frac{1}{0.7}\theta - \frac{0.1}{0.7} && \text{for } 0.1 < \theta \leq 0.8 \\ f_\theta &= 1.0 && \text{for } \theta \geq 0.8 \end{aligned} \tag{57}$$

In fact, the response of stomatal conductance to soil moisture varies according to species, root depth, soil type, and other factors (Giambelluca 1983). However, the necessary information on plant ecophysiology, root depth, and soil characteristics are not available with sufficient spatial detail over the whole state. Therefore, the parameters defining the soil moisture constraint curve are held constant at middle-of-the-road values.

For this study, θ is estimated as an empirical function of mean monthly rainfall in the current and previous months. HaleNet data were used to define the soil moisture-rainfall relationship for non-urban, non-irrigated areas. For urban and irrigated agriculture areas, data from Giambelluca (1983) were used.

Note that when g_{c_max} or any of the constraint factors (f_S, f_{VPD}, f_T, or f_θ) are set to zero, g_c becomes zero and r_c goes to infinity. In that case, transpiration was set to zero.

Soil Evaporation

Evaporation of water from soil is estimated as:

$$\lambda E_{Soil} = (1 - f_c) \cdot f_\theta \cdot \frac{sA + \rho_a C_p (e_{sat} - e)/(r_a + r_u)}{s + \gamma} \qquad (58)$$

Soil evaporation is observed to behave as a three-stage response to declining soil moisture content and is modeled that way in this study. The soil moisture function for soil evaporation is similar in form to that used for stomatal conductance. For soil evaporation, the function used here begins reducing the evaporation rate at a higher critical soil moisture content (0.9) and reaches zero at a higher soil moisture content (0.15) than was used for estimating the stomatal conductance constraint factor:

$$f_\theta = 0.0 \qquad \text{for } \theta \leq 0.15$$
$$f_\theta = \frac{1}{0.75}\theta - \frac{0.15}{0.75} \qquad \text{for } 0.15 < \theta \leq 0.9 \tag{59}$$
$$f_\theta = 1.0 \qquad \text{for } \theta \geq 0.9$$

r_u is the additional aerodynamic resistance between the canopy height and the soil surface in sparse vegetation. Following Norman et al. (1995), r_u (s m^{-1}) was defined as:

$$r_u = \frac{1}{0.004 + 0.012 u_s} \tag{60}$$

where u_s is wind speed near the soil surface (m s^{-1}), estimated as:

$$u_s = u_c \cdot e^{-a \cdot \frac{1-0.05}{h}} \tag{61}$$

where u_c is the wind speed above the canopy(m s^{-1}), h is the vegetation height (m), and a is defined as:

$$a = 0.28 \cdot LAI \cdot h^{\frac{1}{3}} \cdot s^{-\frac{1}{3}} \tag{62}$$

where s is the mean leaf size, defined as "four times the leaf area divided by the perimeter" (Norman et al. 1995). For this study s was held constant at 0.1. Note that we imposed a minimum value of 20 s m^{-1} for r_u to constrain soil evaporation estimates to within a reasonable range.

RESULTS

Land Surface Characteristics

Leaf Area Index

Mean monthly leaf area index (*LAI*) was derived from the MODIS LAI product. Estimated mean annual leaf area index for the Hawaiian Islands is shown in Figure 7.

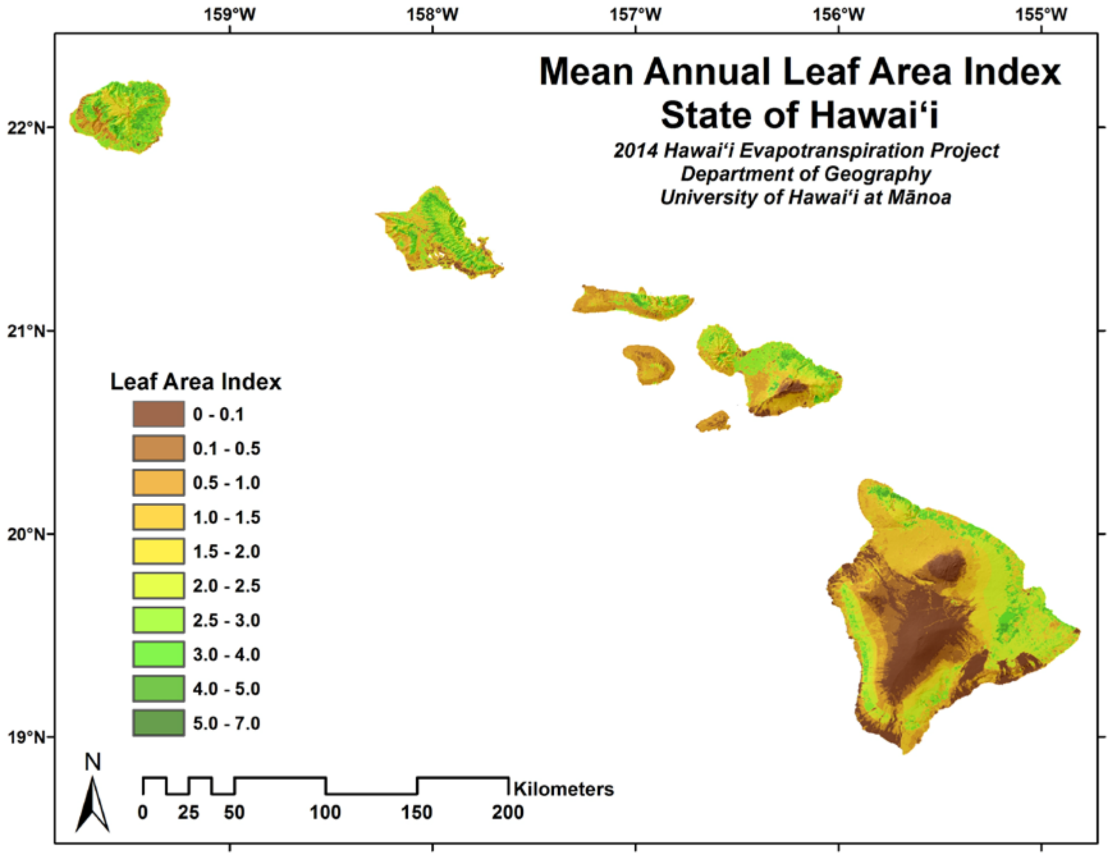

Figure 7. Map of mean annual leaf area index of Hawai'i.

Vegetation Cover Fraction

Vegetation cover fraction (f_c) was derived for each month based on MODIS *EVI* (Eq. 47). Estimated mean annual vegetation cover fraction for the Hawaiian Islands is shown in Figure 8.

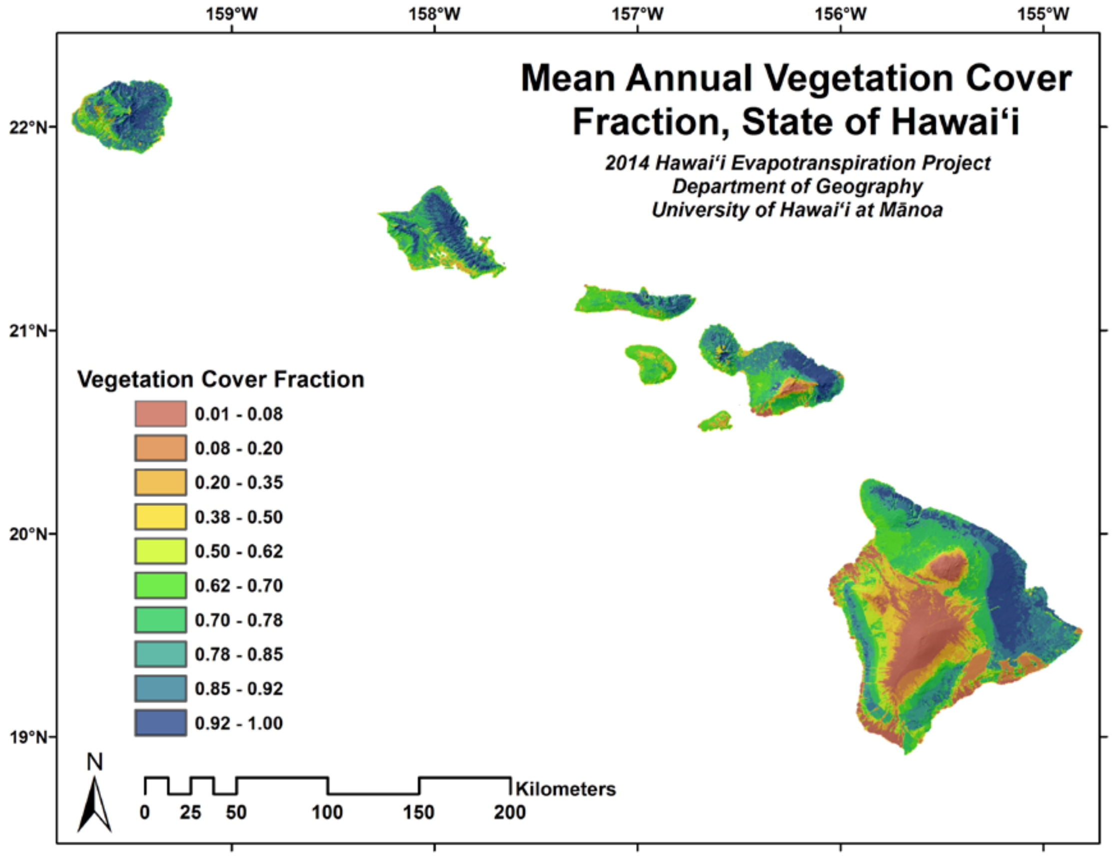

Figure 8. Map of mean annual vegetation cover fraction of Hawaiʻi.

Vegetation Height

Vegetation height (h) was estimated based on the LANDFIRE EVH. Estimated vegetation height for the Hawaiian Islands is shown in Figure 9.

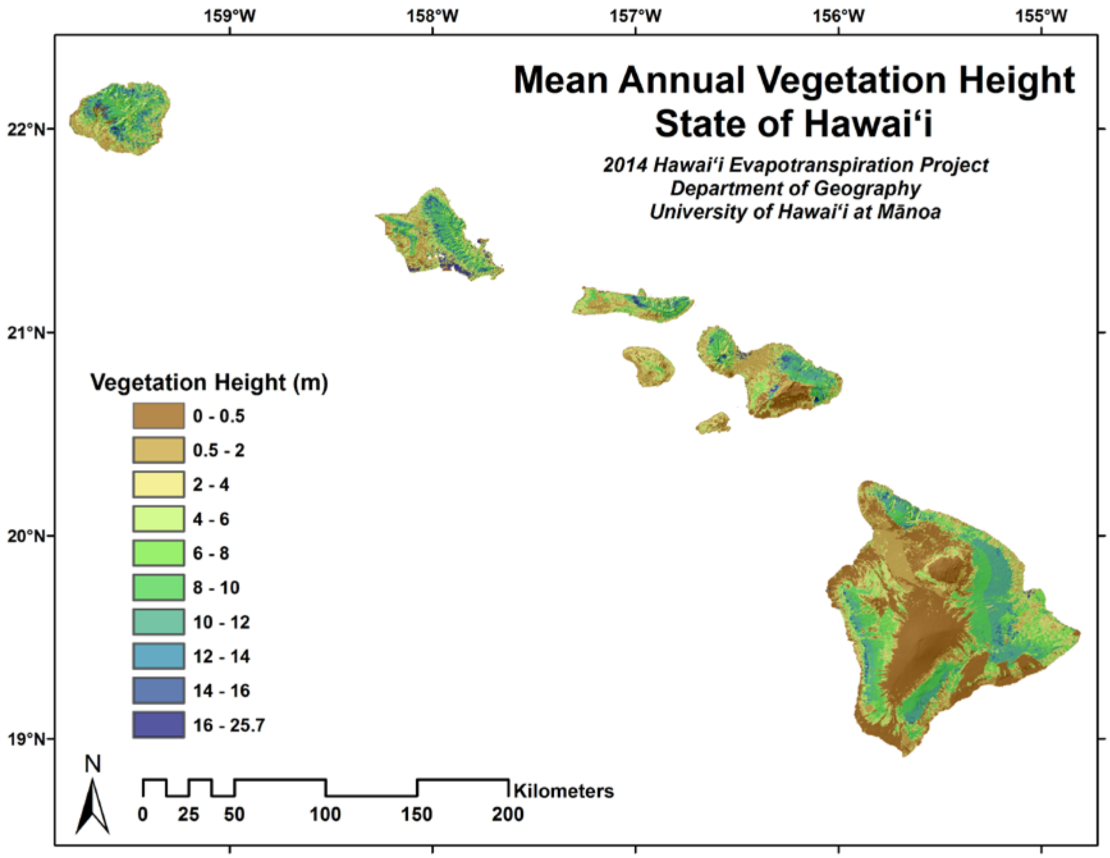

Figure 9. Map of vegetation height of Hawaiʻi.

Available Soil Moisture

Mean monthly rainfall and soil moisture data from seven HaleNet stations (HN119, HN151, HN152, HN153, HN161, HN162, and HN164) were used to develop a statistical model to estimate available soil moisture (θ) (Figure 10):

$$\theta = 0.182 \cdot ln(RF_i + RF_{i-1}) + 0.2632 \tag{63}$$

where RF_i and RF_{i-1} are the mean monthly rainfall of the current and previous months, respectively.

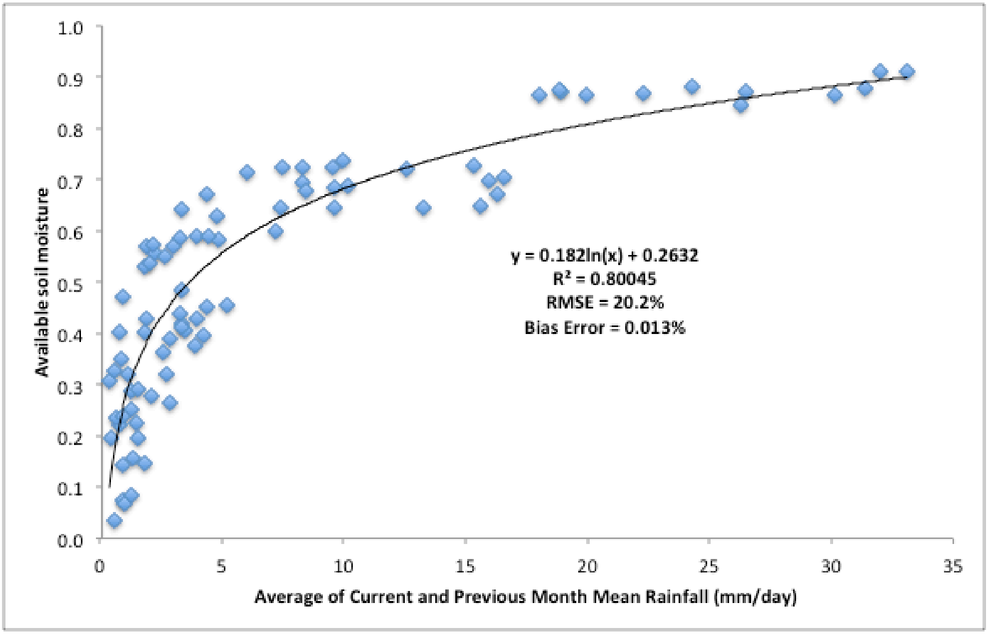

Figure 10. Relationship between mean monthly soil moisture and the average of mean monthly rainfall of the current and previous month for seven HaleNet stations.

A statistical model to estimate soil moisture in irrigated agricultural areas was derived using estimated mean monthly soil moisture and rainfall in drip irrigated sugarcane in southern Oʻahu (Giambelluca 1983). Figure 11 shows the relationship between soil moisture and the average of rainfall in the current month and previous month for irrigated agricultural areas.

A point representing average urban residential areas in Hawaiʻi was selected in the Makiki-Lower Mānoa area of Oʻahu. Mean monthly rainfall was obtained for this location from the Rainfall Atlas of Hawaiʻi (Giambelluca et al. 2013). Mean monthly urban irrigation estimates from Giambelluca (1983, Table 17, p. 75) were added to the monthly rainfall to get monthly total water input. Monthly soil moisture was then estimated using the two-month average of total water input in place of two-month average rainfall in the soil model for non-irrigated areas (Eq. 63). The soil moisture estimates were plotted versus the two-month average rainfall. The result showed that available soil moisture for urban areas follows a pattern similar to non-irrigated areas for two-month average rainfall greater than 4 mm per day, but levels off at a minimum of 0.52 for lower rainfall values (Figure 12). Estimated soil moisture for urban areas was adjusted for the proportion of pervious land cover in each pixel (ET is assumed to be zero for paved areas). The pervious fraction was set at 0.90, 0.65, 0.35, and 0.10 for Developed-Open Space, -Low Intensity, -Medium Intensity, and –High Intensity classes, respectively. To get pixel-scale soil moisture, the pervious area soil moisture estimate (Figure 12) was multiplied by the pervious fraction.

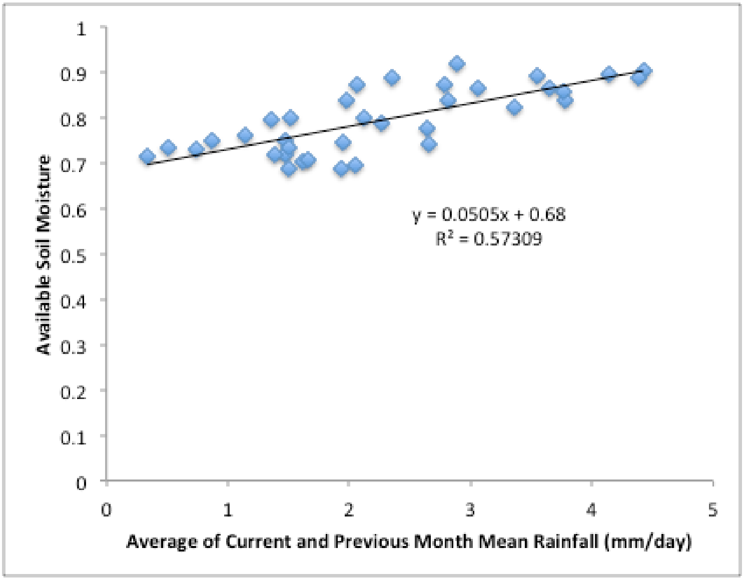

Figure 11. Relationship between mean monthly soil moisture and the average of rainfall in the current month and previous month for three irrigated sugarcane water balance zones in southern Oʻahu (data from Giambelluca 1983).

Estimated mean annual soil moisture of the Hawaiian Islands is shown in Figure 13. For validation purposes, modeled soil moisture estimates are compared with soil moisture measured at stations not used in model development (Figure 14 and Table 1).

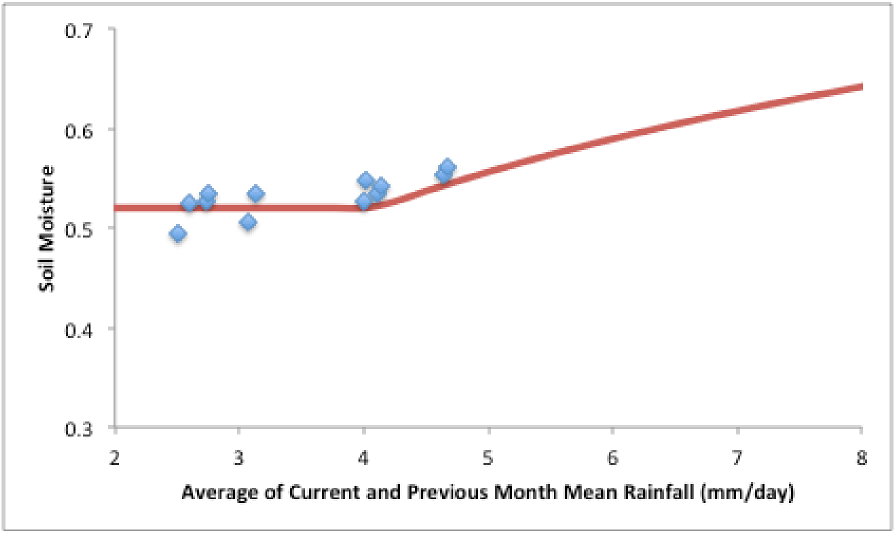

Figure 12. Relationship between mean monthly soil moisture and the average of rainfall in the current month and previous month for a representative irrigated urban location in southern Oʻahu (data from Giambelluca 1983).

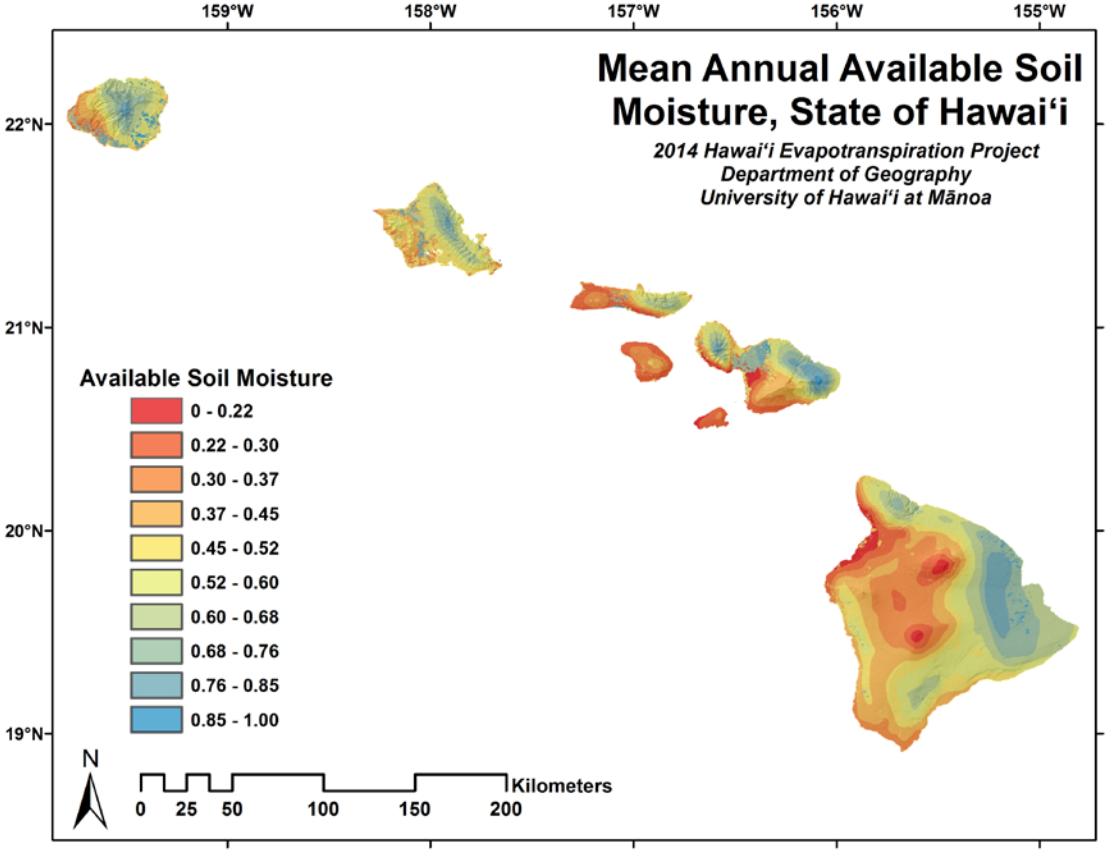

Figure 13. Map of mean annual available soil moisture of Hawaiʻi.

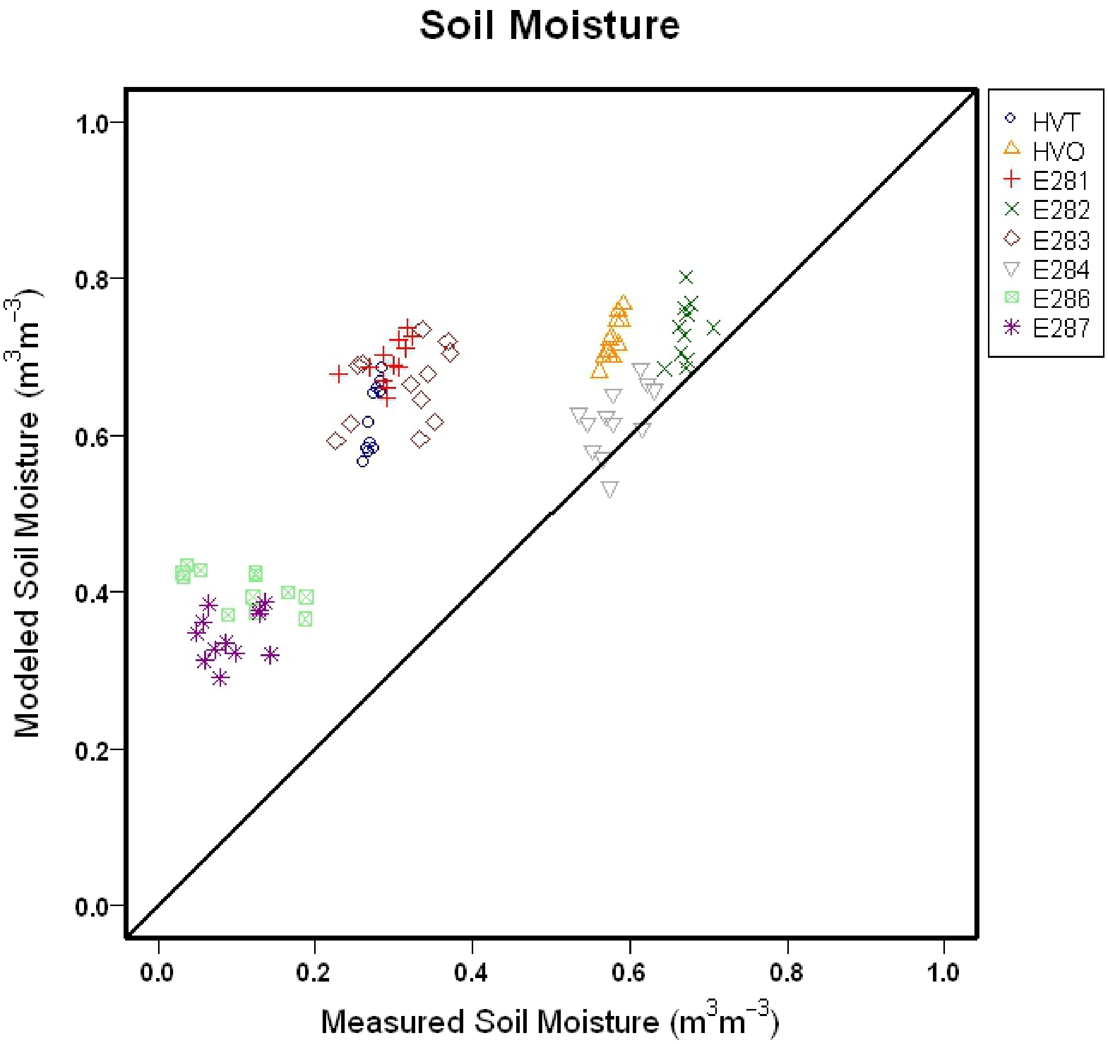

Figure 14. Scatterplot of estimated (mapped) versus observed mean monthly soil moisture at validation stations.

Table 1. Statistical results of estimated versus measured soil moisture for all available observing stations not used in model development.

STA. ID	N	b	a	R2	MBE	MBE%	RMSE	RMSE%	MOD.	MEAS.	MON.	%MON.
All STA.	95	0.52	0.4	0.58	0.24	66	0.27	76	0.60	0.36	314	NA
HVT	12	5.08	-0.8	0.85	0.35	129	0.35	129	0.63	0.27	58	44
HVO	12	2.46	-0.7	0.71	0.14	25	0.14	25	0.72	0.58	51	39
E281	12	0.59	0.5	0.30	0.40	136	0.40	136	0.69	0.29	31	NA
E282	11	0.82	0.2	0.10	0.06	9	0.07	10	0.73	0.67	33	NA
E283	12	0.37	0.5	0.15	0.35	112	0.35	114	0.66	0.31	44	NA
E284	12	0.71	0.2	0.27	0.04	7	0.05	9	0.62	0.58	39	NA
E286	12	-0.26	0.4	0.39	0.30	279	0.31	287	0.40	0.11	36	NA
E287	12	0.24	0.3	0.07	0.25	275	0.26	278	0.34	0.09	22	NA

N = number points in sample; b and a = slope and y-intercept, respectively, of least squares regression line between estimated and measured values; R2 = coefficient of determination (r^2) of the least squares regression line between estimated and measured values; MBE = mean bias error in same units as the variable; MBE% = mean bias error expressed as a percent of the mean of the observed values; RMSE = root mean square error in same units as the variable; RMSE% = root mean square error expressed as a percent of the mean of the observed values; MOD. = mean of model estimates; MEAS. = mean of observed values; MON. = number of month from which data were derived; %MON. = percent of total months in period of record with data available.

Canopy Wetness Fraction

Canopy wetness fraction (f_w) was estimated as a function of relative humidity using the following statistical model calibrated with leaf wetness sensor data:

$$f_w = \frac{1.4621}{1+e^{-\frac{RH-0.9251}{0.1010}}} \tag{64}$$

where RH is relative humidity (expressed as a ratio rather than a percent). The results of RH estimation and mapping are presented later. The model has an RMSE of 0.2325, and a mean bias error of 0.0010. Estimated mean annual canopy wetness fraction of the Hawaiian Islands is shown in Figure 15.

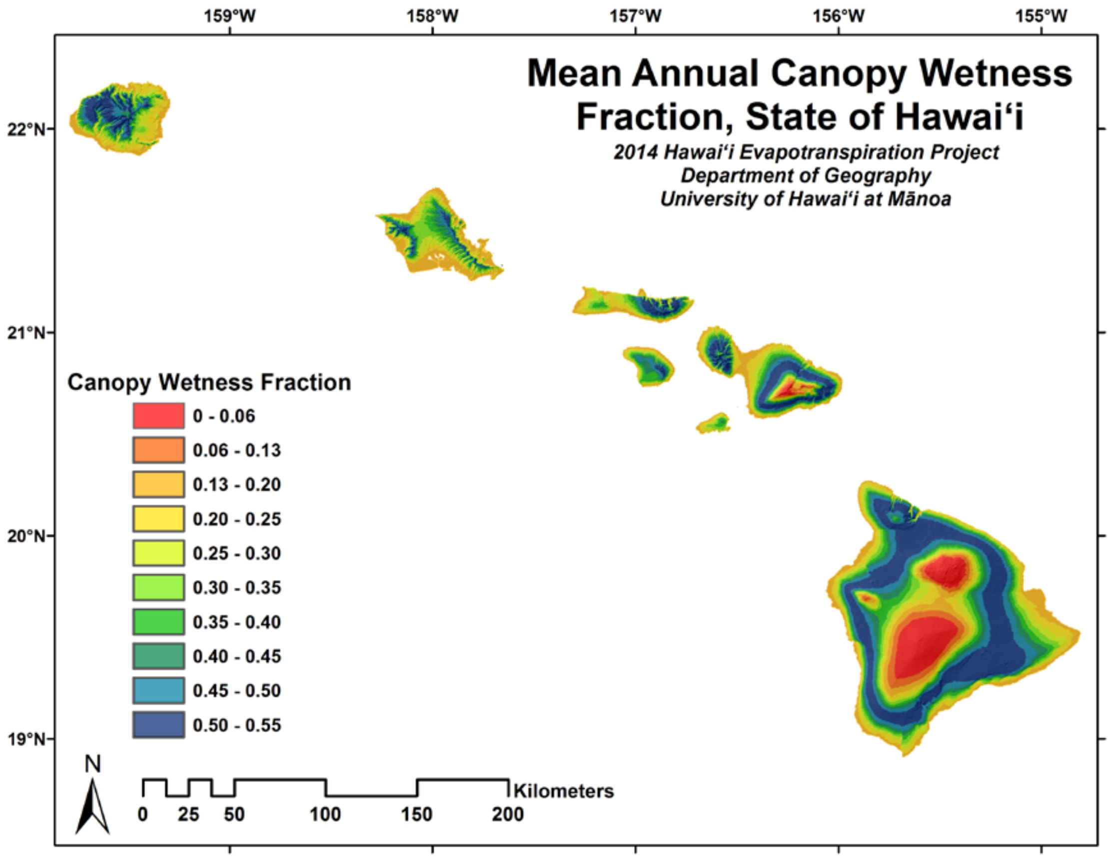

Figure 15. Map of mean annual canopy wetness fraction of Hawaiʻi.

Solar Radiation

Clear-sky Solar Radiation

To evaluate the accuracy of the REST2 clear-sky model, 11 stations were selected (Appendix Table A4). These stations were chosen based on the quality of the available data. We assume that the NREL station data are of the highest quality used in this analysis due to detailed calibration standards enforced at NREL locations (Wilcox and Andreas 2010). In addition, the NREL stations employed two pyranometers at the same location, which can provide some information on instrument error. Cloud free days were identified for a single randomly chosen year (when available) at all of the stations using methods described by Longman et al.

(2012; 2013). Estimated mean annual clear-sky solar radiation of the Hawaiian Islands is shown in Figure 16. For validation purposes, modeled clear-sky results are compared with solar radiation measured during cloud-free periods between the hours of 8 am and 5 pm HST at stations not used in model development (Figure 17 and Table 2).

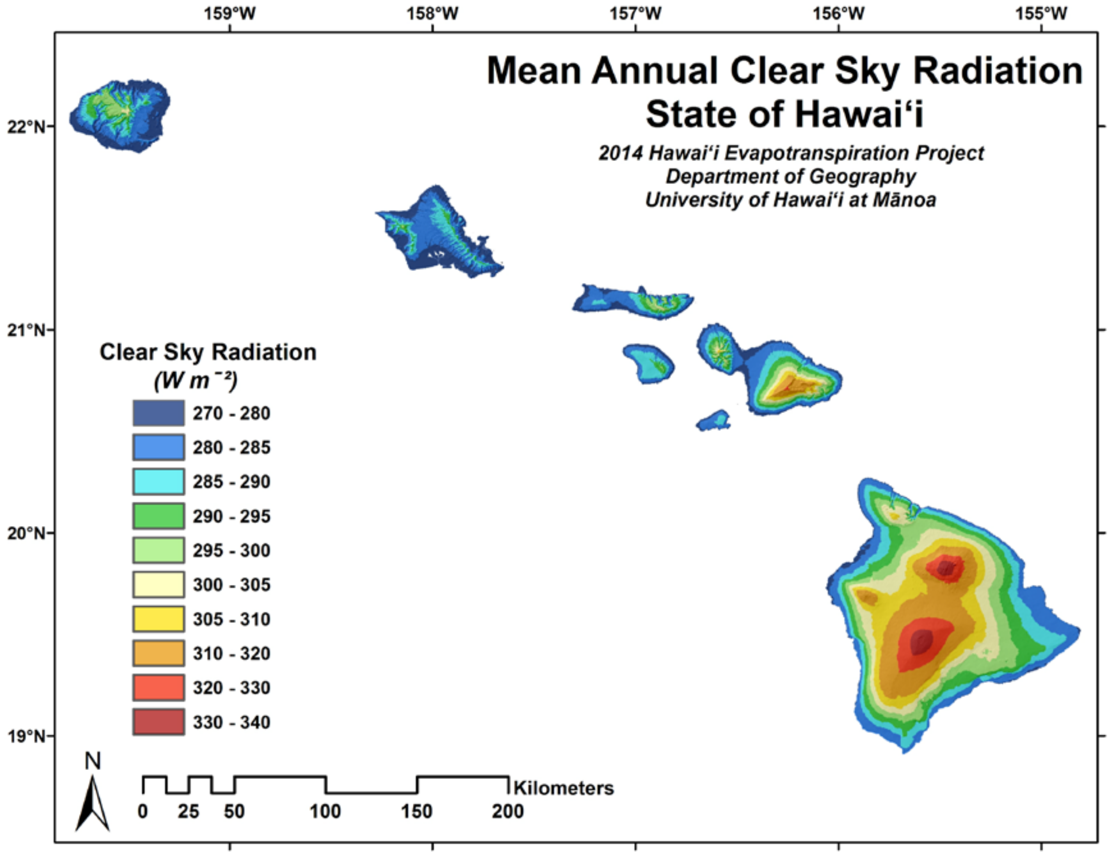

Figure 16. Map of mean annual clear-sky solar radiation of Hawaiʻi .

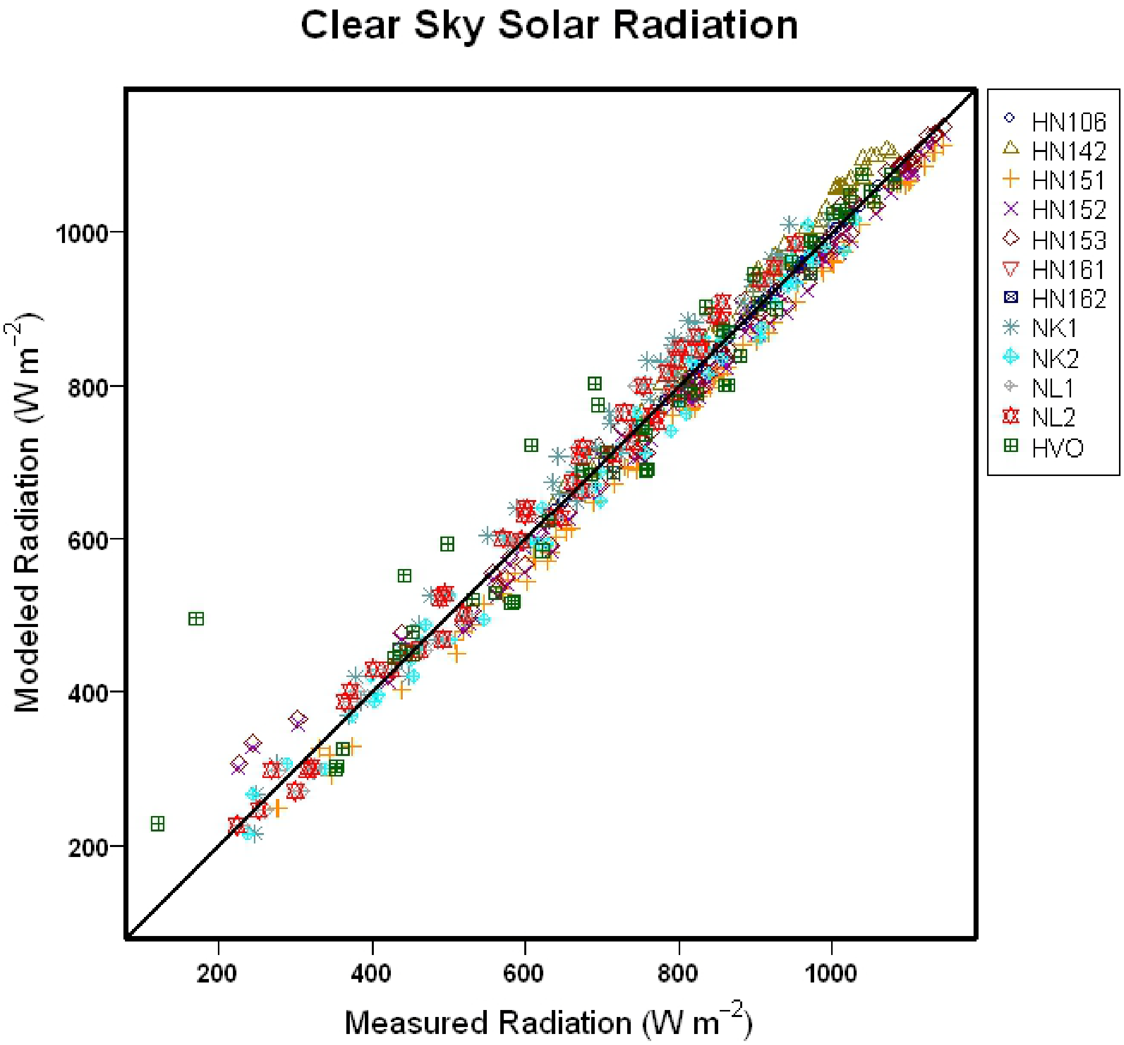

Figure 17. Scatterplot of estimated (mapped) versus measured mean hourly clear-sky solar radiation.

Table 2. Statistical results of estimated (mapped) versus measured clear-sky solar radiation.

STA. ID	N	b	a	R2	MBE	MBE%	RMSE	RMSE%	MOD.	MEAS.	#Days.
All.O	503	1.05	-27	0.96	15	2	30	3	908	893	7627
HN106	60	1.14	-83	0.97	44	5	52	6	921	877	148
HN142	55	1.10	-61	0.99	27	3	31	3	933	905	123
HN151	60	1.08	-71	1.00	6	1	13	1	934	928	1615
HN152	60	1.09	-59	1.00	21	2	24	3	948	927	2910
HN161	60	1.07	-67	0.99	-3	0	15	2	946	950	1781
HN162	60	1.13	-118	0.99	1	0	18	2	936	936	1051
NK1	34	1.02	17	0.94	31	4	41	5	846	814	13
NK2	34	0.99	5	0.93	-5	-1	28	3	846	851	13
NL1	25	1.10	-56	0.96	23	3	32	4	790	768	6
NL2	25	1.12	-75	0.96	19	2	30	4	790	771	6
HVO	30	1.10	-94	0.95	-6	-1	33	4	906	912	6

See Table 1 for definitions of column headings.

Diffuse Radiation

The relationship between the diffuse radiation fraction and an index of cloudiness (1 minus global radiation to clear-sky radiation) is shown in Figure 18. Based on this relationship, the following linear model was used to estimate diffuse radiation for the purpose of implementing terrain shading in the solar radiation model:

$$K_{diffuse} = K_{global} \cdot (1.261 - 1.130 \cdot C_{solar}) \tag{65}$$

where K_{diffuse} is diffuse solar radiation, K_{global} is global solar radiation, and C_{solar} is the ratio of K_{global} to $K_{clear\text{-}sky}$ derived from satellite-based cloud frequency (see Eq. 66 below). Estimated mean annual diffuse solar radiation of the Hawaiian Islands is shown in Figure 19. For validation purposes, modeled diffuse solar radiation estimates are compared with diffuse solar radiation measured at a station not used in model development (Figure 20 and Table 3).

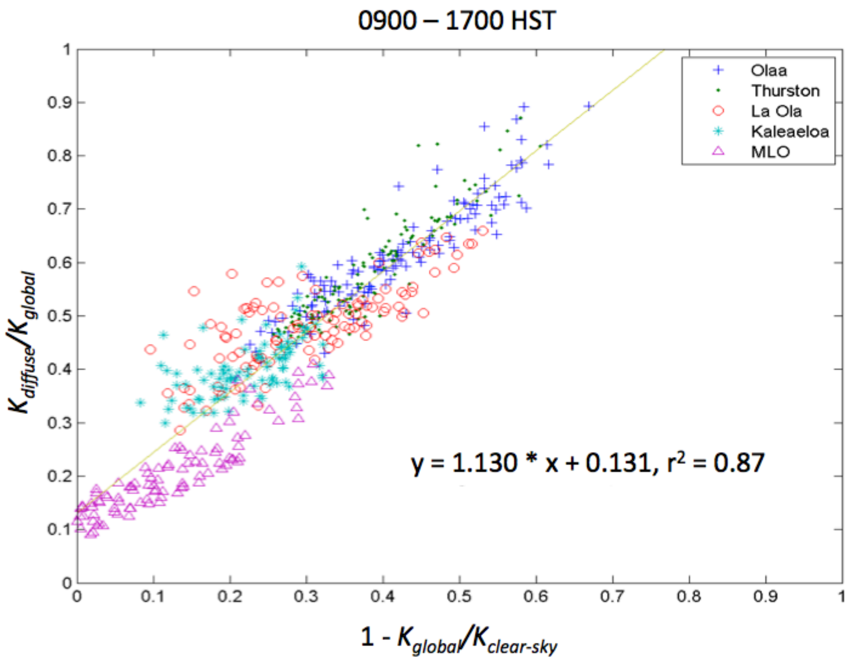

Figure 18. The relationship between the diffuse radiation to global radiation ratio and 1 - C_{solar} (1 - $K_{global}/K_{clear\text{-}sky}$).

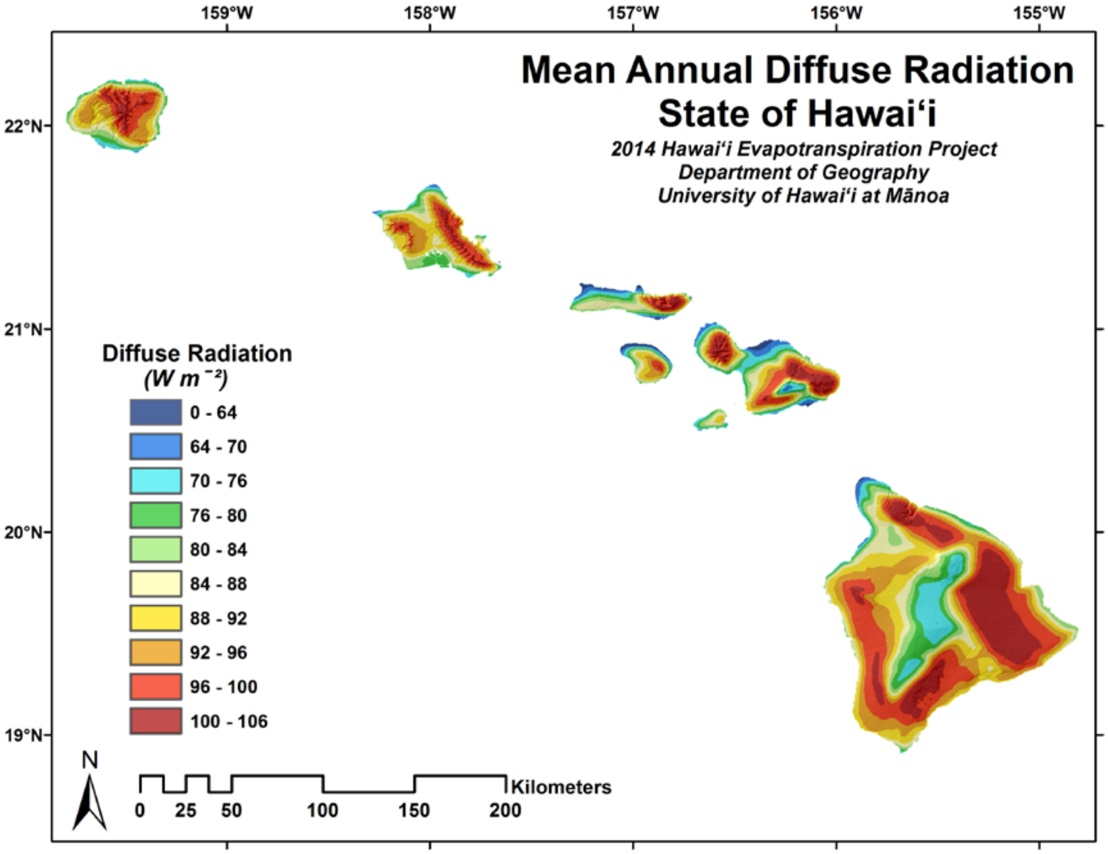

Figure 19. Map of mean annual diffuse solar radiation of Hawaiʻi.

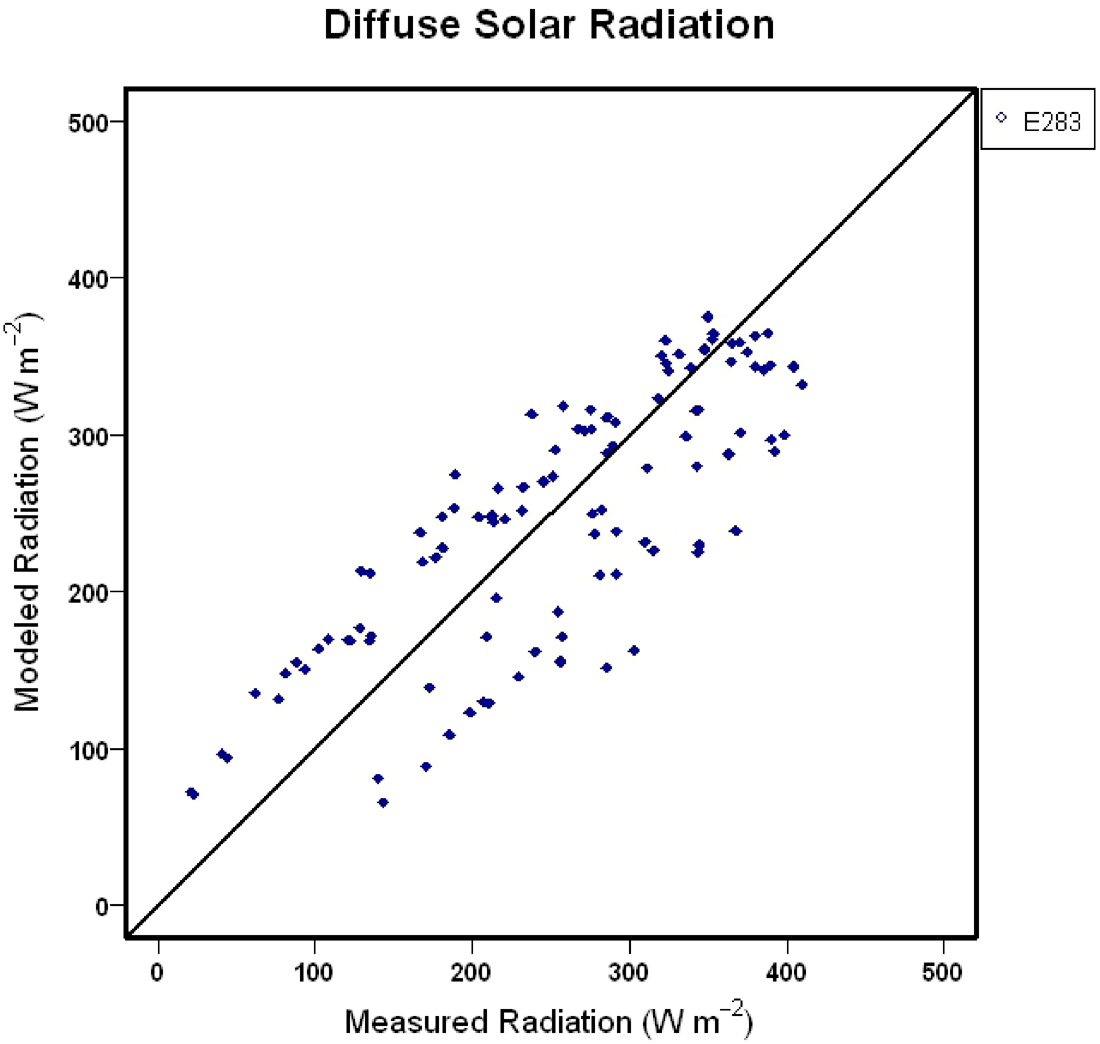

Figure 20. Scatterplot of estimated (mapped) versus measured mean hourly diffuse solar radiation for a station not used in model development. Please note that the measured diffuse radiation plotted here is estimated from diffuse photosynthetically active radiation (*PAR*), which represents a narrower range of the spectrum than solar radiation. However, *PAR* is highly correlated with broadband solar radiation, and hence, is considered a good surrogate for this comparison with model estimates.

Table 3. Statistical results of estimated (mapped) versus measured diffuse solar radiation for a station not used in model development.

STA. ID	N	b	a	r^2	MBE	MBE%	RMSE	RMSE%	MOD.	MEAS.	N_{obs} (mo.)
E283	108	0.68	73	0.64	-8	-3	60	24	244	252	16

See Table 1 for definitions of column headings.

Cloud Frequency

Before fusing the two satellite cloud frequency estimates, each were checked against sky cover observations at Līhuʻe, Honolulu, Kahului, and Hilo airports. Sky cover classes were assigned the following cloud cover fractions: clear: 0.1, few: 0.3, scattered: 0.5, broken, 0.7, and overcast 0.9. These values were averaged by time of day for each month and compared with the satellite cloud frequency from MODIS (120) and GOES (Figure 22) imagery. Results verify the satellite cloud frequency estimates. Estimated mean annual cloud frequency of the Hawaiian Islands is shown in Figure 23.

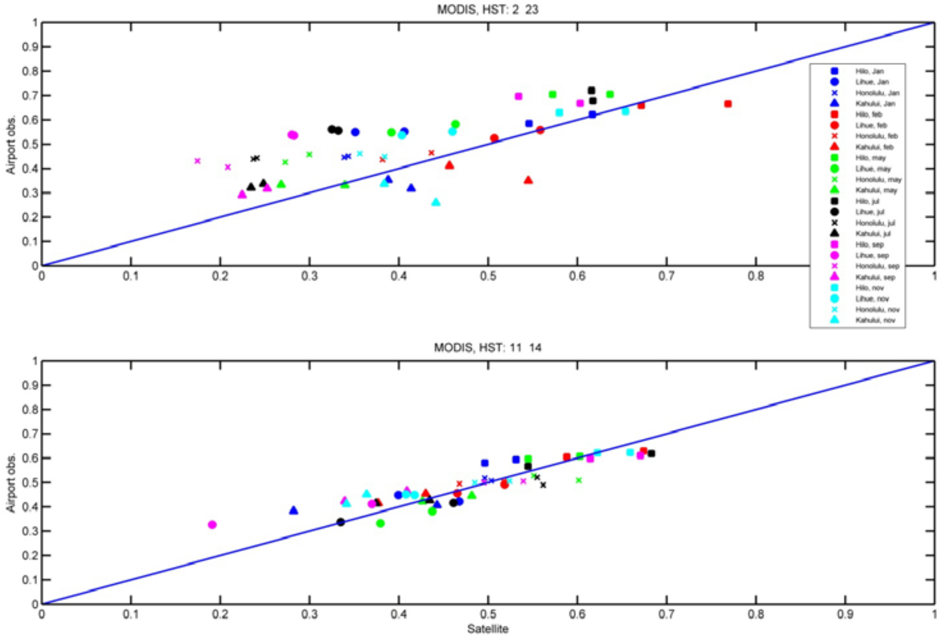

Figure 21. Comparison of MODIS cloud frequency estimates with mean sky cover observations at Līhuʻe, Honolulu, Kahului, and Hilo airport for nighttime (upper panel) and daytime (lower panel) observations.

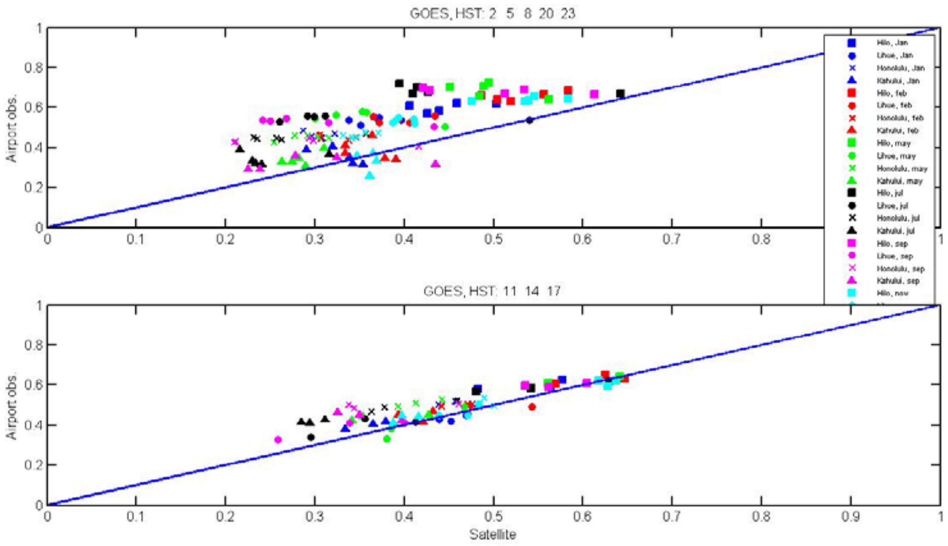

Figure 22. Comparison of GOES cloud frequency estimates with mean sky cover observations at Līhu‘e, Honolulu, Kahului, and Hilo airport for nighttime (upper panel) and daytime (lower panel) observations.

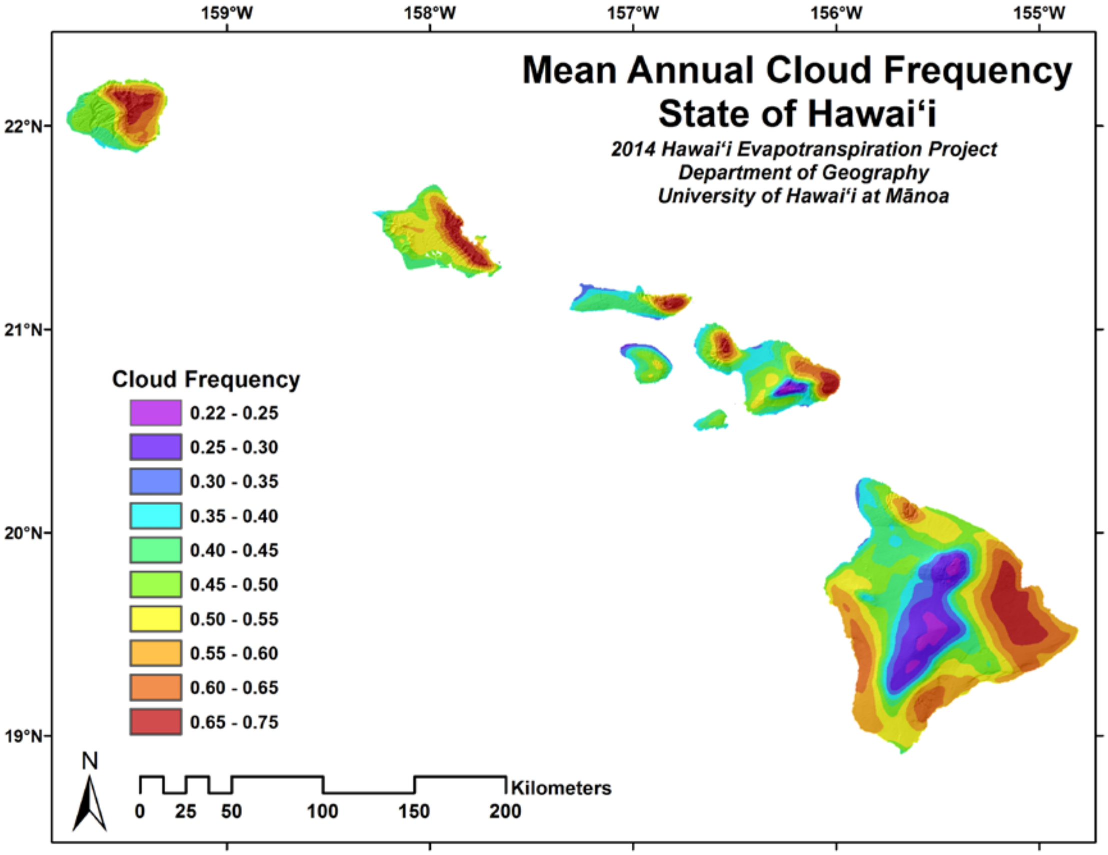

Figure 23. Map of mean annual cloud frequency of Hawai‘i.

Cloud-solar Function

The relationship between C_{solar} (the ratio of K_{global} to $K_{clear\text{-}sky}$), derived from ground-based solar radiation measurements and clear-sky solar estimates, and satellite-derived cloud frequency (CF) is shown in Figure 24 for the months of January and July. Combining mean hourly values from all months (Figure 25), the relationship between C_{solar} and CF can be represented by the function:

$$C_{solar} = 1 - 0.593 \cdot CF^{1.615} \qquad (66)$$

The expression above allows the use of Eq. (6) to estimate solar radiation under all-sky conditions as:

$$K_{global} = (1 - 0.593 \cdot CF^{1.615}) \cdot K_{clear-sky} \qquad (67)$$

where K_{global} is all-sky downward solar (shortwave) radiation, CF is satellite-derived cloud frequency, and $K_{clear\text{-}sky}$ is clear-sky solar radiation estimated using the REST2 clear-sky model. Using this approach, solar radiation was estimated at each gridpoint, for each daylight hour of the mean diurnal cycle of each month.

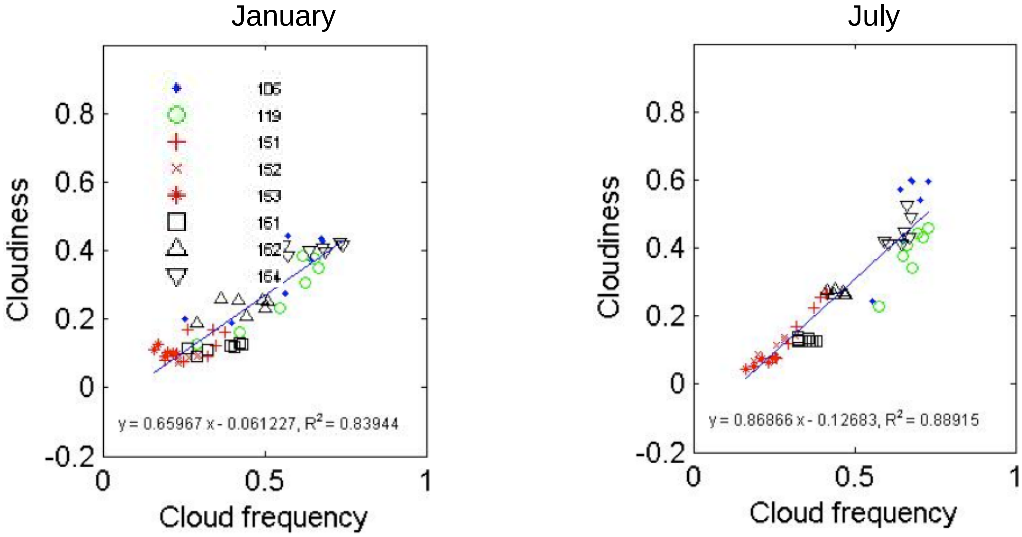

Figure 24. Relationship between mean hourly cloudiness (C = 1 − K_{global}/K_{clear_sky}) and mean hourly satellite-based cloud frequency (CF) for January and July at eight HaleNet stations.

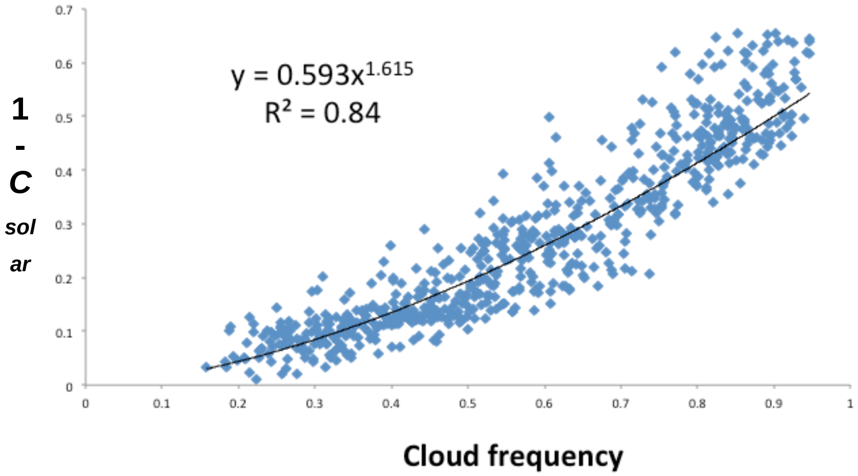

Figure 25. The statistical relationship between the attenuation of solar radiation by clouds, represented by 1 – C_{solar} and satellite-derived cloud frequency (*CF*).

All-sky Solar Radiation

Estimated mean annual solar radiation of the Hawaiian Islands is shown in Figure 26. For validation purposes, modeled solar radiation estimates are compared with solar radiation measured at stations not used in model development (Figure 27 and Table 4).

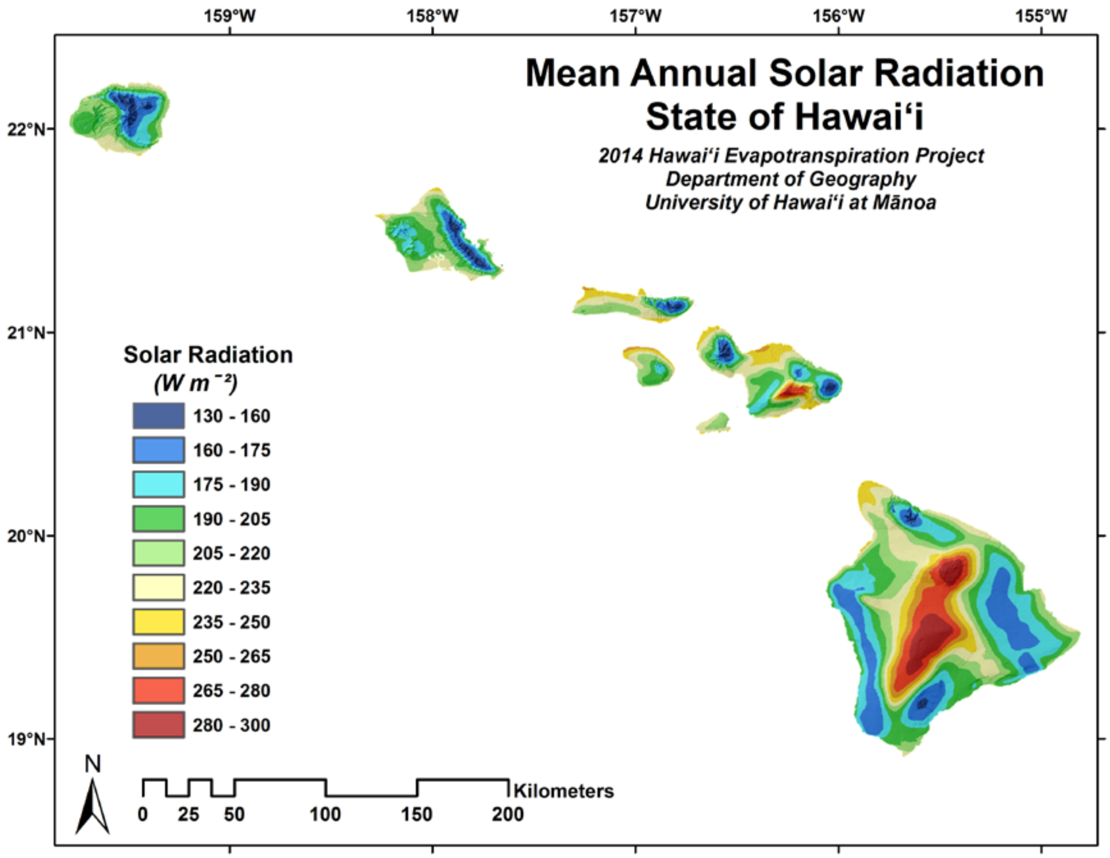

Figure 26. Map of mean annual solar radiation of Hawaiʻi.

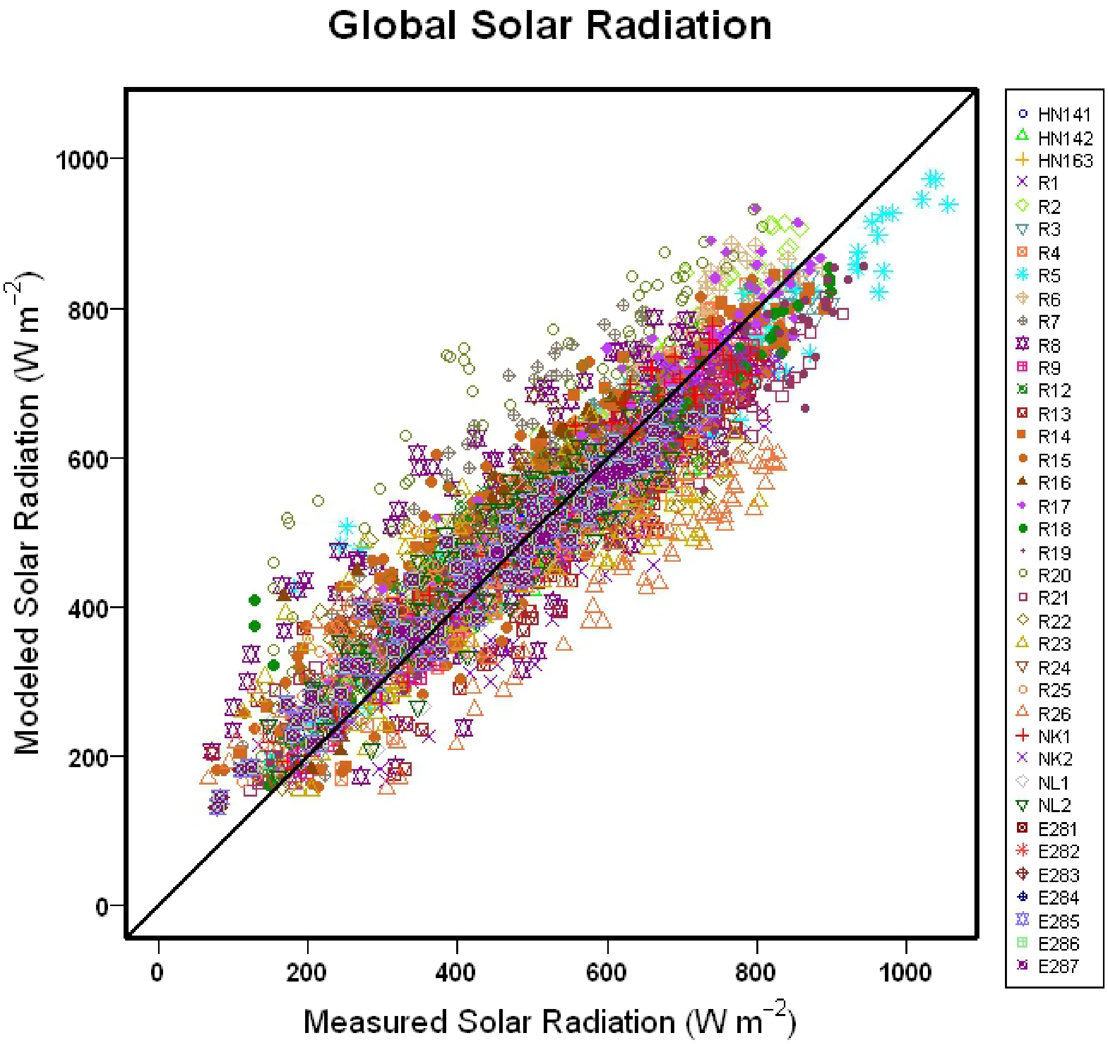

Figure 27. Scatterplot of estimated (mapped) versus measured mean hourly all-sky solar radiation for stations not used in model development.

Table 4. Statistical results of estimated (mapped) versus measured all-sky solar radiation for stations not used in model development.

Sta. ID	N	b	a	r^2	MBE	MBE%	RMSE	RMSE%	Mod.	Meas.	N_{obs} (mo.)
All	4095	0.78	121	0.82	6	1	78	15	521	514	2837
HN141	108	0.83	88	0.92	10	2	39	8	470	463	128
HN142	108	0.78	94	0.89	-19	-4	52	10	495	516	21
HN163	108	0.80	100	0.91	0	0	50	10	499	502	96
R1	108	0.74	114	0.73	-32	-6	94	17	530	564	118
R2	108	0.76	112	0.79	-20	-4	82	15	530	553	120
R3	108	0.87	65	0.97	-6	-1	40	7	551	561	132
R4	108	0.90	65	0.89	11	2	59	11	561	552	104
R5	108	0.77	130	0.92	-11	-2	76	12	603	614	59
R6	108	1.01	47	0.97	50	9	60	11	578	532	100
R7	108	0.96	111	0.77	91	20	118	26	550	462	100
R8	108	0.65	222	0.61	40	8	122	23	558	520	92
R9	108	0.92	20	0.97	-21	-4	36	7	522	546	112
R12	108	0.80	129	0.91	40	9	63	14	494	457	80
R13	108	0.71	128	0.79	-31	-6	87	16	521	554	88
R14	108	0.85	98	0.9	17	3	64	12	555	539	21
R15	108	0.78	141	0.80	31	6	95	19	529	502	81
R16	108	0.89	77	0.85	25	5	58	12	509	487	80
R17	108	0.93	67	0.95	27	5	53	9	606	582	89
R18	108	0.79	111	0.95	-3	0	56	10	543	549	132
R19	108	0.80	82	0.95	-37	-6	70	11	564	606	105
R20	108	0.86	185	0.72	115	23	154	31	603	491	117
R21	108	0.74	107	0.96	-39	-7	74	13	520	562	132
R22	108	0.67	160	0.75	0	0	84	17	493	493	65
R23	108	0.55	187	0.62	-34	-7	109	22	456	492	96
R24	108	0.82	97	0.92	16	3	46	10	467	454	100
R25	108	0.71	137	0.87	13	3	59	13	448	438	92
R26	108	0.49	176	0.73	-109	-19	159	28	451	562	98
NK1	108	0.94	33	0.95	-2	0	35	7	535	540	18
NK2	108	0.90	34	0.95	-23	-4	44	8	535	562	18
NL1	108	0.77	116	0.83	6	1	56	12	480	473	28
NL2	108	0.77	118	0.83	11	2	57	12	480	469	28
E281	108	0.82	89	0.95	5	1	42	9	458	457	31
E282	99	0.78	129	0.90	18	4	66	13	531	512	11
E283	108	0.83	110	0.95	28	6	50	10	519	495	38
E284	108	0.78	103	0.92	-26	-4	68	12	555	585	19
E285	108	0.53	267	0.75	29	6	143	28	536	511	30
E286	108	0.82	66	0.91	-13	-3	39	9	421	437	36
E287	108	0.68	148	0.91	5	1	63	14	458	457	22

See Table 1 for definitions of column headings.

Albedo

Monthly albedo was mapped at 250-m resolution by estimating mean monthly albedo for each land cover type. A linear least-squares model was optimized with respect to mean monthly 1-km MODIS albedo values (Eq. 9). Optimization statistics are shown in Table 5. Albedo estimates for each HIGAP land cover class (HIGAP land cover classes shown in Appendix Table A6) are shown in Table 6. Estimated mean annual albedo of the Hawaiian Islands is shown in Figure 28.

Table 5. R^2 and MSE of the regression for each month are shown as follows.

Month	R^2	MSE
1	0.7431	2.8227
2	0.7523	2.7950
3	0.7525	2.8098
4	0.7534	2.8408
5	0.7527	2.9027
6	0.7493	2.9681
7	0.7416	2.8861
8	0.7232	2.9039
9	0.7216	2.7904
10	0.7195	2.6837
11	0.7248	2.6182
12	0.7296	2.6614

Table 6. Estimates of monthly albedo by land cover type.

Land cover code[1]	Jan	Feb	Mar	Apr	May	Jun	Jul	Aug	Sep	Oct	Nov	Dec
0	6.1	6.3	6.5	6.6	6.7	6.8	7.2	7.2	6.8	6.7	6.4	6.5
1	9.0	9.8	10.8	11.4	11.7	11.7	11.2	10.3	9.6	9.2	9.2	9.8
2	10.8	11.5	12.0	12.5	12.7	12.6	11.9	11.3	11.1	11.2	11.4	12.2
3[2]	-	-	-	-	-	-	-	-	-	-	-	-
4	12.0	8.4	7.8	8.1	7.5	8.3	8.5	8.9	8.3	16.2	10.2	8.9
5	9.0	9.3	9.3	9.4	9.4	9.4	10.0	10.2	9.6	9.1	8.9	9.7
6	12.2	11.2	11.2	12.1	13.1	14.1	14.3	13.1	11.5	10.7	10.7	11.9
7	8.4	9.1	9.3	9.4	9.3	9.3	9.4	9.8	9.5	8.8	9.2	9.7
8	8.2	8.7	9.0	9.1	9.1	9.1	9.3	9.2	8.9	8.4	8.0	8.1
9	9.5	10.9	11.9	12.6	13.0	13.0	12.8	12.1	11.2	10.3	9.6	9.4
10[2]	-	-	-	-	-	-	-	-	-	-	-	-
11	16.4	16.9	17.3	17.7	18.0	18.3	18.1	17.6	16.8	15.6	14.9	14.8
12	9.3	10.7	11.4	11.6	11.5	11.6	11.7	11.5	10.6	9.4	8.6	8.2
13	10.3	10.8	11.2	11.4	11.5	11.6	11.8	11.8	11.3	10.6	10.1	9.8
14	9.2	9.7	10.0	10.2	10.2	10.2	10.5	10.5	10.0	9.3	8.9	8.9
15[2]	-	-	-	-	-	-	-	-	-	-	-	-
16	15.7	16.1	15.4	14.5	13.5	13.5	13.7	12.2	14.6	13.3	14.1	15.6
17	8.8	9.5	9.5	9.8	9.8	9.9	9.8	9.6	9.4	9.3	9.0	8.8
18	6.0	6.7	7.9	8.8	9.8	10.4	11.4	11.0	10.4	9.6	8.0	5.0
19	12.9	13.3	14.0	14.9	15.8	16.5	16.7	16.1	15.3	14.4	13.4	12.5
20[2]	10.9	11.7	12.2	12.6	12.8	12.9	12.9	12.1	11.3	10.5	10.3	11.1
21	-	-	-	-	-	-	-	-	-	-	-	-
22	9.4	10.0	10.3	10.4	10.3	10.3	10.6	10.6	10.1	9.7	9.6	9.7
23	11.8	12.5	12.9	13.1	13.1	13.0	13.0	12.9	12.4	11.9	11.6	11.6
24	11.1	11.8	12.2	12.5	12.6	12.6	13.0	13.1	12.6	12.0	11.4	11.2
25	10.3	11.2	11.8	12.6	13.2	13.7	14.6	14.5	13.5	12.5	12.2	11.8
26	14.5	15.3	16.3	16.9	17.4	17.8	17.8	17.4	16.6	15.7	15.0	14.5
27	14.8	15.4	15.8	16.1	16.2	16.4	16.2	15.8	15.2	14.6	14.2	14.2
28	12.9	13.1	13.5	13.8	14.1	14.3	14.0	13.7	13.1	12.6	12.2	12.2
29	12.5	13.4	13.9	14.2	14.2	14.1	13.9	13.5	13.0	12.5	12.2	12.4
30	16.3	16.9	17.1	17.2	17.2	17.2	17.2	16.8	16.4	15.9	15.6	15.8
31	12.2	13.0	13.2	13.3	13.4	13.3	13.5	13.3	12.6	11.9	11.8	12.5
32	13.1	13.8	14.4	14.9	15.3	15.5	15.4	15.0	14.4	13.7	13.1	12.9
33	10.7	11.2	11.2	11.3	11.4	11.4	11.7	11.6	11.1	10.6	10.3	10.9
34	14.7	15.0	15.2	15.0	14.6	14.7	15.2	15.7	15.4	14.9	14.3	13.8
35	9.0	9.5	9.6	9.4	9.1	8.8	9.7	10.4	10.0	9.8	9.8	10.3
36	7.6	9.1	10.1	10.9	11.5	11.7	12.6	12.1	10.5	8.8	7.7	8.2
37	5.5	5.9	6.2	6.3	6.4	6.4	6.6	6.6	6.4	6.2	5.8	5.7

[1] HIGAP land cover classes are given in Appendix Table A6 . [2] Land cover types 3, 10, 15, and 21, each representing less than 0.003% of the total land area, had insufficient sample sizes to estimate their albedo values. Albedo values of similar land cover types were substituted for those classes.

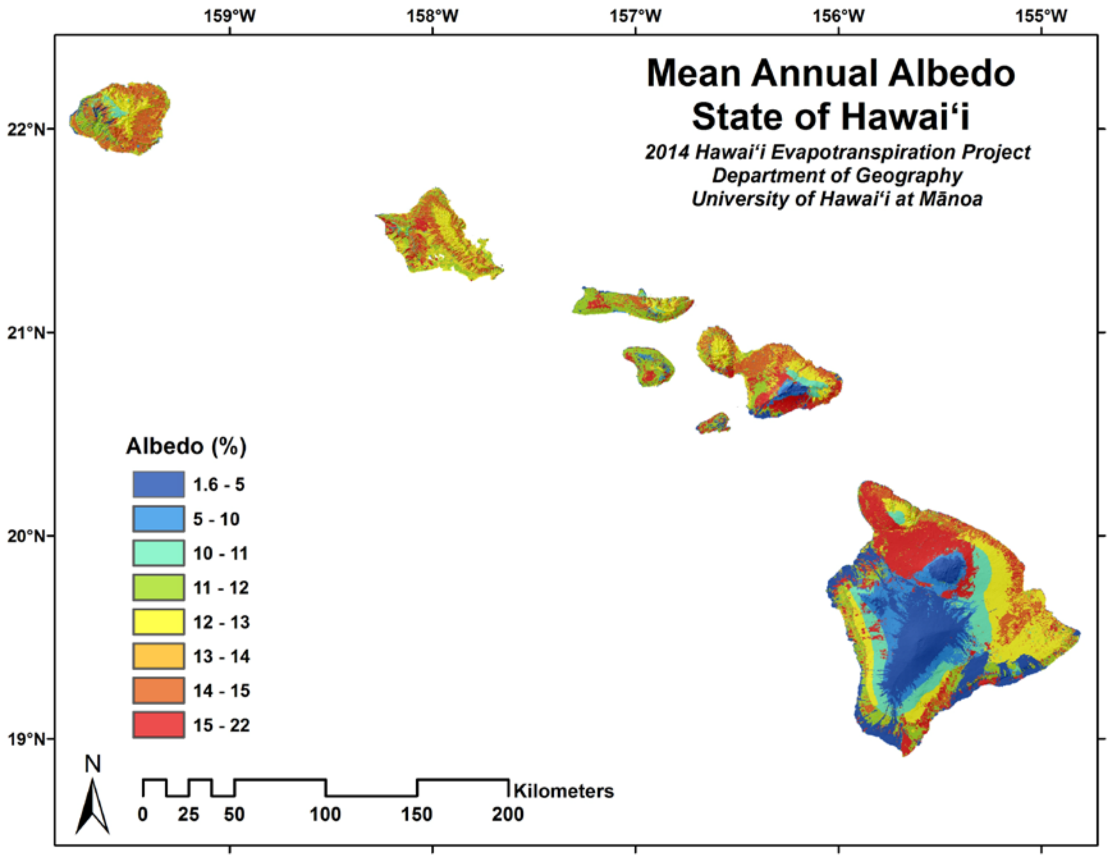

Figure 28. Map of mean annual albedo (250 m resolution) of Hawaiʻi.

As check of the use of albedo disaggregated, based on land cover, to 250-m from the 1-km MODIS values, the 250-m albedo estimates were aggregated to the 1-km scale and compared with the MODIS estimates (Figure 29). For validation purposes, albedo estimates are compared with measured albedo (Figure 30 and Table 7). No ground station data were used in developing albedo estimates.

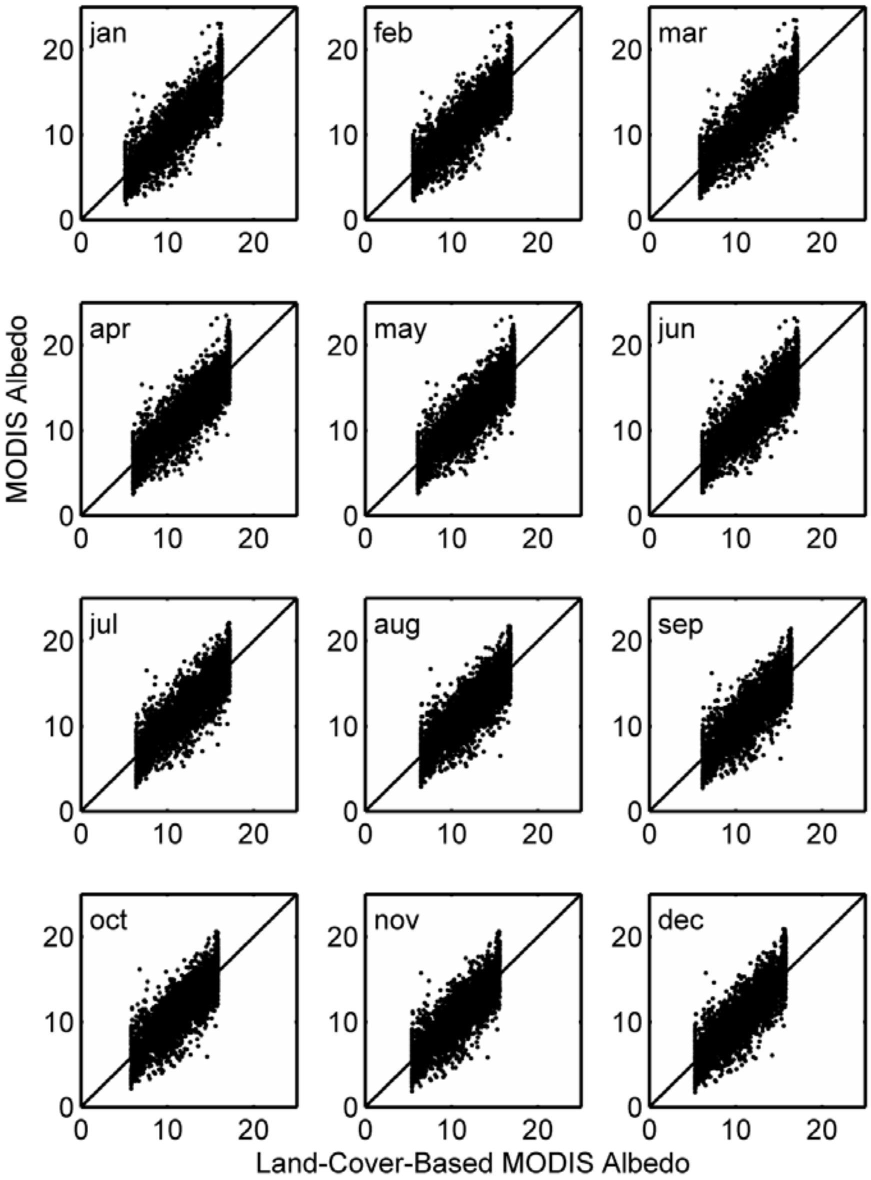

Figure 29. Scatterplots of estimated albedo (%), based on the land cover distribution in each pixel, vs. MODIS albedo for each month.

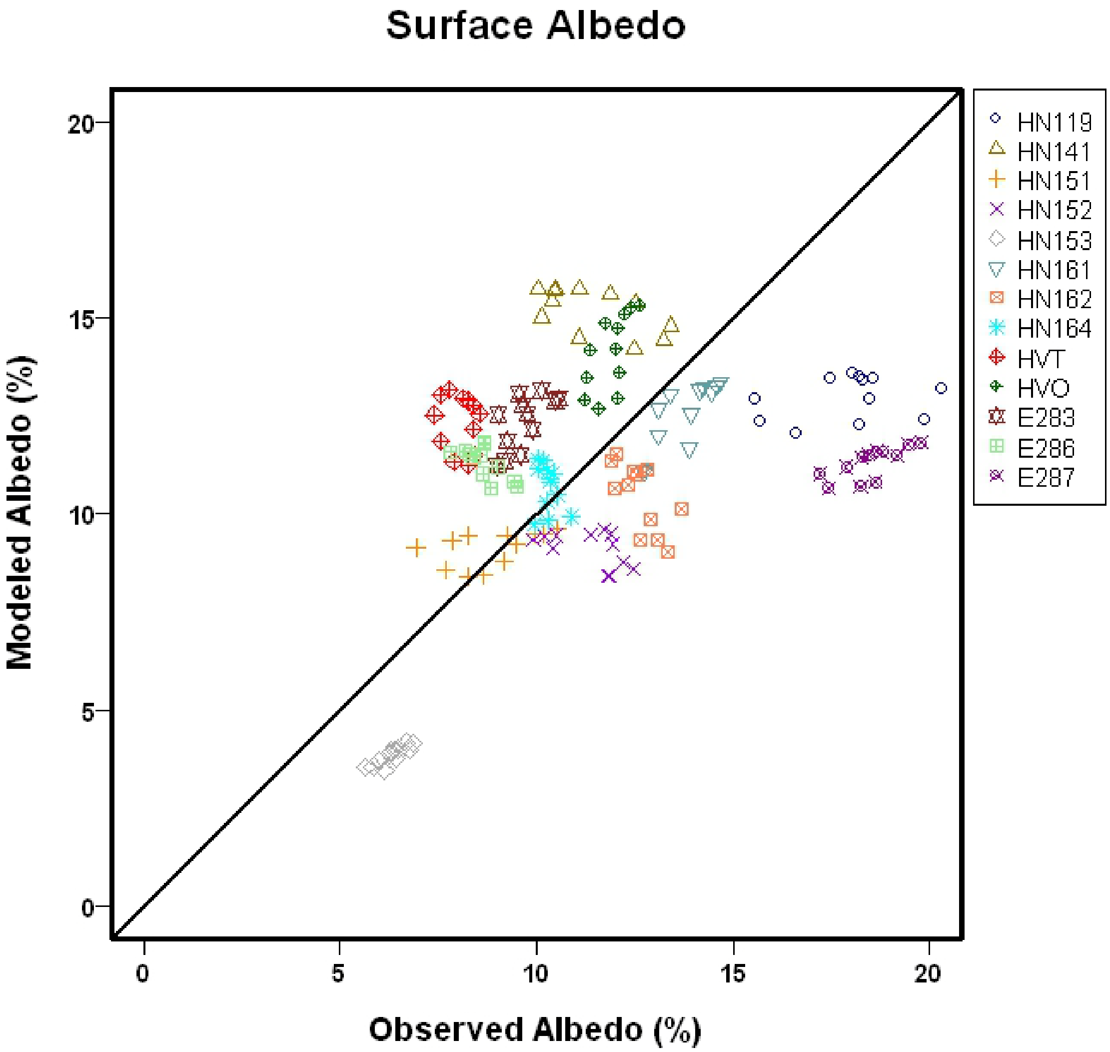

Figure 30. Scatterplot of estimated (mapped) versus measured mean monthly albedo for all available observing stations.

Table 7. Statistical results of estimated versus measured mean monthly albedo for all available observing stations.

Sta. ID	N	b	a	r^2	MBE	MBE%	RMSE	RMSE%	Mod.	Meas.	N_{obs} (mo.)
All	156	0.33	7.4	0.18	0	-3	3	30	11	11	283
HN119	12	0.10	11.2	0.07	-5	-28	5	29	13	18	12
HN141	12	-0.27	18.3	0.34	4	33	4	35	15	11	12
HN151	12	0.19	7.4	0.23	0	3	1	11	9	9	12
HN152	12	-0.25	11.9	0.24	-2	-20	3	22	9	11	12
HN153	12	0.57	0.3	0.74	-2	-39	2	39	4	6	12
HN161	12	0.94	-0.3	0.63	-1	-9	1	10	13	14	12
HN162	12	-1.05	23.8	0.45	-2	-18	3	20	10	13	12
HN164	12	-0.70	17.8	0.09	0	4	1	8	11	10	12
HVT	12	-0.30	14.7	0.03	4	53	4	54	12	8	40
HVO	12	1.39	-2.4	0.43	2	19	2	20	14	12	51
E283	12	0.86	4.0	0.42	3	27	3	28	12	10	38
E286	12	-0.59	16.4	0.48	3	30	3	32	11	9	36
E287	12	0.39	4.0	0.53	-7	-39	7	39	11	19	22

See Table 1 for definitions of column headings.

Downward Longwave Radiation

Downward longwave radiation was modeled using Eq. (10). Clear-sky downward longwave radiation ($L_{down\_clear\_sky}$) based on Eq. (11) was estimated using the vertical distribution of precipitable water from Longman et al. (2013). A statistical relationship was then derived for C_{LW}, the ratio of L_{down} to $L_{down\_clear\_sky}$, and cloud frequency (CF):

$$C_{LW} = 1 + 0.202 \cdot CF^{0.836} \tag{68}$$

Based on Eq. (10), the following model was used to map L_{down}:

$$L_{down} = L_{down\_clear\_sky} \cdot (1 + 0.202 \cdot CF^{0.836}) \tag{69}$$

A comparison between measured and estimated L_{down} for stations used in the calibration of the cloud frequency effect is shown in Figure 31. Estimated mean annual downward longwave radiation of the Hawaiian Islands is shown in Figure

32. For validation purposes, modeled downward longwave radiation estimates are compared with downward longwave radiation measured at stations not used in model development (Figure 33 and Table 8).

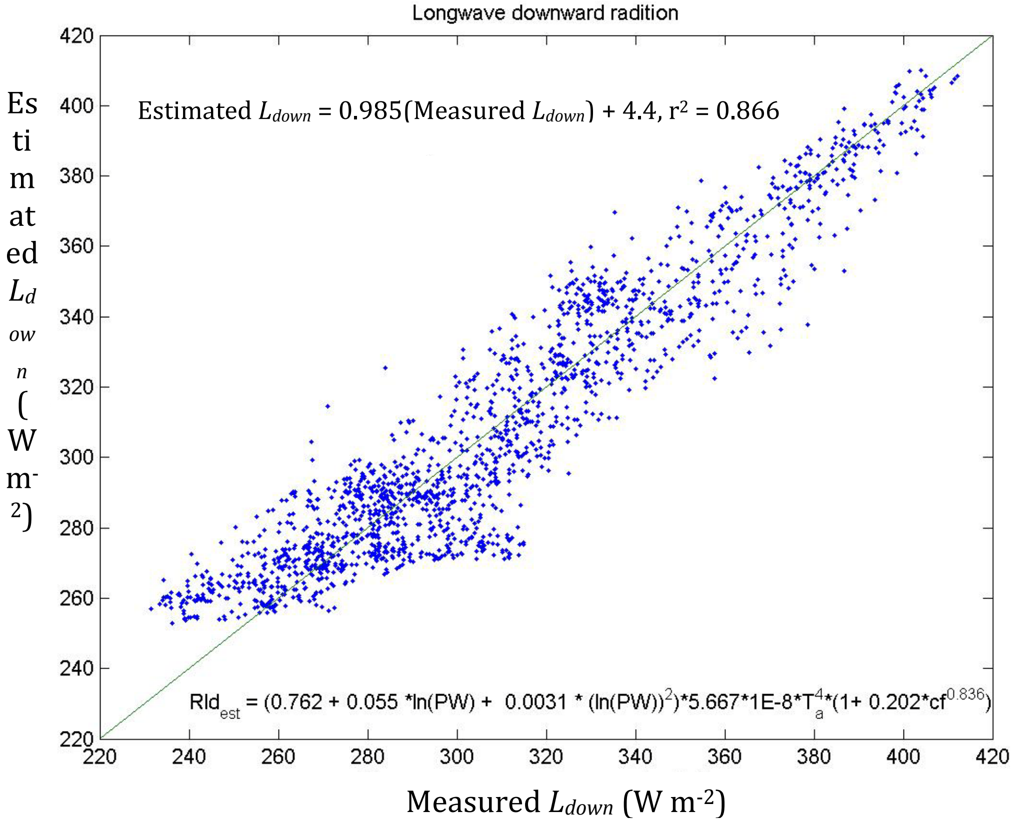

Figure 31. Scatterplot of estimated versus measured downward longwave radiation.

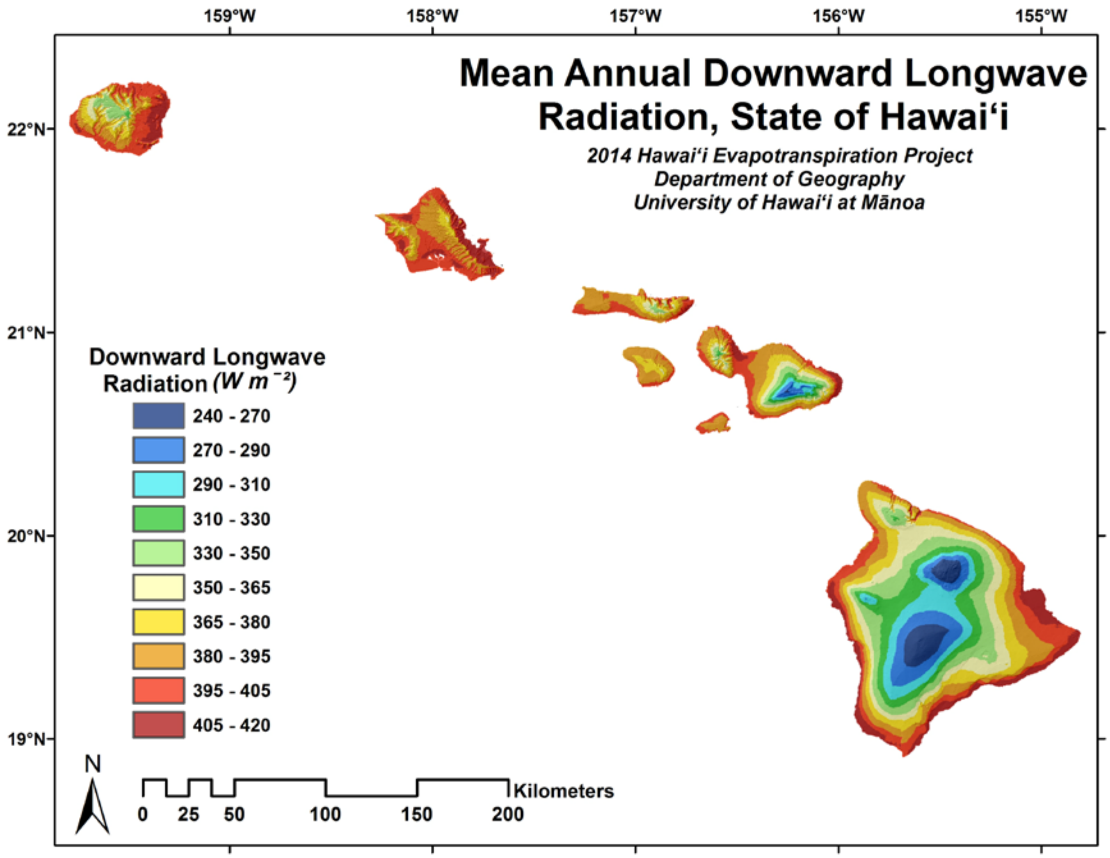

Figure 32. Map of mean annual downward longwave radiation of Hawai'i.

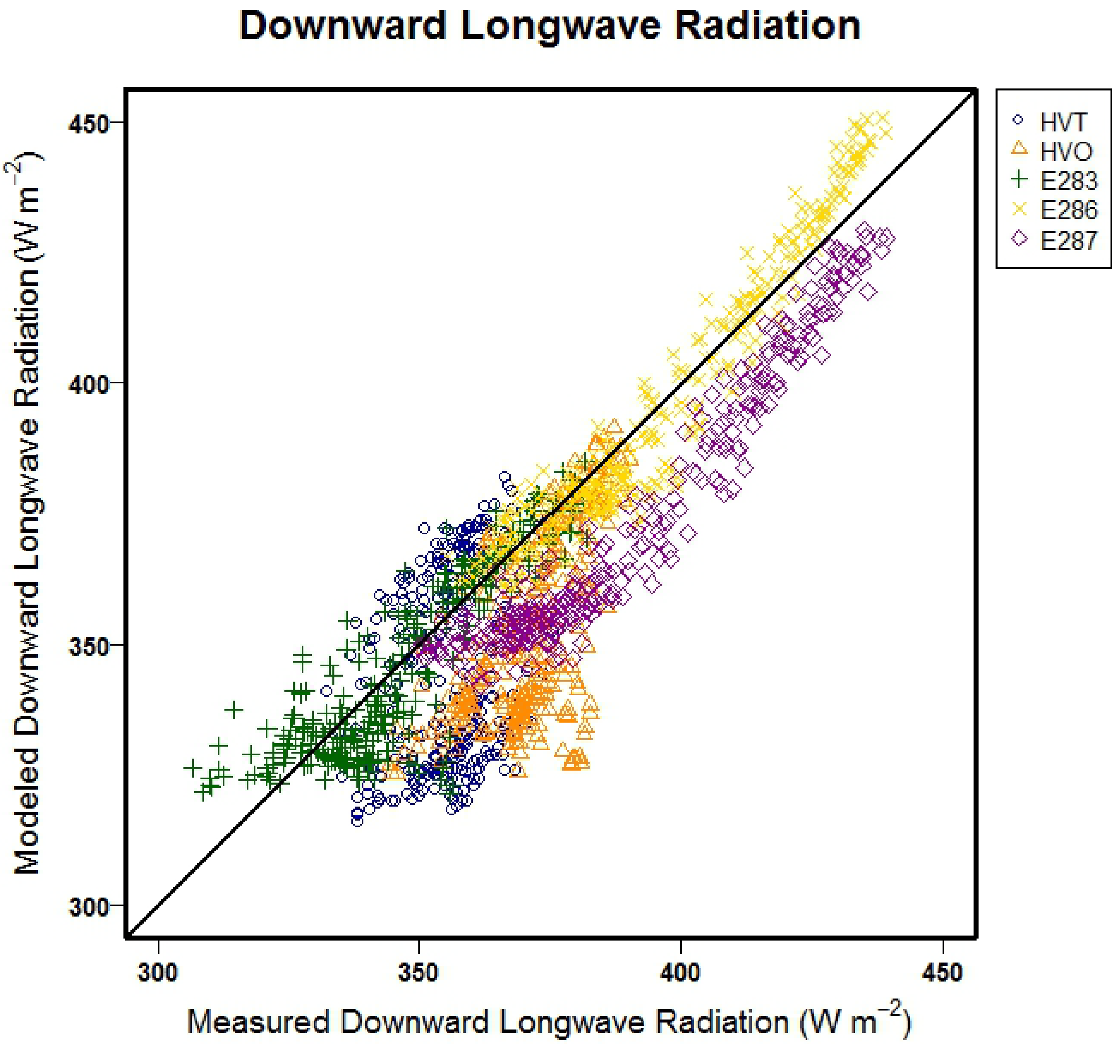

Figure 33. Scatterplot of estimated (mapped) versus measured mean hourly downward longwave radiation for stations not used in model development.

Table 8. Statistical results of estimated (mapped) versus measured downward radiation for stations not used in model development.

Sta. ID	N	b	a	r^2	MBE	MBE%	RMSE	RMSE%	Mod.	Meas.	N_{obs} (mo.)
All	1440	0.98	-1	0.77	-9	-2	17	5	363	372	167
HVT	288	0.58	142	0.04	-7	-2	24	7	348	355	40
HVO	288	1.19	-90	0.40	-18	-5	23	6	354	371	48
E283	288	0.86	47	0.71	-1	0	9	3	345	345	37
E286	288	1.12	-49	0.93	0	0	7	2	396	397	20
E287	288	1.01	-19	0.92	-16	-4	18	4	375	391	22

See Table 1 for definitions of column headings.

Upward Longwave Radiation

Upward longwave radiation was modeled using Eqs. (15-16). Parameter values were derived for each calibration station (Appendix Table A3), and then averaged for three broad land cover groups (Table 9). Estimated mean annual upward longwave radiation of the Hawaiian Islands is shown in Figure 34. For validation purposes, modeled upward longwave radiation estimates are compared with upward longwave radiation measured at stations not used in model development (Figure 35 and Table 10).

Table 9. Parameter values for the upward longwave radiation model Eqs. (15-16).

Forest

Month	b_0		b_1		i_0		σ^2	
	mean	s.d.	mean	s.d.	mean	s.d.	mean	s.d.
1	-0.290	0.980	1.873	0.113	12.897	0.492	13.297	3.380
2	-0.410	0.921	1.887	0.252	12.923	0.379	14.340	2.789
3	-0.190	0.814	1.620	0.189	13.205	0.564	14.980	1.743
4	-0.310	0.780	2.363	0.705	13.018	0.459	18.440	2.855
5	-0.538	0.397	1.953	0.231	12.888	0.609	17.475	3.033
6	-0.533	0.442	1.958	0.246	12.925	0.415	18.355	4.726
7	-0.663	0.417	2.120	0.222	13.048	0.536	18.848	4.403
8	-0.560	0.345	1.915	0.167	13.150	0.576	16.583	4.461
9	-0.803	0.328	2.215	0.360	12.830	0.503	16.625	2.967
10	-0.883	0.278	1.840	0.163	12.553	0.246	16.350	0.913
11	-0.710	0.485	1.437	0.125	12.580	0.257	13.613	0.539
12	-0.697	0.572	1.597	0.120	13.003	0.394	14.870	2.090

Grass/shrub

Month	b_0		b_1		i_0		σ^2	
	mean	s.d.	mean	s.d.	mean	s.d.	mean	s.d.
1	-2.556	1.039	10.590	0.305	13.668	0.399	14.074	1.557
2	-2.130	0.641	10.272	0.711	13.676	0.320	16.290	1.395
3	-1.880	0.525	9.940	1.352	13.560	0.429	17.488	2.084
4	-2.338	1.055	11.454	2.887	13.300	0.363	21.452	2.294
5	-1.776	0.382	9.786	1.593	13.328	0.523	22.088	1.964
6	-1.632	0.692	10.950	2.600	13.322	0.431	21.586	2.318
7	-1.958	0.755	12.532	2.510	13.482	0.589	21.892	2.552
8	-2.168	0.793	13.382	1.437	13.432	0.507	20.542	2.263
9	-2.218	0.744	12.088	0.829	13.234	0.472	18.690	1.835
10	-1.968	0.739	10.354	0.823	13.112	0.425	16.572	1.712
11	-1.846	0.582	8.666	1.353	13.202	0.402	14.378	1.691
12	-1.946	0.702	8.052	2.077	13.468	0.376	13.836	2.221

Bare soil

Month	b_0		b_1		i_0		σ^2	
	mean	s.d.	mean	s.d.	mean	s.d.	mean	s.d.
1	-4.750	0.470	22.425	1.475	14.035	0.205	14.065	0.175
2	-4.015	0.495	20.840	0.100	14.035	0.175	15.500	0.340
3	-3.105	0.095	18.800	0.570	14.030	0.240	17.285	0.415
4	-4.470	0.373	31.350	1.445	13.540	0.230	21.060	1.521
5	-3.025	0.325	24.455	2.655	13.960	0.260	20.935	2.385
6	-3.395	0.575	27.855	2.455	13.855	0.245	21.175	2.945
7	-4.015	0.695	31.070	2.560	14.065	0.295	21.320	2.970
8	-4.860	0.860	32.120	3.240	13.980	0.290	21.265	2.535
9	-5.385	0.985	31.540	3.450	13.750	0.220	19.090	1.040
10	-4.655	0.745	26.225	1.375	13.620	0.180	16.215	0.855
11	-3.660	0.830	17.010	1.110	13.690	0.210	14.525	0.485
12	-3.700	0.660	15.715	0.415	13.840	0.220	12.830	0.010

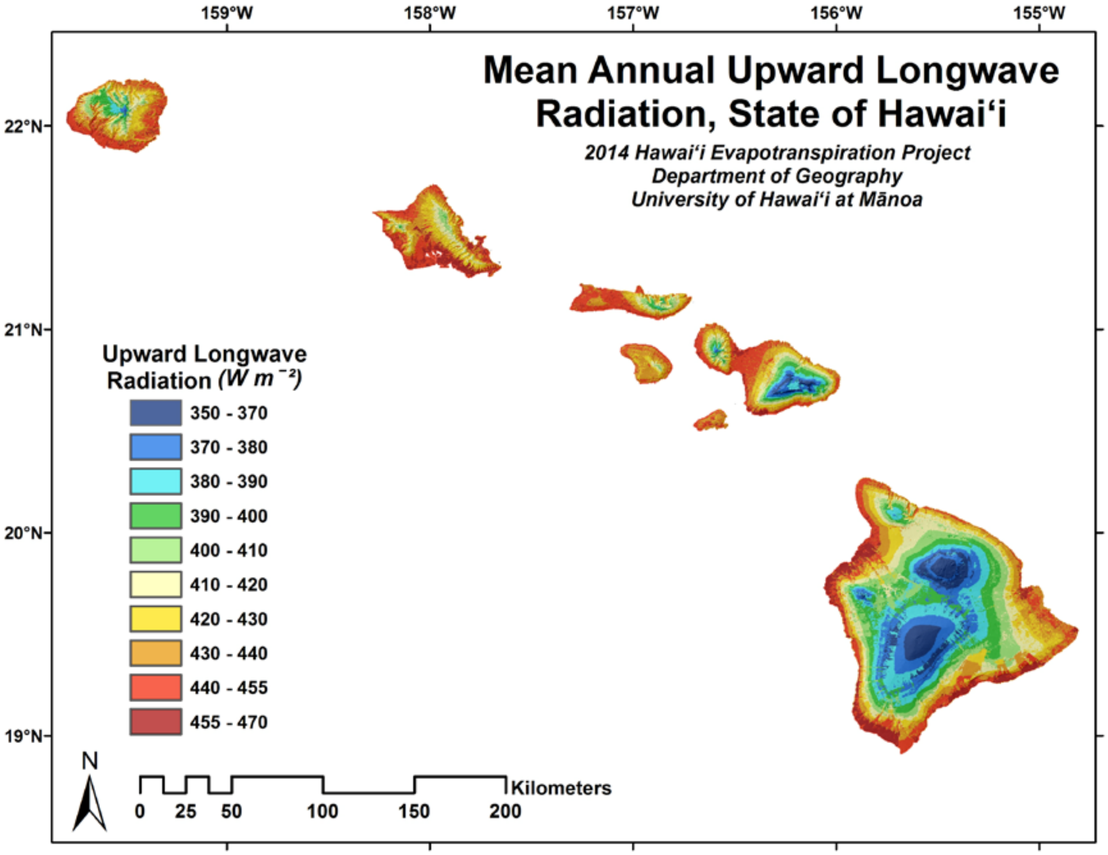

Figure 34. Map of mean annual upward longwave radiation of Hawaiʻi.

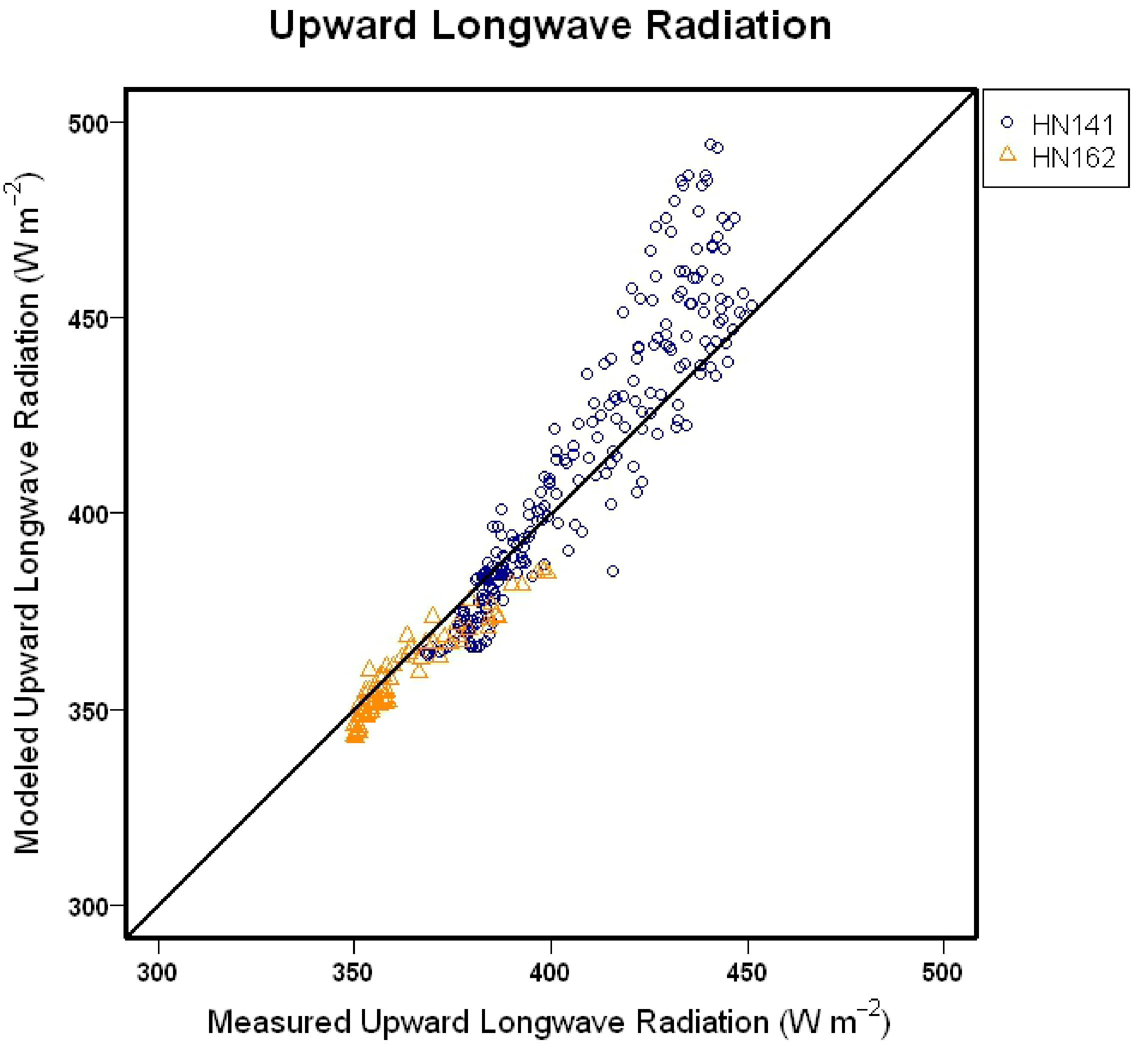

Figure 35. Scatterplot of estimated (mapped) versus measured mean hourly upward longwave radiation for stations not used in model development.

Table 10. Statistical results of estimated (mapped) versus measured upward radiation for stations not used in model development.

Sta. ID	N	b	a	r^2	MBE	MBE%	RMSE	RMSE%	Mod.	Meas.	N_{obs} (mo.)
All	315	1.29	-112	0.91	3	1	15	4	400	396	14
HN141	243	1.38	-149	0.87	6	1	16	4	412	406	11
HN162	72	0.82	62	0.90	-4	-2	6	2	358	363	3

See Table 1 for definitions of column headings.

Net Radiation

Net radiation was calculated as the difference between incoming and outgoing radiation (Eq. 3). Estimated mean annual net radiation of the Hawaiian Islands is shown in Figure 36. For validation purposes, modeled net radiation estimates are compared with net radiation measured at stations not used in model development (Figure 37 and Table 11).

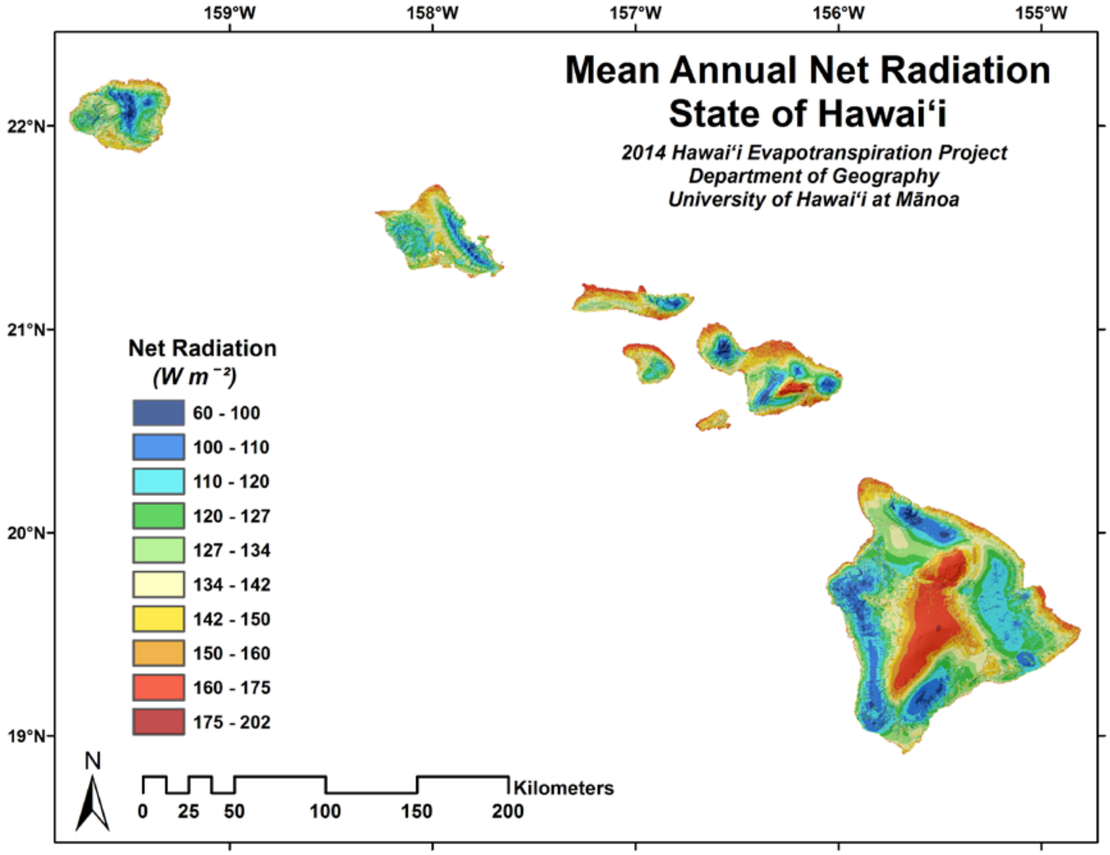

Figure 36. Map of mean annual net radiation of Hawaiʻi.

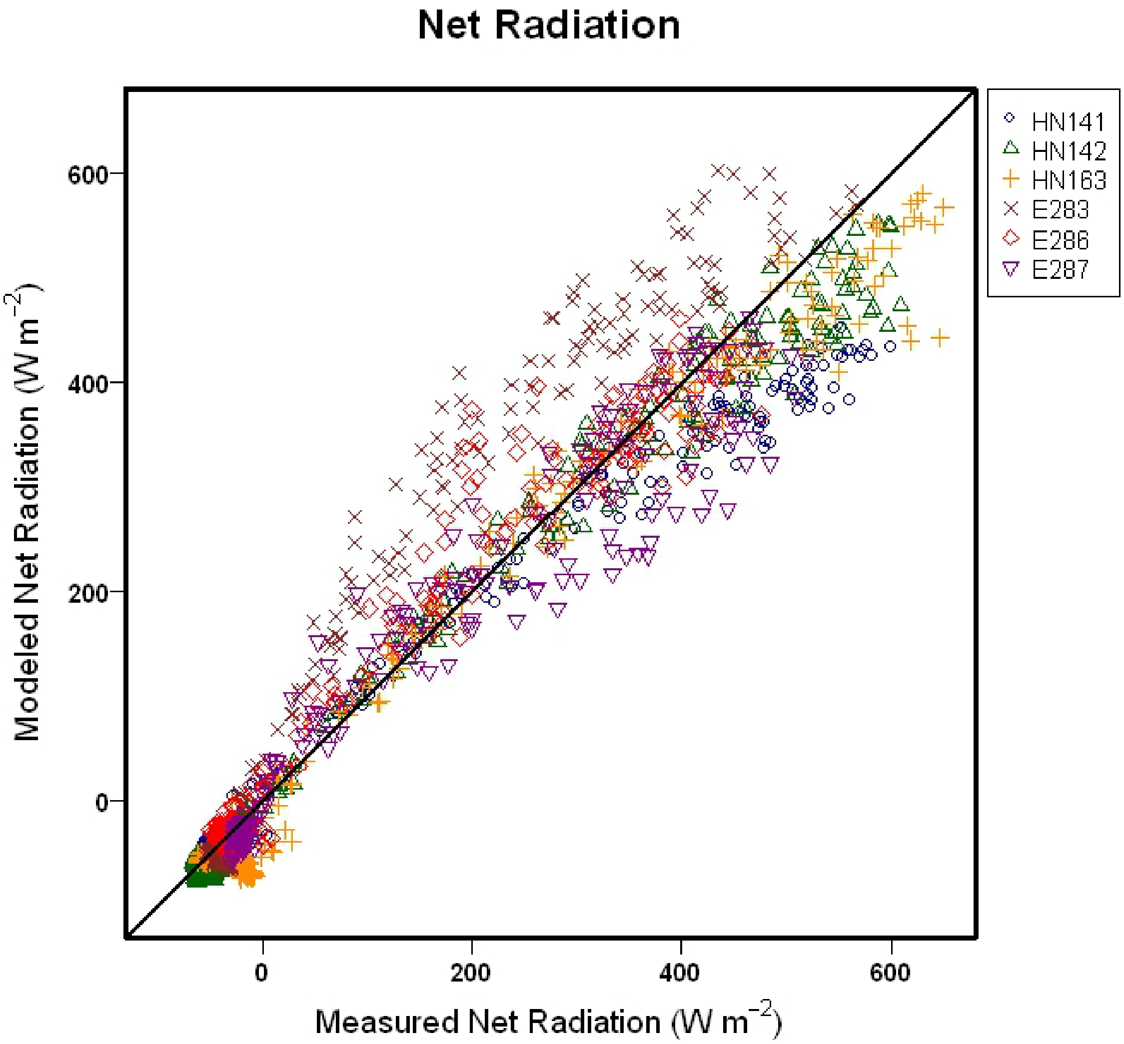

Figure 37. Scatterplot of estimated versus measured mean hourly net radiation.

Table 11. Statistical results of estimated (mapped) versus measured net radiation for stations not used in model development.

Sta. ID	N	b	a	r^2	MBE	MBE%	RMSE	RMSE%	Mod.	Meas.	N_{obs} (mo.)
All	1722	0.95	0	0.94	-5	-4	51	42	116	121	278
HN141	287	0.82	-2	0.98	-26	-20	54	41	106	132	121
HN142	287	0.93	-5	0.98	-15	-11	35	26	122	137	18
HN163	287	0.97	-25	0.98	-29	-19	45	29	126	155	43
E283	287	1.26	18	0.95	42	45	80	85	136	94	38
E286	287	0.99	10	0.96	9	9	35	35	109	100	36
E287	287	0.92	-5	0.95	-14	-12	43	39	97	111	22

See Table 1 for definitions of column headings.

Heat Storage Fluxes

Soil Heat Flux

Parameter values for the soil heat flux model (Eq. 17) are given in Tables 12-13. Estimated mean annual midday and midnight soil heat flux of the Hawaiian Islands are shown in Figure 38. For validation purposes, modeled soil heat flux estimates are compared with soil heat flux measured at stations not used in model development (Figure 39 and Table 14).

Table 12. Parameter values for estimating the diurnal amplitude of soil heat flux (Eq. 17).

Month	b_1	b_0	r^2
Jan	-0.5776	0.4723	0.902
Feb	-0.6034	0.4791	0.868
Mar	-0.5565	0.4296	0.829
Apr	-0.6427	0.4727	0.824
May	-0.6525	0.4975	0.911
Jun	-0.676	0.4939	0.876
Jul	-0.6565	0.4883	0.857
Aug	-0.5922	0.4451	0.958
Sep	-0.6866	0.484	0.924
Oct	-0.6351	0.4758	0.944
Nov	-0.6968	0.5208	0.931
Dec	-0.6374	0.5029	0.894

Table 13. Parameter values describing the shape of the diurnal cycle of soil heat flux (Eq. 17).

Month	i_0		σ	
	mean	s.d.	mean	s.d.
1	13.1	1.081	2.82	0.380
2	13.0	0.933	2.84	0.316
3	12.7	0.854	2.92	0.272
4	12.6	0.872	2.99	0.282
5	12.4	0.929	3.00	0.266
6	12.4	0.883	3.08	0.339
7	12.6	0.864	3.09	0.390
8	12.7	0.884	2.99	0.304
9	12.6	0.960	2.94	0.332
10	12.5	0.987	2.83	0.314
11	12.6	0.987	2.70	0.364
12	12.9	1.067	2.70	0.338

(a)

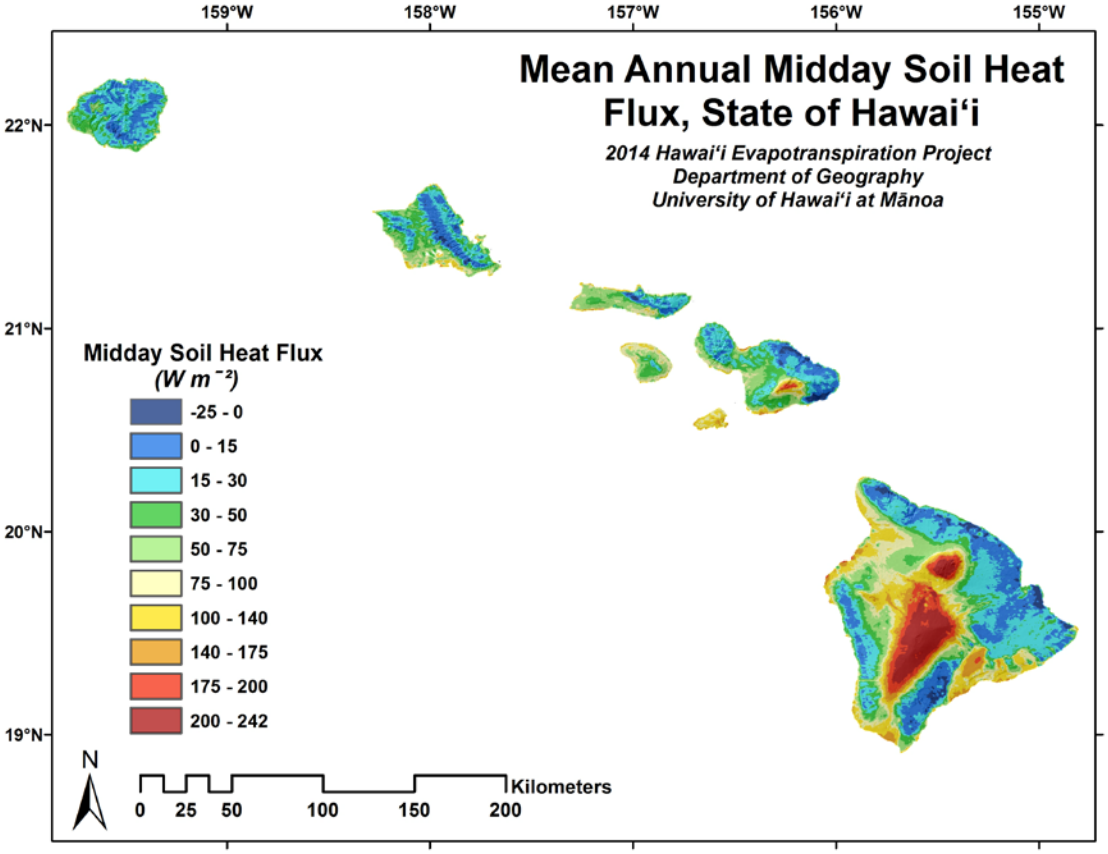
Mean Annual Midday Soil Heat Flux, State of Hawaiʻi
2014 Hawaiʻi Evapotranspiration Project
Department of Geography
University of Hawaiʻi at Mānoa
159°W
158°W
157°W
156°W
155°W
22°N
21°N
20°N
19°N
Midday Soil Heat Flux
(W m⁻²)
-25 - 0
0 - 15
15 - 30
30 - 50
50 - 75
75 - 100
100 - 140
140 - 175
175 - 200
200 - 242
N
0
25
50
100
150
200
Kilometers

(b)

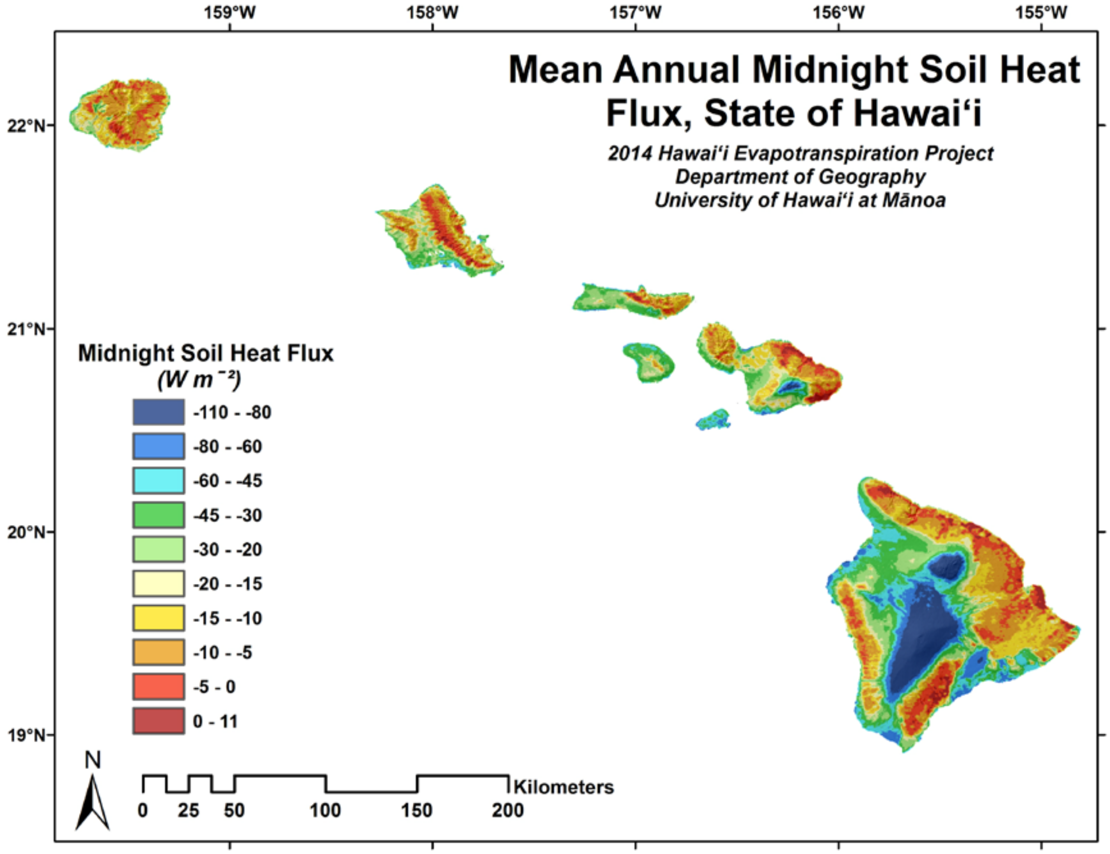

Figure 38. Mean annual midday (a) and midnight (b) soil heat flux of Hawaiʻi.

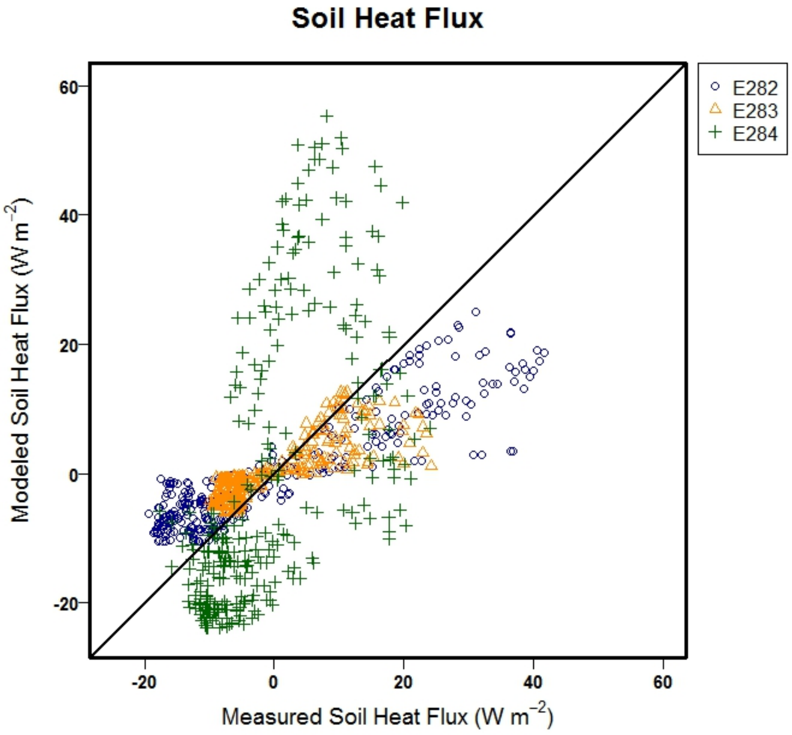

Figure 39. Scatterplot of estimated versus measured mean hourly soil heat flux.

Table 14. Statistical results of estimated (mapped) versus measured soil heat flux for stations not used in model development.

Sta. ID	N	b	a	R2	MBE	RMSE	MOD.	MEAS.	N_{obs} (mo.)
All	864	0.62	0.2	0.32	0.28	12.3	-0.0005	-0.28	67
E282	288	0.46	-0.1	0.82	-0.18	10.3	-0.0003	0.18	22
E283	288	0.45	0.2	0.69	0.44	5.3	-0.0002	-0.44	8
E284	288	1.31	0.8	0.34	0.58	17.8	-0.0009	-0.59	37

See Table 1 for definitions of column headings. Note that MBE% and RMSE% are not shown because mean soil heat flux (denominator MBE% and RMSE%) is near zero.

Biomass and Air Layer Energy Storage

The diurnal maximum and minimum biomass and air layer heat storage values (Q_{b_max}, Q_{b_min}, Q_{a_max}, and Q_{a_min}) were modeled in terms of maximum net radiation (R_{net_max}) and vegetation height (h) as:

$$\frac{Q_{b\_max}}{R_{net\_max}} = 0.00335 \cdot h, \quad r^2 = 0.59 \tag{70}$$

$$\frac{Q_{b\_min}}{R_{net\_max}} = -0.00209 \cdot h, \quad r^2 = 0.53 \tag{71}$$

$$\frac{Q_{a\_max}}{R_{net\_max}} = 0.00145 \cdot h, \quad r^2 = 0.58 \tag{72}$$

$$\frac{Q_{a\_min}}{R_{net\_max}} = -0.00101 \cdot h, \quad r^2 = 0.44 \tag{73}$$

A diurnal biomass energy storage template was estimated as the normalized hourly values (Q_b/R_{net_max} for daytime hours, and Q_b/R_{net_min} for nighttime hours) based on data observed at the Thurston (HVT) and Olaʻa (HVO) sites. The times of the diurnal maximum and minimum were varied by shifting the template. Maximum and minimum Q_b times, estimated as a function of vegetation height, are shown in Table 15, based on data from the Thurston (HVT) and Olaʻa (HVO) sites and results of prior heat storage studies (see Lit1-Lit7 in Appendix Table A3). In similar fashion, a diurnal air layer energy storage template was estimated as the normalized hourly values (Q_a/R_{net_max} for daytime hours, and Q_a/R_{net_min} for nighttime hours) based on data observed at the Thurston (HVT) and Olaʻa (HVO) sites. No significant variation in maximum and minimum times were observed among sites for Q_a.

Table 15. Time of maximum and minimum

Veg Height (m)	Time of Max	Time of Min
0.00 – 1.25	8:00	18:30
1.25 – 2.00	8:30	18:30
2.00 – 3.40	9:00	18:30
3.40 – 5.70	9:30	18:30
5.70 – 9.70	10:00	18:30
9.70 – 16.50	10:30	18:30
16.50 – 50.00	11:00	18:30

Estimated mean annual midday and midnight biomass energy storage flux of the Hawaiian Islands are shown in Figure 40. Estimated mean annual midday and midnight air layer energy storage flux of the Hawaiian Islands are shown in Figure 41. The estimated (mapped) and measured mean diurnal cycles of Q_b and Q_a for each month are shown for the two HAVO sites in Figure 42. Note that these two sites were used in developing the Q_b and Q_a models.

(a)

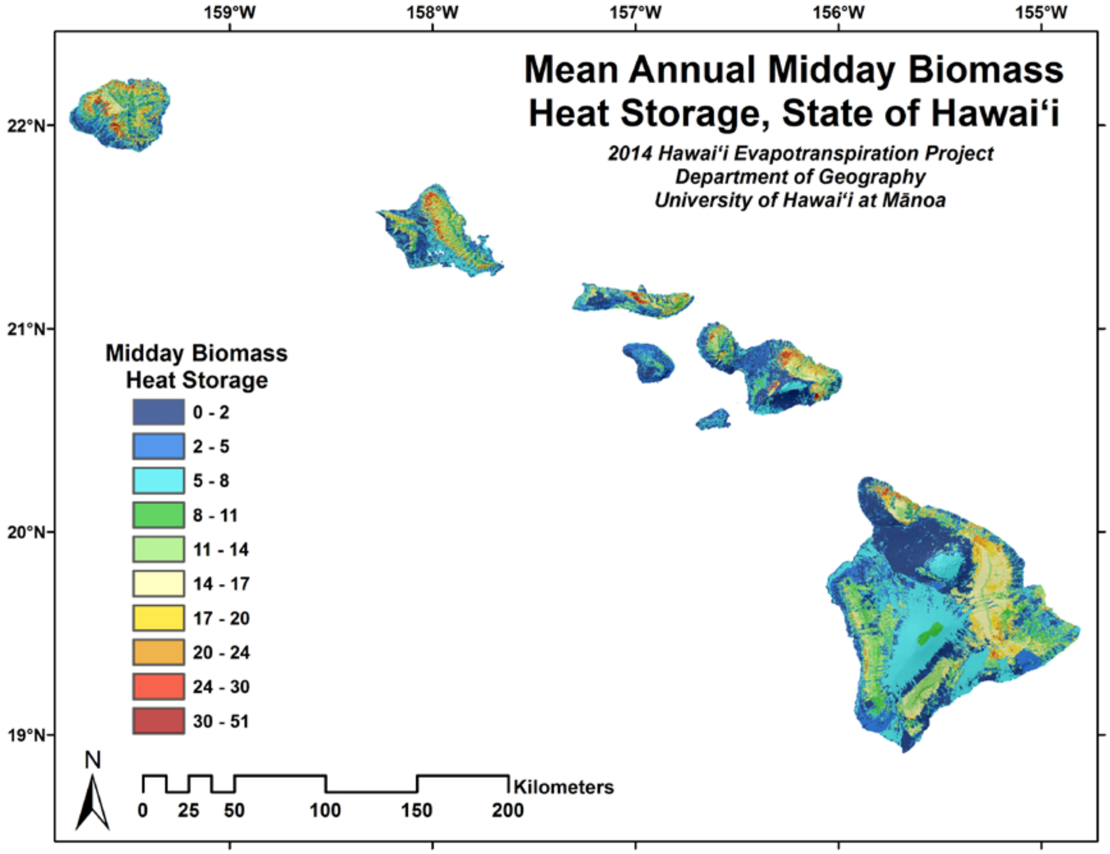

(b)

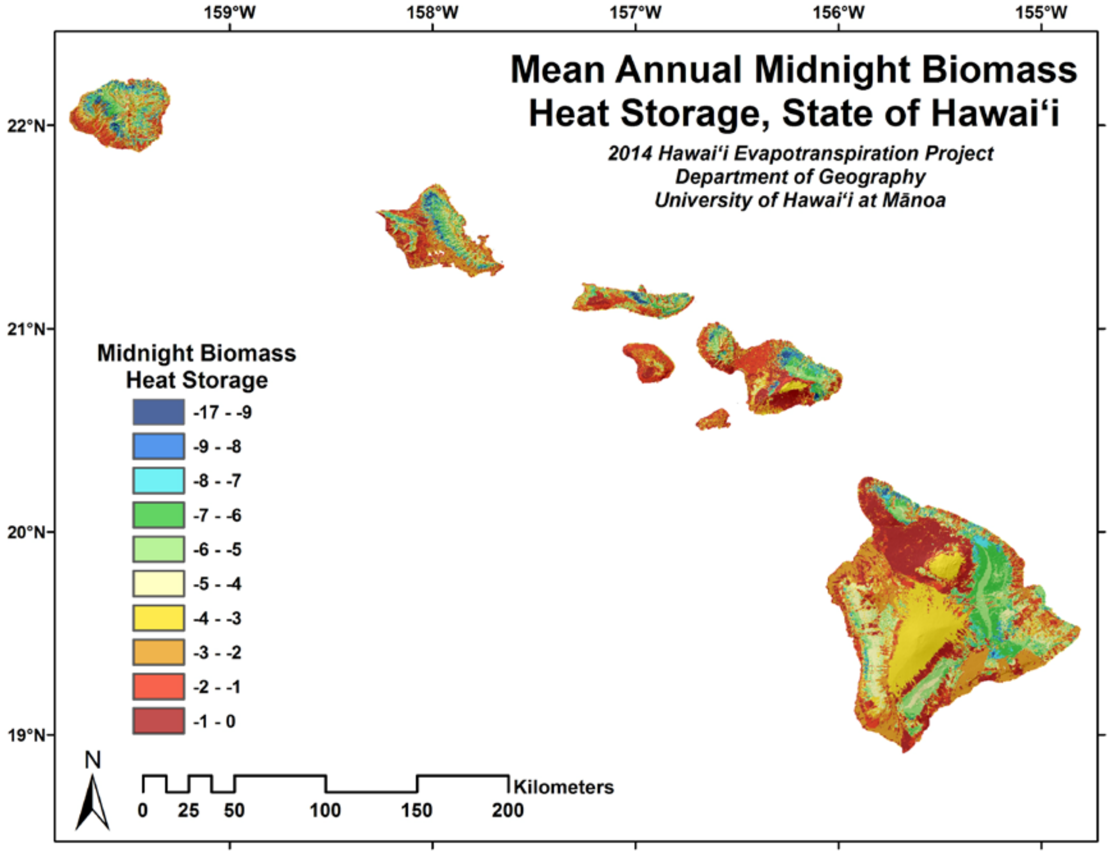

Figure 40. Mean annual midday (a) and midnight (b) biomass energy storage flux of Hawaiʻi.

(a)

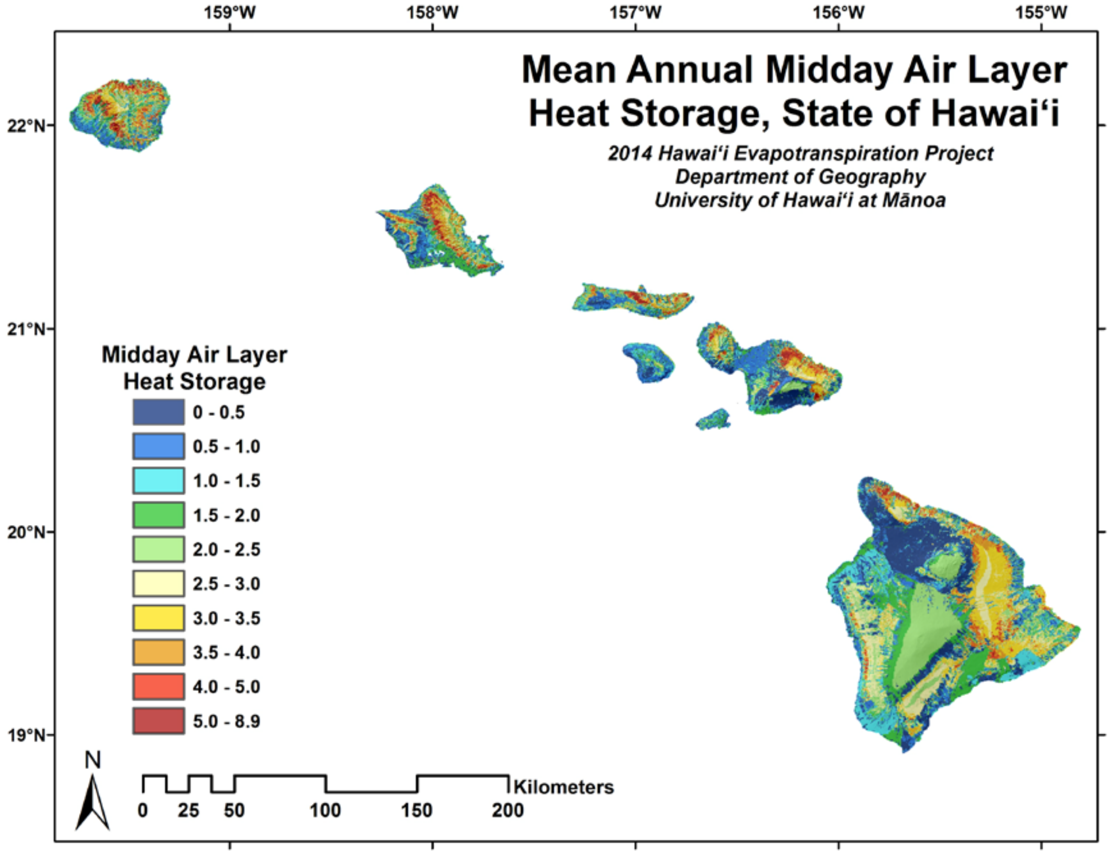
159°W
158°W
157°W
156°W
155°W
22°N
21°N
20°N
19°N
Mean Annual Midday Air Layer Heat Storage, State of Hawai'i
2014 Hawai'i Evapotranspiration Project
Department of Geography
University of Hawai'i at Mānoa
Midday Air Layer Heat Storage
0 - 0.5
0.5 - 1.0
1.0 - 1.5
1.5 - 2.0
2.0 - 2.5
2.5 - 3.0
3.0 - 3.5
3.5 - 4.0
4.0 - 5.0
5.0 - 8.9
N
0
25
50
100
150
200
Kilometers

(b)

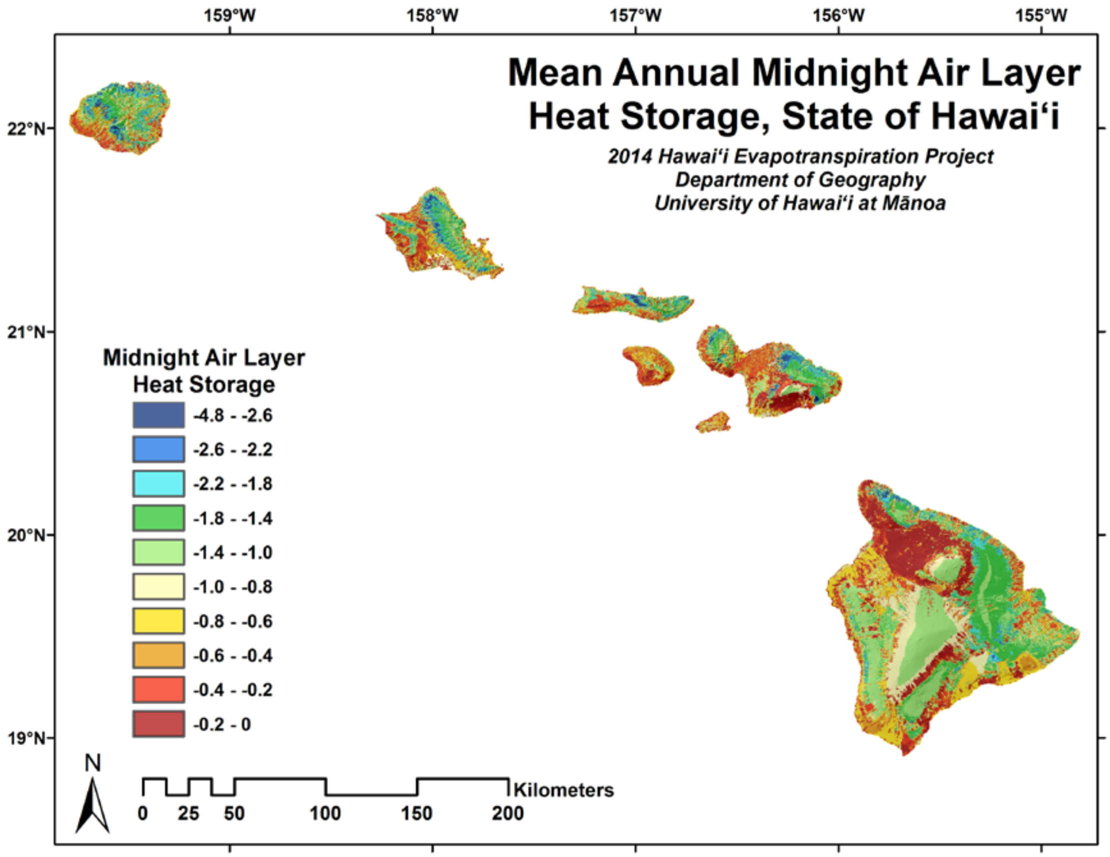

Figure 41. Mean annual midday (a) and midnight (b) air layer energy storage flux of Hawaiʻi.

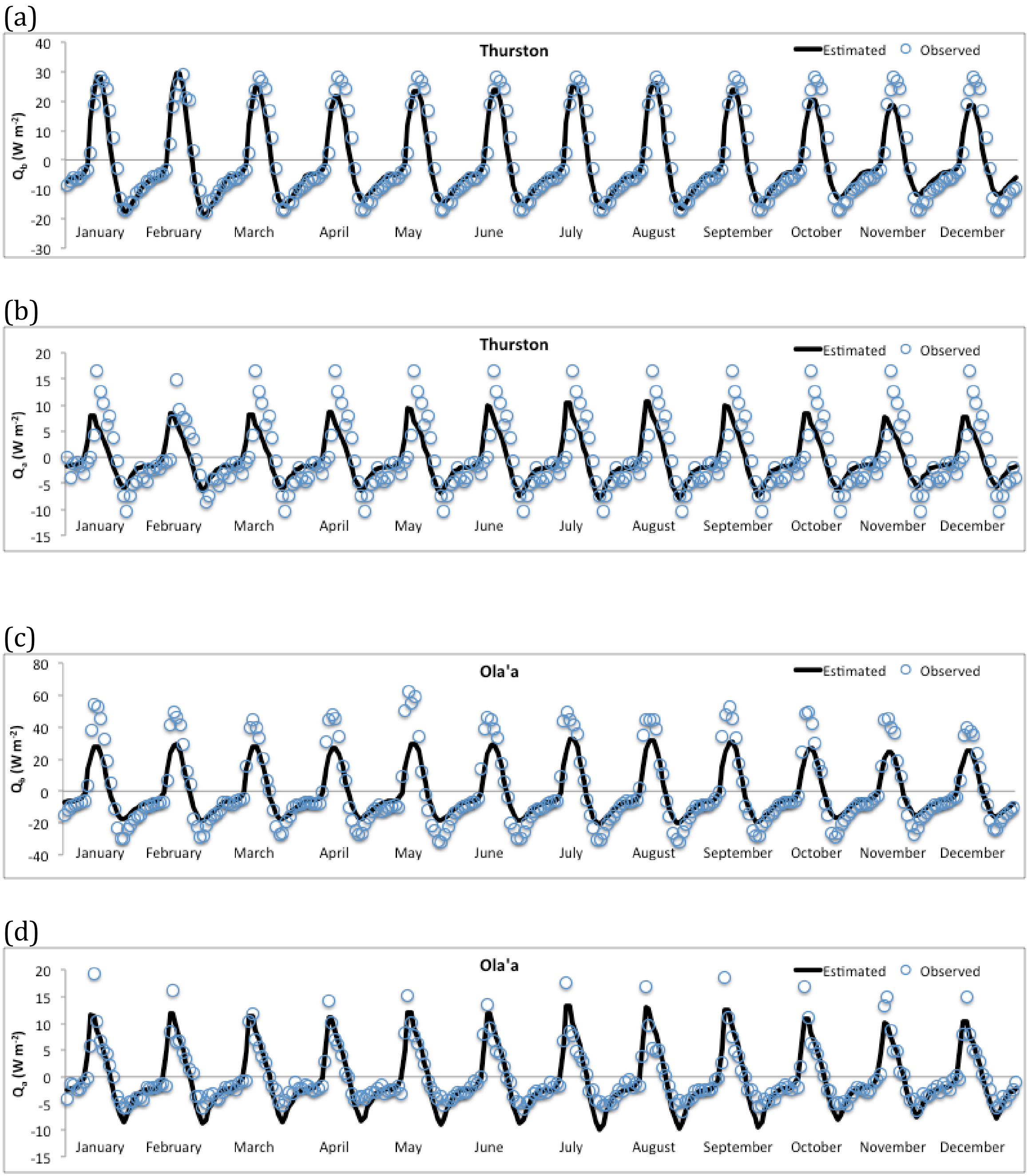

Figure 42. Estimated (mapped) and measured mean diurnal cycles of Q_b and Q_a for each month for the Thurston tower (HVT) site (a and b), and for the Olaʻa tower (HVO) site (c and d).

Other Meteorological Variables

Air Temperature

Model parameters for Eq. (18) to estimate monthly maximum, minimum, and mean air temperature as a function of elevation and mean rainfall were derived by least-squares regression using data from 131 stations representing a wide range of climates in Hawaiʻi (Appendix Table A3). Statistical results are shown in Table 16.

Appendix Table A3 lists the stations used to calibrate the diurnal temperature model, Eqs. (19-20). Corresponding coefficients of the equations derived at each station were averaged to generate the model (Table 17).

Estimated mean annual temperature of the Hawaiian Islands is shown in Figure 43. For validation purposes, modeled air temperature estimates are compared with air temperature measured at stations not used in model development (Figure 44 and Table 18).

Table 16. Model coefficients for monthly and annual maximum, minimum, and mean temperature models (Eq. 18).

Month	a_1	a_2	a_3	a_4	R^2
	------------- °C	-------------		°C mm^{-1}	
			T_{max} (°C)		
January	26.9	15.2	6.5	-0.0039	0.950
February	26.8	14.5	5.8	-0.0043	0.944
March	27.1	14.6	5.1	-0.0037	0.934
April	27.6	15.4	7.4	-0.0052	0.930
May	28.4	15.6	9.6	-0.0070	0.920
June	29.3	17.1	10.8	-0.0112	0.909
July	29.9	17.2	10.9	-0.0090	0.925
August	30.2	17.9	10.6	-0.0079	0.920
September	30.3	17.6	10.7	-0.0085	0.928
October	29.9	17.2	9.3	-0.0073	0.942
November	28.6	16.1	8.0	-0.0055	0.944
December	27.4	15.5	6.6	-0.0052	0.943
			T_{min} (°C)		
January	18.1	3.5	-1.3	-0.0013	0.918
February	18.0	3.3	-1.7	-0.0013	0.926
March	18.5	3.7	-2.4	-0.0015	0.936
April	19.2	4.4	-0.6	-0.0019	0.935
May	20.0	5.0	0.6	-0.0027	0.935
June	21.0	6.3	1.1	-0.0053	0.926
July	21.5	6.5	0.9	-0.0037	0.931
August	21.9	7.0	1.5	-0.0039	0.933
September	21.7	6.5	1.5	-0.0051	0.926
October	21.2	6.1	0.5	-0.0032	0.927
November	20.3	5.5	-0.1	-0.0019	0.930
December	19.0	4.2	-0.9	-0.0013	0.927
			T_{mean} (°C)		
January	22.0	8.9	2.6	-0.0008	0.906
February	22.0	8.7	2.1	-0.0015	0.919
March	22.4	8.9	1.4	-0.0017	0.920
April	23.1	9.7	3.4	-0.0027	0.917
May	23.8	10.0	5.2	-0.0031	0.911
June	24.7	11.4	6.1	-0.0057	0.903
July	25.3	11.5	6.0	-0.0046	0.917
August	25.7	12.1	6.1	-0.0043	0.915
September	25.6	11.7	6.1	-0.0042	0.909
October	25.2	11.4	4.9	-0.0035	0.918
November	24.1	10.5	4.0	-0.0026	0.929
December	22.8	9.5	2.9	-0.0020	0.921

Table 17. Model coefficients for diurnal cycle of air temperature (Eqs. 19-20).

Month	t_{Tmin} (hr)*	$t_{sunrise}$** (hr)*	t_{sunset}** (hr)*	l (hr)	a (hr)	b (hr)	c -	d -
Jan	7.00	7.17	18.18	11.02	1.75	-0.167	4.825	1.011
Feb	7.00	7.02	18.48	11.47	2.00	-0.017	6.050	1.036
Mar	6.75	6.63	18.68	12.05	2.00	0.117	3.625	0.972
Apr	6.25	6.18	18.85	12.67	2.00	0.067	3.550	0.986
May	6.00	5.88	19.05	13.17	1.75	0.117	3.500	0.992
Jun	6.00	5.82	19.23	13.42	2.00	0.183	4.125	1.004
Jul	6.25	5.97	19.25	13.28	2.25	0.283	4.625	1.004
Aug	5.50	6.17	18.98	12.82	2.25	-0.667	4.925	0.992
Sep	6.25	6.30	18.55	12.25	1.50	-0.050	3.775	0.965
Oct	5.25	6.45	18.10	11.65	1.25	-1.200	3.725	0.997
Nov	5.50	6.70	17.83	11.13	1.00	-1.200	5.375	0.981
Dec	6.25	7.02	17.88	10.87	1.75	-0.767	4.400	0.996

*Time of day given in Hawai‘i Standard Time. **Sunrise and sunset times are for Kahului, Hawai‘i (20° 53’ N, 156° 28’ W), for the year 2005 (U.S. Naval Observatory N.D.; http://aa.usno.navy.mil/data/docs/rs_oneyear.php).

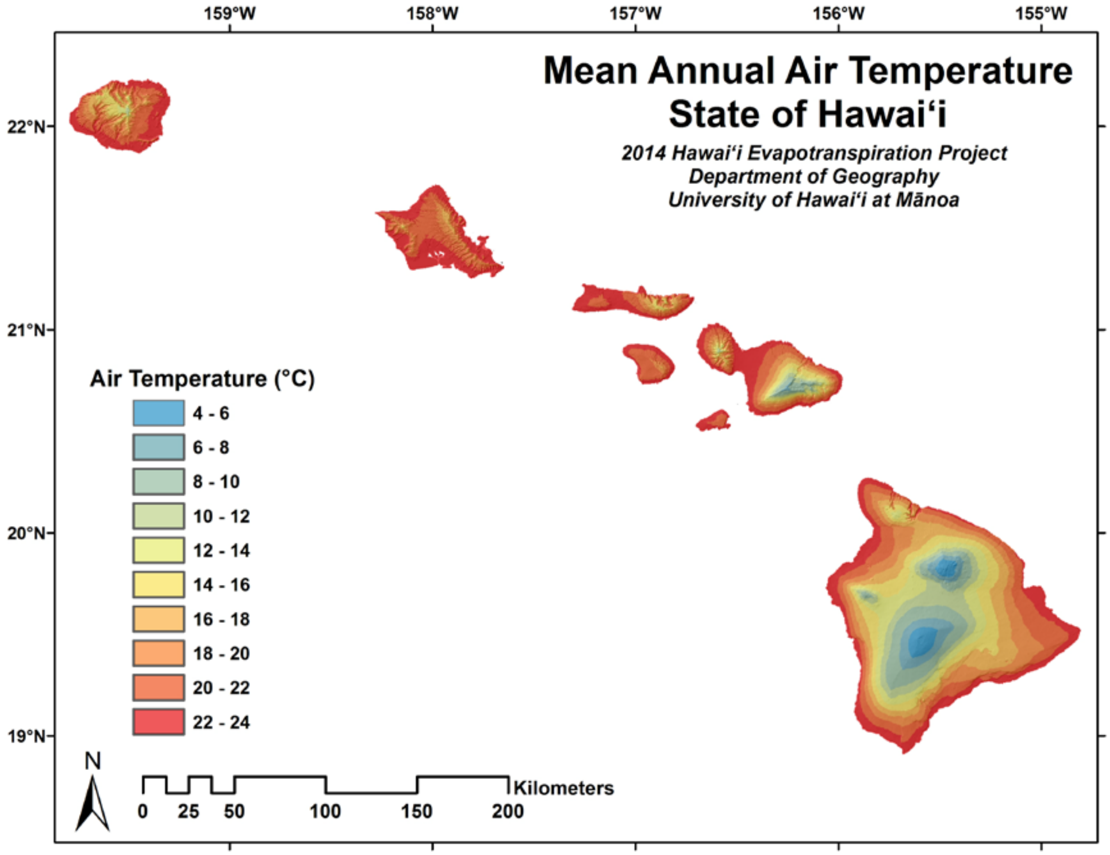

Figure 43. Map of mean annual air temperature of Hawai‘i.

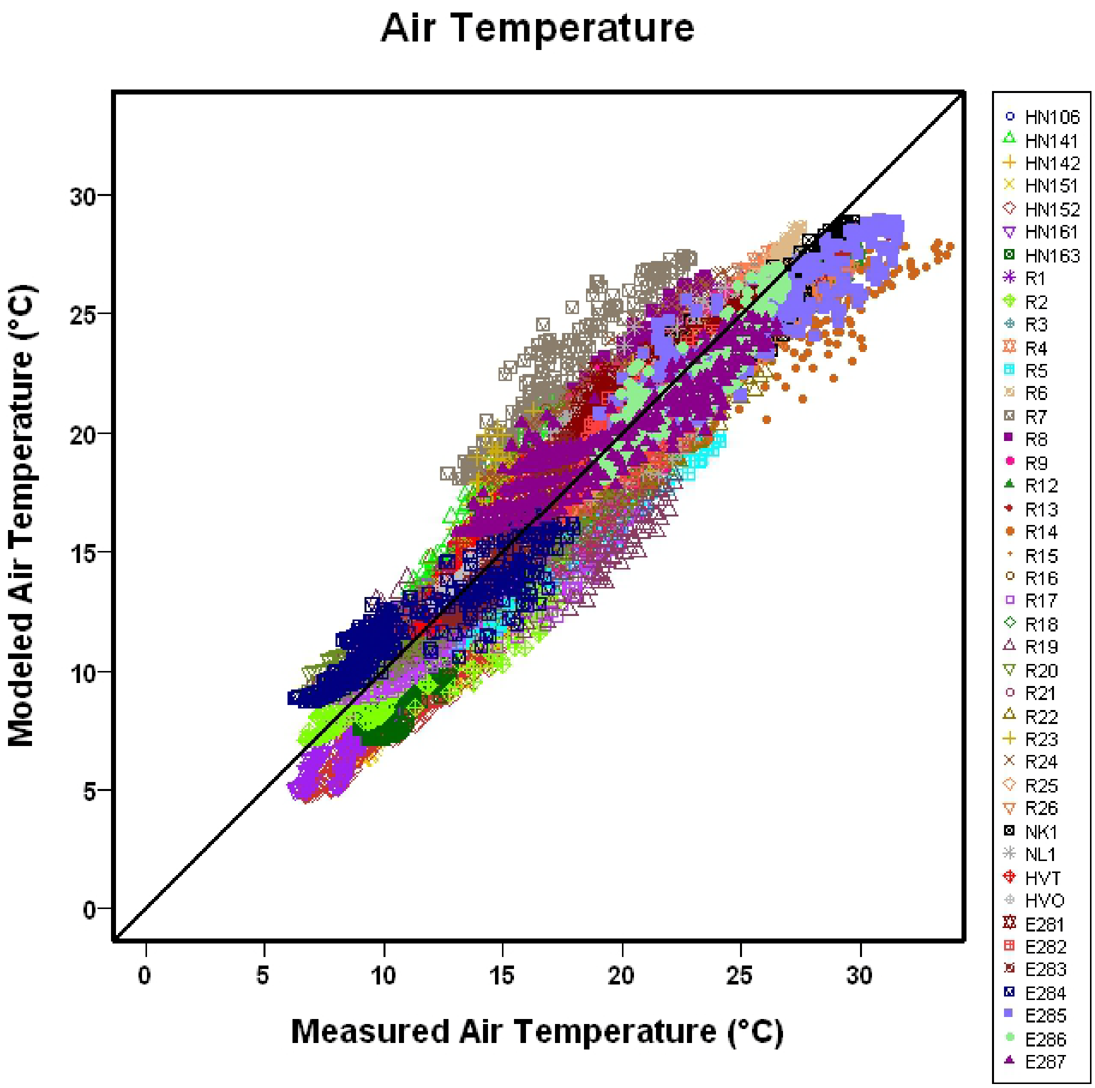

Figure 44. Scatterplot of estimated (mapped) versus observed mean hourly air temperature for each month at validation stations.

Table 18. Statistical results of estimated (mapped) versus measured air temperature for stations not used in model development.

Sta. ID	N	b	a	r^2	MBE	MBE%	RMSE	RMSE%	Mod.	Meas.	N_{obs} (mo.)
All	12096	0.95	0.6	0.89	-0.1	0	0.5	3	17.9	18.2	3788
R1	288	0.90	2.1	0.68	0.0	0	1.4	7	21.8	21.8	121
R2	288	0.60	3.5	0.82	-1.3	-11	2.1	17	10.7	12.0	119
R3	288	1.18	-4.3	0.92	-0.3	-1	0.8	4	22.8	23.1	131
R4	288	1.40	-9.8	0.93	-0.7	-3	1.2	5	22.5	23.1	112
R5	288	0.78	1.4	0.93	-2.4	-14	2.5	15	14.8	17.2	121
R6	288	1.34	-8.9	0.89	-0.6	-3	1.2	5	23.6	24.2	107
R7	288	0.84	7.2	0.69	4.4	24	4.6	26	22.2	17.9	102
R8	288	1.12	-0.9	0.68	1.4	7	2.0	10	21.4	19.9	96
R9	288	1.03	-1.0	0.74	-0.3	-1	1.3	6	21.1	21.3	103
R12	288	0.82	3.1	0.96	-1.2	-5	1.4	6	22.5	23.7	79
R13	288	0.81	3.6	0.94	-1.0	-4	1.3	5	23.6	24.6	104
R14	288	0.83	2.7	0.95	-0.7	-4	1.0	5	18.6	19.3	89
R15	288	0.59	8.2	0.80	-2.0	-8	2.7	11	22.9	24.9	83
R16	288	0.79	4.5	0.78	0.5	2	1.4	7	20.0	19.6	82
R17	288	0.65	3.5	0.82	-1.5	-11	2.2	15	12.9	14.4	91
R18	288	0.82	2.9	0.91	-0.5	-3	1.0	6	18.2	18.7	128
R19	288	0.51	6.0	0.84	-1.2	-8	2.6	18	13.5	14.6	106
R20	288	0.63	4.6	0.91	-0.2	-1	1.6	12	12.9	13.1	124
R21	288	0.64	5.3	0.87	-0.5	-3	1.6	10	15.7	16.1	132
R22	288	0.64	6.2	0.83	-0.6	-3	1.7	9	18.6	19.2	68
R23	288	0.64	7.6	0.75	1.0	5	2.0	11	19.4	18.4	95
R24	288	0.75	6.7	0.83	1.9	10	2.3	11	21.6	19.7	125
R25	288	0.88	1.9	0.91	-0.5	-3	0.9	4	20.4	20.9	96
R26	288	0.78	3.9	0.95	-1.3	-6	1.6	7	22.0	23.3	98
HN106	288	1.05	-1.0	0.92	-0.4	-3	0.8	6	13.2	13.5	163
HN141	288	1.39	-3.0	0.94	2.4	17	2.6	18	16.4	14.0	130
HN142	288	0.91	-0.2	0.75	-1.3	-11	1.7	14	10.7	11.9	21
HN151	288	0.95	-1.5	0.92	-2.1	-18	2.2	18	10.0	12.2	127
HN152	288	0.81	-0.5	0.94	-2.6	-23	2.7	24	8.4	11.0	131
HN161	288	1.22	-3.2	0.88	-1.1	-11	1.4	14	8.5	9.6	105
HN163	288	1.24	-4.1	0.81	-1.4	-12	1.6	14	10.1	11.5	47
NK1	288	0.88	2.3	0.91	-0.5	-2	1.0	4	23.7	24.3	20
NL1	288	0.68	7.2	0.78	0.6	3	1.7	8	21.3	20.7	29
HVT	288	1.16	-1.6	0.90	0.8	5	1.1	7	15.3	14.5	58
HVO	288	0.97	0.9	0.91	0.4	2	0.7	4	15.9	15.5	51
E281	288	0.70	7.1	0.86	0.8	4	1.3	6	21.9	21.1	31
E282	288	0.89	2.1	0.82	-0.1	-1	0.9	4	19.6	19.7	33
E283	288	1.31	-4.9	0.87	-0.1	-1	0.9	6	15.3	15.4	44
E284	288	0.58	5.3	0.83	0.5	4	1.7	14	12.2	11.7	39
E285	288	0.68	6.9	0.83	-1.2	-5	1.9	8	23.8	25.0	30
E286	288	0.93	1.0	0.88	-0.5	-2	1.0	4	22	22.5	36
E287	288	0.62	7.7	0.85	0.2	1	1.7	9	19.8	19.6	22

See Table 1 for definitions of column headings.

Relative Humidity

Mean monthly minimum and maximum relative humidity were estimated as a function of elevation using a third-order polynomial (Eq. 21). Model coefficients (Table 19) were derived using data from 26 stations distributed throughout the islands (Appendix Table A3). The model was implemented to map mean monthly minimum and maximum relative humidity by using DEM-derived elevation values as input to the model.

Table 19. Model coefficients for monthly relative humidity model.

Month	a_0	a_1	a_2	a_3	r^2
RH_{max}					
Jan	83.75	3.38E-02	-2.17E-05	2.68E-09	0.888
Feb	82.80	3.41E-02	-2.05E-05	2.28E-09	0.828
Mar	82.37	2.81E-02	-1.36E-05	1.12E-09	0.822
Apr	81.91	2.87E-02	-1.34E-05	1.07E-09	0.822
May	80.56	3.69E-02	-2.02E-05	2.17E-09	0.841
Jun	79.39	3.90E-02	-2.06E-05	2.23E-09	0.800
Jul	80.01	3.54E-02	-1.85E-05	2.05E-09	0.785
Aug	80.86	2.72E-02	-1.20E-05	9.38E-10	0.828
Sep	80.67	2.28E-02	-7.31E-06	-1.20E-10	0.871
Oct	81.67	2.26E-02	-7.67E-06	-9.87E-12	0.827
Nov	82.89	2.72E-02	-1.43E-05	1.45E-09	0.786
Dec	82.58	2.88E-02	-1.55E-05	1.57E-09	0.773
RH_{min}					
Jan	58.20	1.84E-02	-2.13E-05	3.47E-09	0.900
Feb	56.52	2.34E-02	-2.36E-05	3.70E-09	0.866
Mar	55.85	3.63E-02	-2.95E-05	4.41E-09	0.821
Apr	55.32	4.66E-02	-3.40E-05	4.90E-09	0.739
May	56.13	4.30E-02	-3.42E-05	5.08E-09	0.841
Jun	55.41	4.80E-02	-3.59E-05	5.19E-09	0.759
Jul	55.81	3.87E-02	-2.93E-05	4.25E-09	0.673
Aug	55.74	3.79E-02	-2.76E-05	3.81E-09	0.710
Sep	55.46	4.20E-02	-2.88E-05	3.80E-09	0.736
Oct	57.47	3.70E-02	-2.73E-05	3.75E-09	0.683
Nov	59.51	2.28E-02	-2.11E-05	3.18E-09	0.708
Dec	59.07	2.20E-02	-2.27E-05	3.62E-09	0.743

Stations with hourly *RH* data (see Appendix Table A3) were used to derive parameters for the diurnal *RH* model, Eq. (23). Model coefficients were regionalized by elevation (Table 20).

Table 20. Parameter values for the estimation of the mean diurnal cycle of relative humidity, regionalized by elevation.

$a_0 = 0.5$	
$a_1 = -0.5$	for $0 < z \leq 500$
$a_1 = 0.0006333 * z - 0.81666$	for $500 < z \leq 2000$
$a_1 = 0.45$	for $z > 2000$
$b_1 = 0.00075 * z - 0.25$	for $0 < z \leq 1000$
$b_1 = 0.5$	for $1000 < z \leq 1500$
$b_1 = -0.0003 * z + 0.95$	for $z > 1500$
$w = 0.00011954 * z + 2.11224746$	

Note: z = elevation (m).

Estimated mean annual relative humidity of the Hawaiian Islands is shown in Figure 45. For validation purposes, modeled relative humidity estimates are compared with relative humidity measured at stations not used in model development (Figure 46 and Table 21).

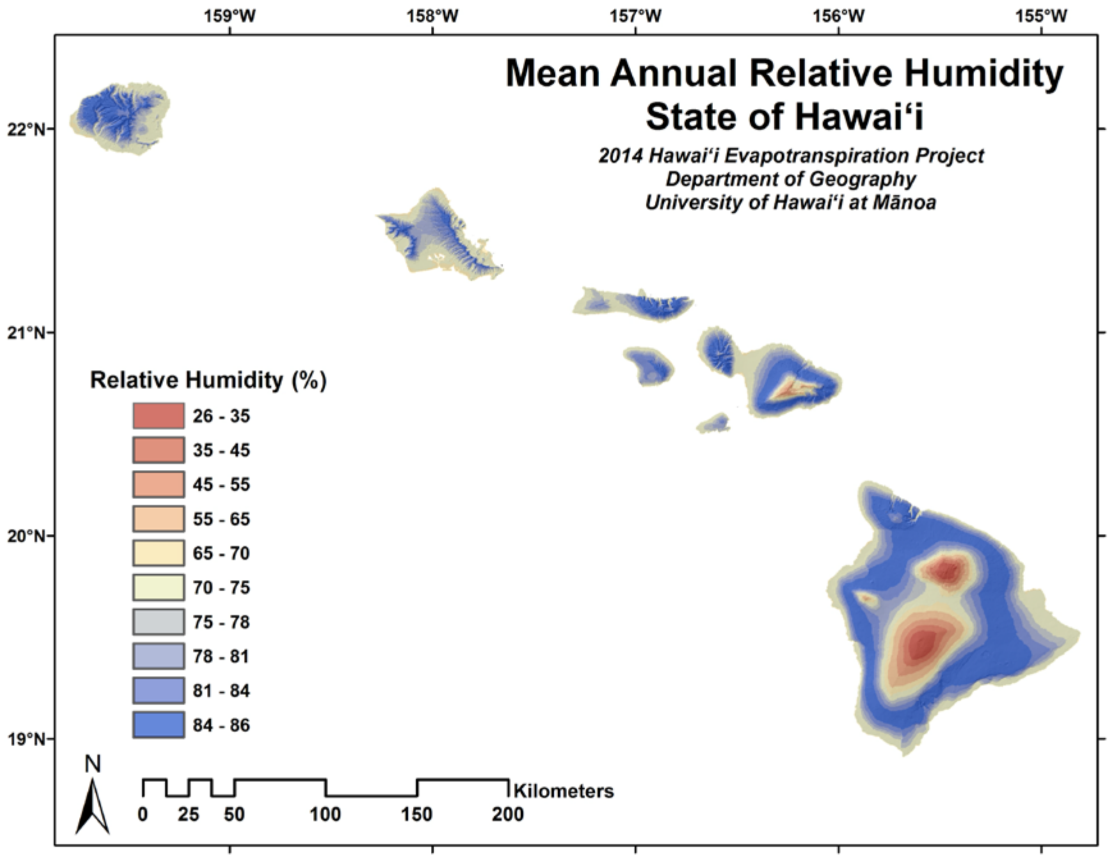

Figure 45. Map of mean annual relative humidity of Hawaiʻi.

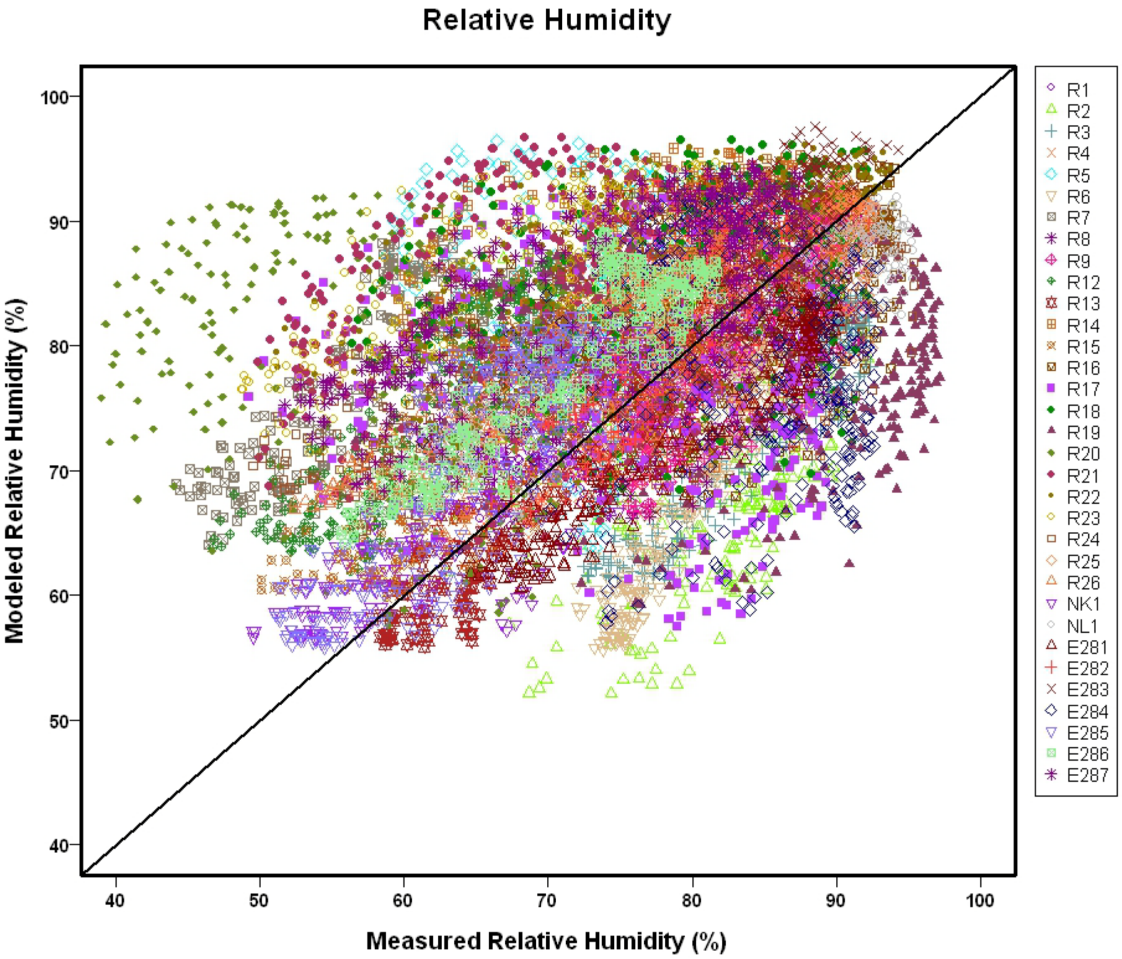

Figure 46. Scatterplot of estimated (mapped) versus observed mean hourly relative humidity for each month at validation stations.

Table 21. Statistical results of estimated (mapped) versus measured relative humidity for stations not used in model development.

Sta. ID	N	b	a	r^2	MBE	MBE%	RMSE	RMSE%	Mod.	Meas.	N_{obs} (mo.)
All	3771	0.36	52	0.21	8	11	19	25	79	76	3027
R1	288	0.78	19	0.54	2	2	5	7	79	77	121
R2	288	0.12	63	0.01	-7	-9	13	17	72	80	119
R3	288	1.18	-27	0.87	-11	-13	12	14	74	85	126
R4	288	0.99	4	0.62	3	4	5	7	77	74	118
R5	288	0.09	77	0.00	11	15	14	20	84	73	118
R6	288	1.97	-89	0.90	-11	-13	12	14	70	80	113
R7	288	0.68	38	0.50	18	31	19	32	78	60	105
R8	288	0.58	35	0.48	2	2	7	8	81	79	96
R9	288	1.24	-24	0.80	-3	-3	5	5	82	85	112
R12	288	0.88	20	0.71	13	20	13	21	75	63	70
R13	288	1.08	-7	0.87	-1	-1	3	5	70	71	104
R14	288	0.23	68	0.08	8	11	12	16	86	78	89
R15	288	0.84	17	0.71	6	8	7	11	73	67	82
R16	288	0.43	48	0.24	1	1	8	9	84	83	82
R17	288	-0.12	87	0.02	1	2	15	19	78	76	91
R18	288	0.27	65	0.13	7	9	12	15	86	79	287
R19	288	0.03	77	0.00	-5	-6	14	17	80	84	106
R20	288	-0.30	96	0.11	19	33	24	41	78	59	124
R21	288	0.32	63	0.13	17	25	19	29	85	67	106
R22	288	0.36	58	0.37	8	10	12	15	86	78	68
R23	288	0.50	51	0.49	18	26	19	28	85	68	95
R24	288	0.45	46	0.62	6	8	10	14	79	74	117
R25	288	0.63	31	0.64	0	0	6	7	83	83	96
R26	288	0.68	29	0.74	6	8	8	11	78	72	98
NK1	288	0.73	20	0.78	1	1	5	7	70	69	20
NL1	288	0.57	35	0.86	0	0	6	7	81	81	29
HVT	288	0.18	68	0.01	-8	-9	12	13	85	93	58
HVO	288	1.21	-25	0.56	-6	-7	8	9	86	93	46
E281	288	0.89	3	0.88	-6	-8	7	9	74	80	31
E282	288	1.07	-3	0.60	3	4	5	7	83	80	33
E283	288	1.27	-22	0.54	1	1	5	6	86	85	40
E284	288	-0.01	79	0.00	-6	-7	12	15	78	84	39
E285	288	1.13	-2	0.68	6	9	8	12	70	64	30
E286	288	0.87	16	0.82	7	10	8	11	78	71	36
E287	288	0.46	51	0.55	12	16	14	19	85	73	22

See Table 1 for definitions of column headings.

Vapor Pressure Deficit

Vapor pressure deficit was computed from the mapped values of air temperature and relative humidity. Estimated mean annual vapor pressure deficit of the Hawaiian Islands is shown in Figure 47.

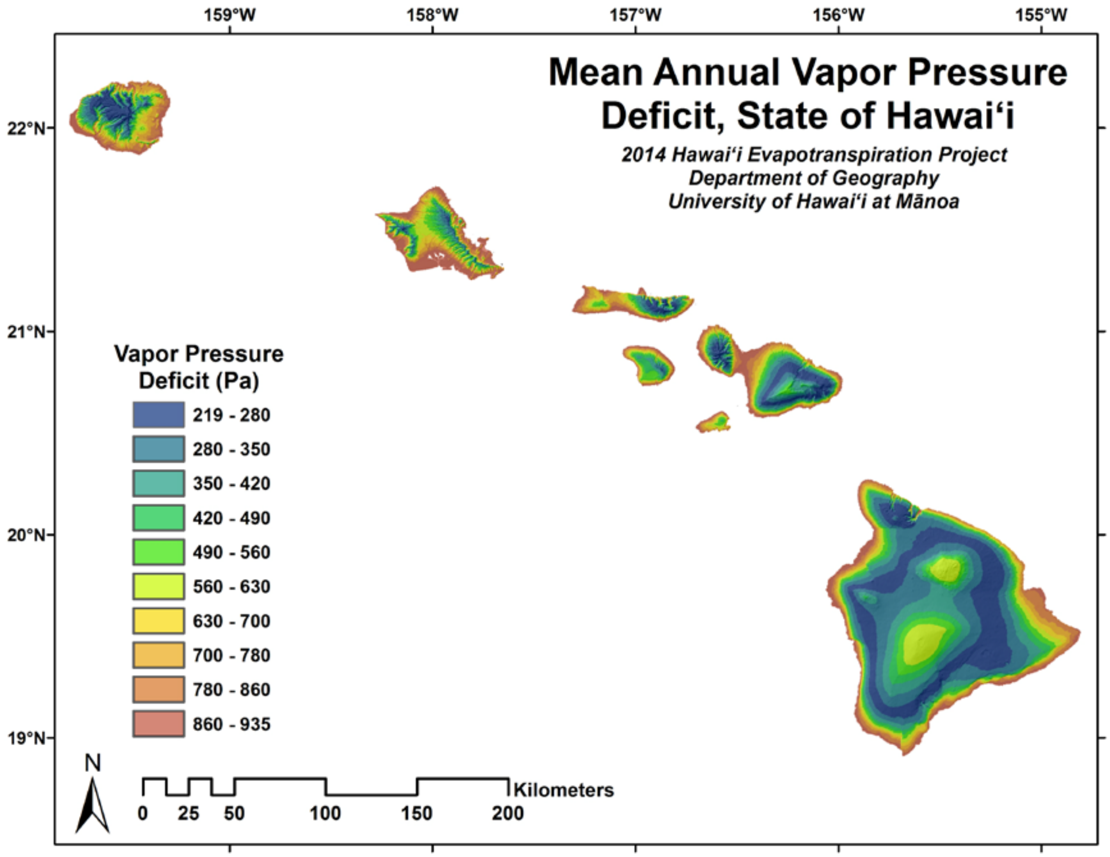

Figure 47. Map of mean annual vapor pressure deficit of Hawaiʻi.

Wind Speed

Hourly wind speed data for the stations in Hawaiʻi (Appendix Table A3) were used to derive parameter values for the diurnal wind speed model. Parameter values are shown in Table 22. Estimated mean annual wind speed of the Hawaiian Islands is shown in Figure 48. For validation purposes, modeled wind speed estimates are compared with wind speed measured at stations not used in model development (Figure 49 and Table 23).

Table 22. Parameter values for the diurnal wind speed model, Eq. (29).

	Sigmoid			Linear		Exponential		
Hour	a_i	b_i	z_{0_i}	c_i	d_i	g_i	h_i	k_i
1:00	1.27	1628.65	-262.46					
2:00	1.18	1252.55	-238.75					
3:00	1.14	1143.84	-306.09					
4:00	1.12	1016.87	-304.71					
5:00	1.11	992.57	-330.92					
6:00	1.11	954.90	-354.72					
7:00	1.13	1127.84	-447.31					
8:00				0.73	1.00E-04			
9:00				0.89	2.92E-05			
10:00						0.88	0.30	5.00E-04
11:00						0.21	1.15	2.00E-04
12:00						-1.66	3.14	7.34E-05
13:00						-4.41	5.98	4.49E-05
14:00						-20.82	22.41	1.22E-05
15:00						-6.77	8.37	3.48E-05
16:00						-3.88	5.40	4.87E-05
17:00						0.10	1.31	2.00E-04
18:00						0.85	0.37	7.00E-04
19:00				0.88	2.92E-05			
20:00				0.74	1.00E-04			
21:00	2.26	3864.94	2996.13					
22:00	1.70	2943.10	886.98					
23:00	1.42	2038.41	58.90					
24:00	1.38	2029.14	-163.32					

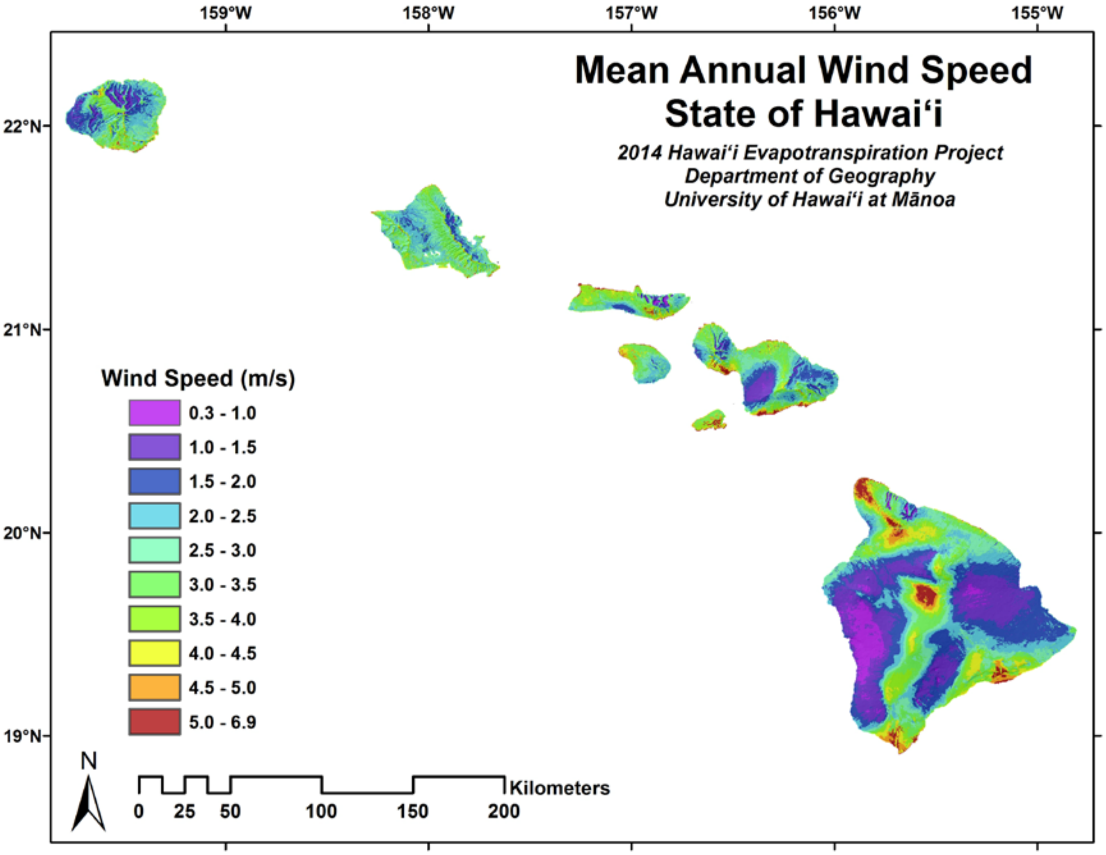

Figure 48. Map of mean annual wind speed for Hawaiʻi (derived from data of AWS Truewind 2004).

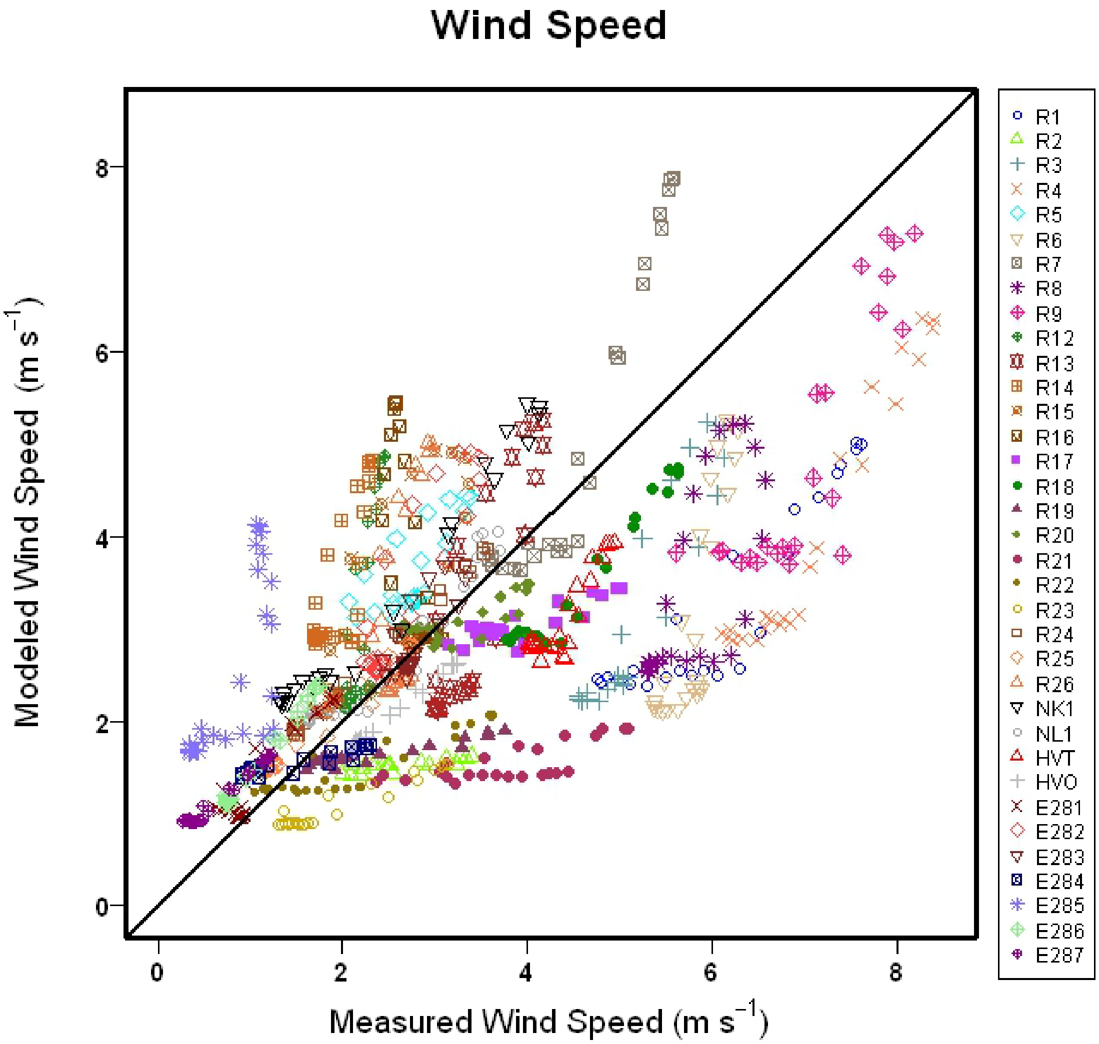

Figure 49. Scatterplot of estimated (mapped) versus observed mean hourly wind speed at validation stations.

Table 23. Statistical results of estimated versus measured wind speed for all available observing stations not used in model development.

Sta. ID	N	b	a	r^2	MBE	MBE%	RMSE	RMSE%	Mod.	Meas.	N_{obs} (mo.)
All	840	0.46	1.3	0.40	-0.1	-3	0.5	15	2.8	3.2	3006
R1	24	0.96	-2.6	0.84	-2.8	-46	2.8	47	3.3	6.1	121
R2	24	0.11	1.2	0.62	-1.1	-41	1.1	44	1.5	2.6	119
R3	24	2.00	-7.2	0.86	-2.0	-37	2.1	40	3.3	5.2	125
R4	24	1.70	-8.0	0.94	-3.0	-42	3.1	43	4.1	7.1	115
R5	24	0.96	1.0	0.54	0.8	31	0.9	33	3.6	2.7	121
R6	24	3.70	-18.3	0.73	-2.6	-44	2.7	47	3.2	5.8	107
R7	24	2.27	-5	0.89	0.6	12	1.2	25	5.1	4.6	100
R8	24	1.62	-6	0.47	-2.4	-40	2.5	43	3.5	5.8	96
R9	24	1.69	-7.0	0.72	-2.1	-30	2.3	33	4.9	7.0	100
R12	24	5.90	-9.9	0.66	0.9	41	1.3	59	3.1	2.2	76
R13	24	2.52	-5.4	0.79	-0.2	-6	0.9	25	3.3	3.4	102
R14	24	2.37	-1.2	0.55	1.5	78	1.6	83	3.5	2.0	89
R15	24	1.61	-0.6	0.8	0.8	34	1.0	43	3.1	2.3	82
R16	24	-3.85	14.2	0.47	1.0	36	1.5	55	3.7	2.7	73
R17	24	0.31	1.8	0.73	-0.9	-22	1.0	24	3.0	3.9	91
R18	24	1.06	-1.3	0.93	-1.1	-23	1.1	24	3.5	4.5	106
R19	24	0.17	1.2	0.91	-0.8	-32	1.0	41	1.6	2.4	106
R20	24	0.31	2.1	0.54	-0.1	-5	0.4	12	3.1	3.2	126
R21	24	0.19	0.8	0.53	-2.2	-59	2.3	62	1.5	3.8	132
R22	24	0.33	0.8	0.82	-0.6	-29	0.9	40	1.5	2.1	68
R23	24	0.38	0.3	0.92	-0.9	-45	1.0	49	1.1	2.0	95
R24	24	0.95	0.5	1.00	0.4	17	0.4	18	2.5	2.2	120
R25	24	0.82	0.5	0.97	0.2	11	0.2	14	1.9	1.7	95
R26	24	3.92	-7.0	0.44	0.6	24	1.1	43	3.2	2.6	99
NK1	24	1.15	0.5	0.97	0.9	37	0.9	38	3.4	2.5	20
NL1	24	0.98	0.3	0.93	0.2	9	0.3	12	2.7	2.5	29
HVT	24	1.33	-2.7	0.79	-1.3	-29	1.3	30	3.1	4.4	52
HVT	24	1.03	-2.5	0.82	-2.4	-54	2.4	54	2.0	4.4	48
E281	24	1.10	0.2	0.89	0.3	27	0.3	31	1.4	1.1	31
E282	24	1.93	-1.8	0.84	0.7	25	0.9	33	3.3	2.7	33
E283	24	1.41	-1.1	0.70	0.1	4	0.3	10	2.9	2.8	37
E284	24	0.19	1.3	0.79	0.1	10	0.4	30	1.5	1.4	39
E285	24	1.87	1.0	0.48	1.7	204	1.9	223	2.5	0.8	30
E286	24	1.25	0.2	1.00	0.5	44	0.5	45	1.5	1.1	20
E287	24	0.83	0.6	0.98	0.5	79	0.5	79	1.1	0.6	22

See Table 1 for definitions of column headings.

Potential Evapotranspiration

Priestley-Taylor Method

Estimated mean annual Priestley-Taylor potential evapotranspiration ($PET_{Priestley\text{-}Taylor}$) of the Hawaiian Islands is shown in Figure 50.

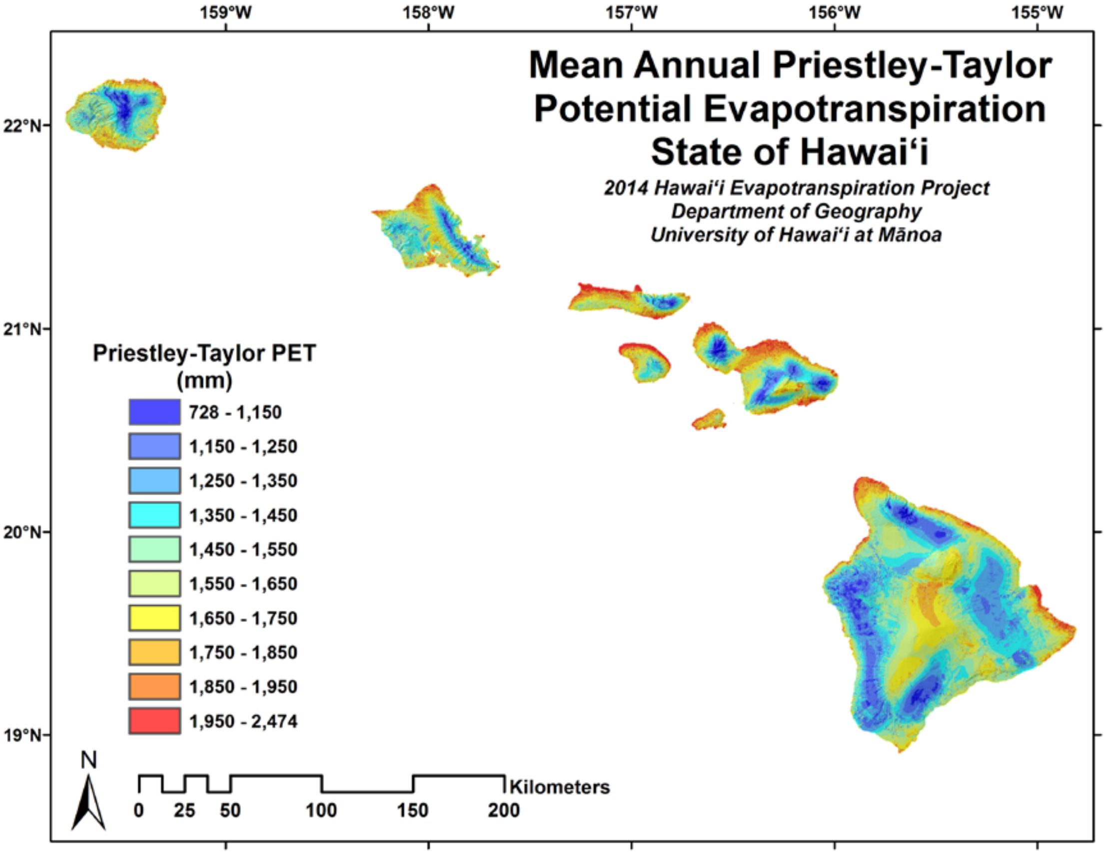

Figure 50. Map of mean annual Priestley-Taylor potential evapotranspiration of Hawaiʻi.

Penman-Monteith Method

Estimated mean annual Penman-Monteith potential evapotranspiration ($PET_{Penman\text{-}Monteith}$) of the Hawaiian Islands is shown in Figure 51.

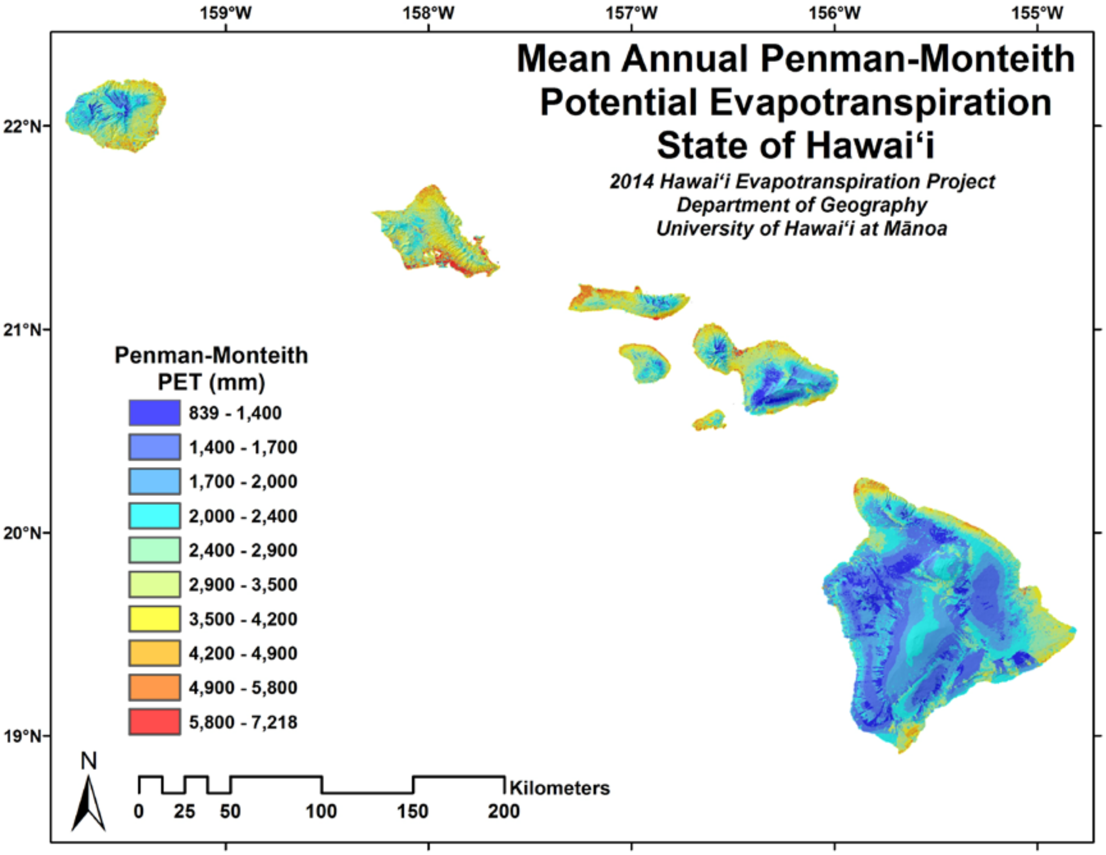

Figure 51. Map of mean annual Penman-Monteith potential evapotranspiration of Hawaiʻi.

Grass Reference Surface PET

Estimated mean annual grass reference surface (Allen et al. 1998) potential evapotranspiration (ET_0) of the Hawaiian Islands is shown in Figure 52.

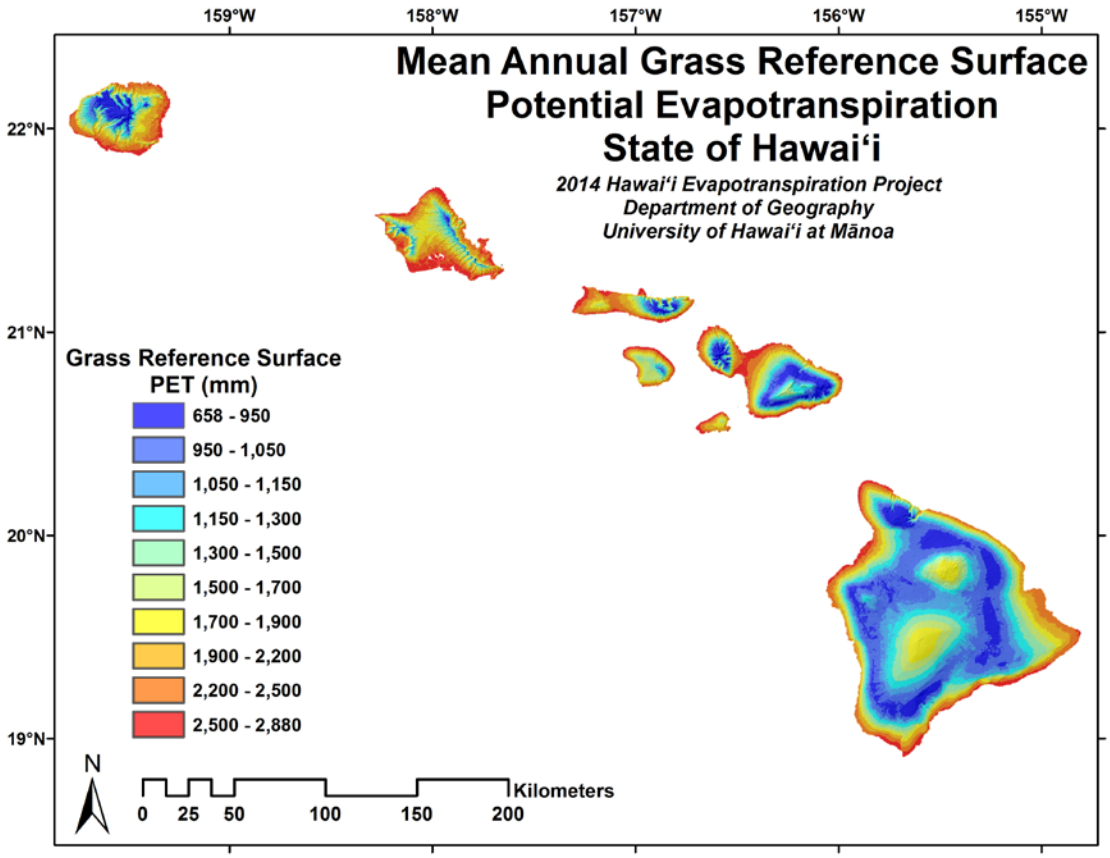

Figure 52. Map of mean annual grass reference surface potential evapotranspiration of Hawaiʻi.

Evapotranspiration

Wet-canopy Evaporation

Estimated mean annual wet-canopy evaporation of the Hawaiian Islands is shown in Figure 53.

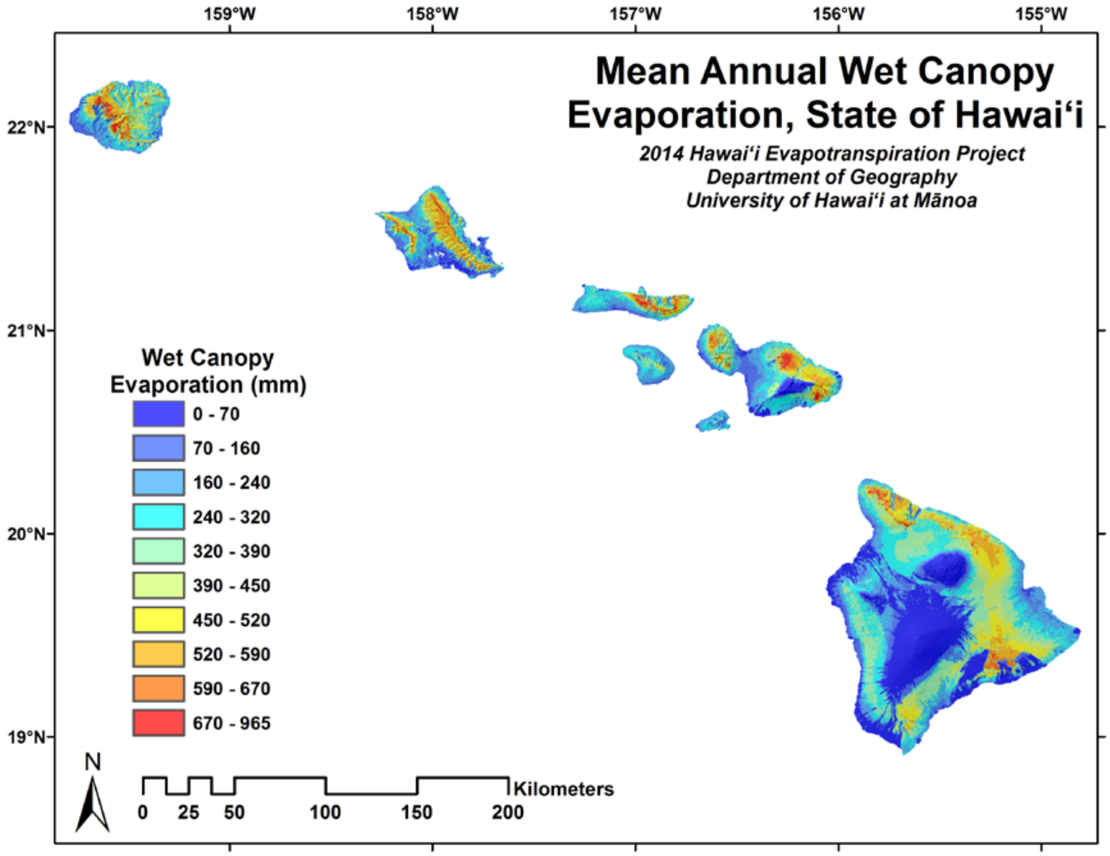

Figure 53. Map of mean annual wet-canopy evaporation of Hawaiʻi.

Transpiration

Estimated mean annual transpiration of the Hawaiian Islands is shown in Figure 54.

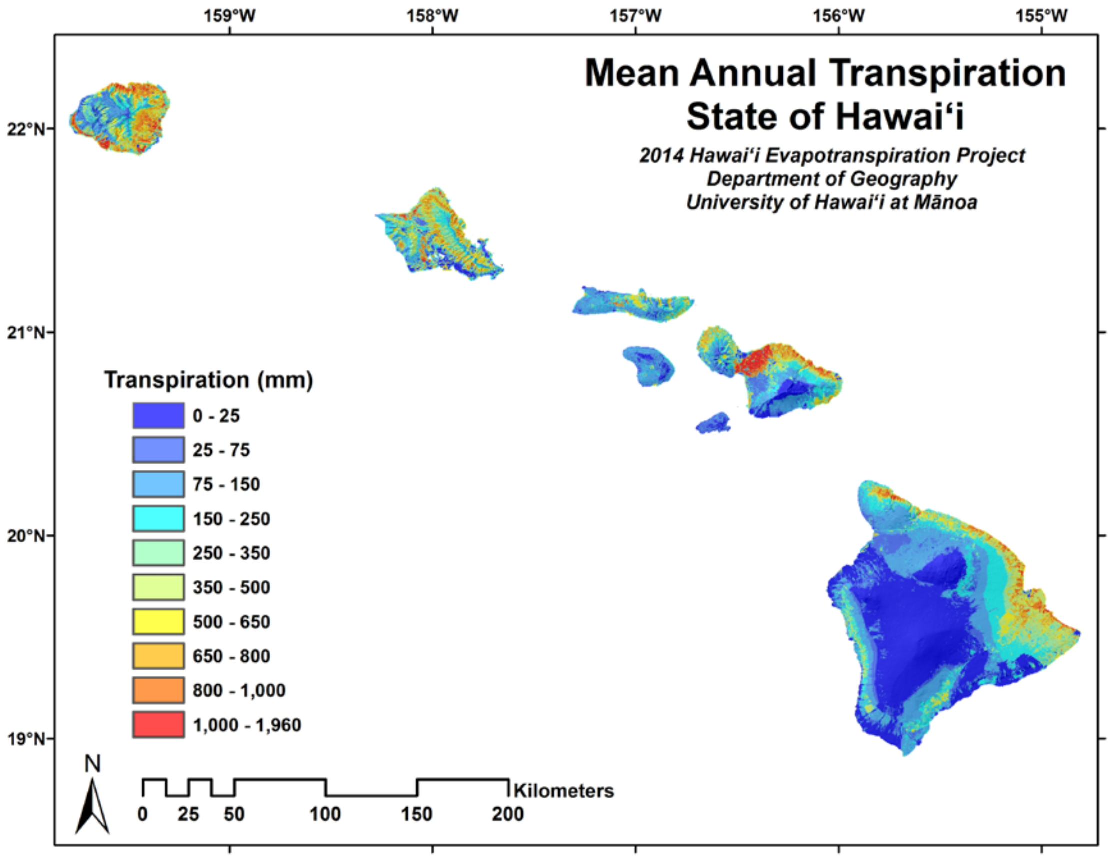

Figure 54. Map of mean annual transpiration of Hawaiʻi.

Soil Evaporation

Estimated mean annual soil evaporation of the Hawaiian Islands is shown in Figure 55.

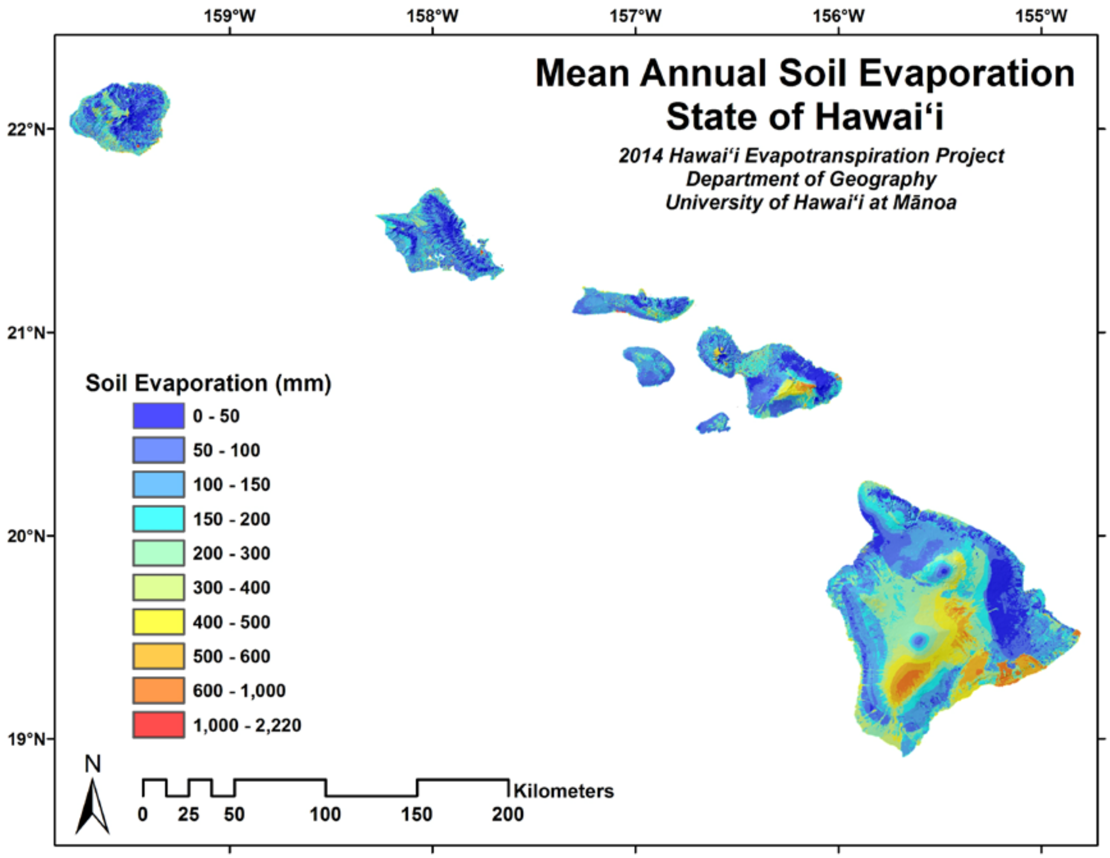

Figure 55. Map of mean annual soil evaporation of Hawaiʻi.

Evapotranspiration

Estimated mean annual evapotranspiration of the Hawaiian Islands is shown in Figure 56 in latent energy flux units (λE, W m^{-2}) and in Figure 57 in water units (ET, mm). For validation purposes, modeled ET estimates are compared with ET at the only four stations with reported ET estimates based on eddy covariance measurements (Figure 58 and Table 24).

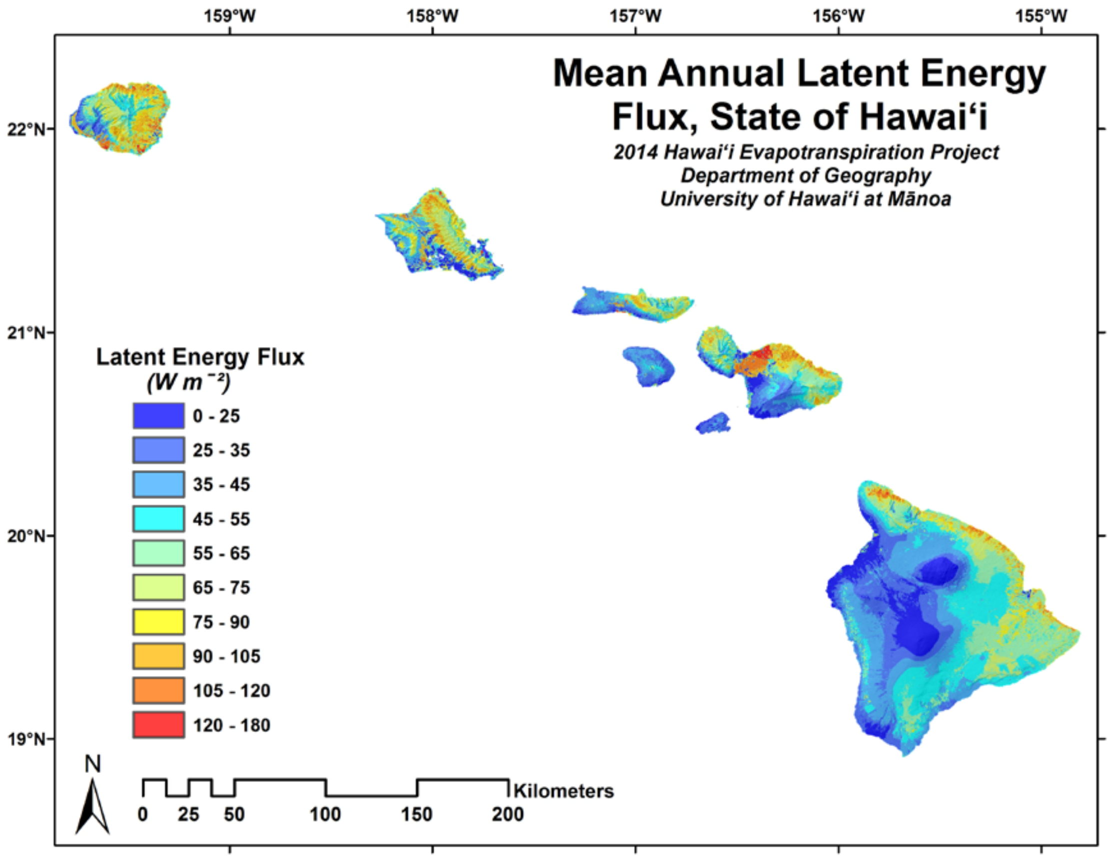

Figure 56. Map of mean annual latent energy flux of Hawaiʻi.

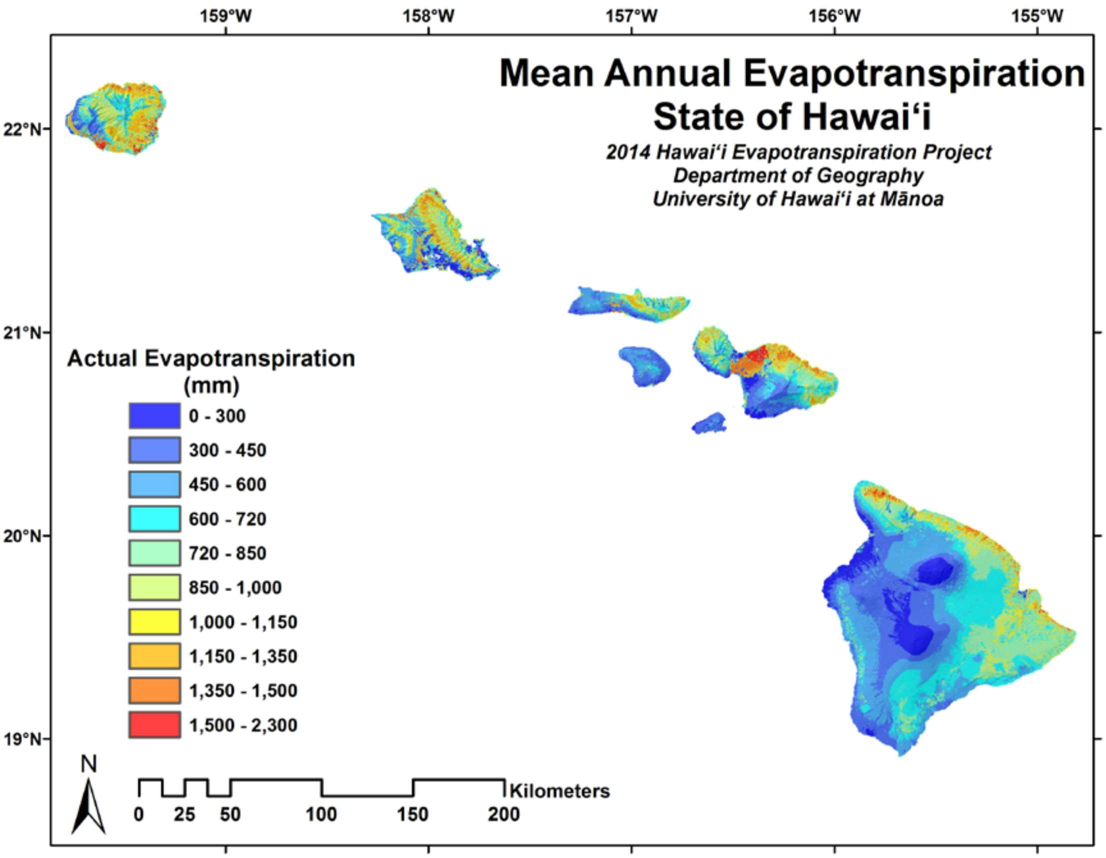

Figure 57. Map of mean annual evapotranspiration of Hawaiʻi.

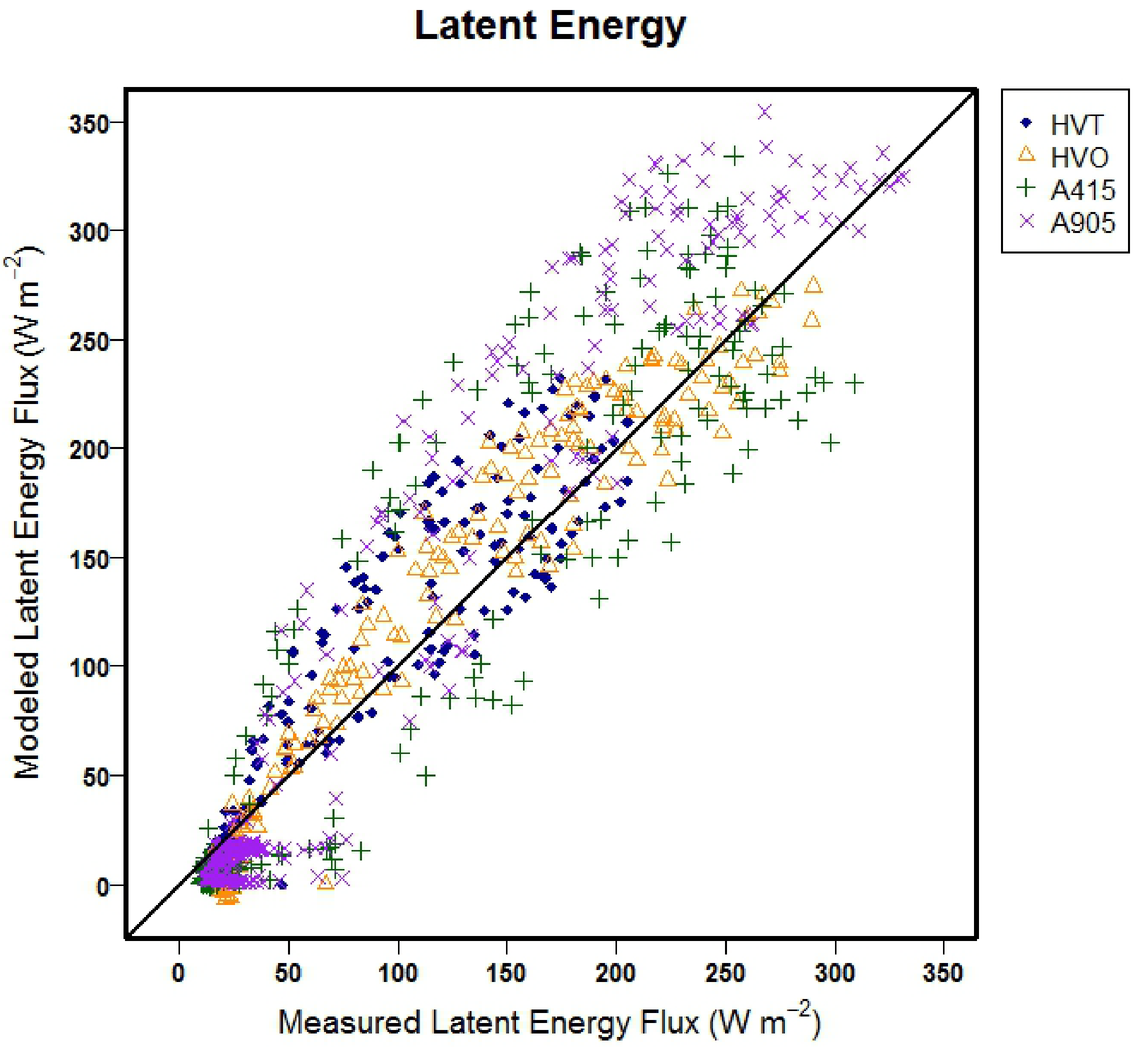

Figure 58. Scatterplot of estimated (mapped) versus eddy covariance estimates of latent energy flux for two flux tower sites in Hawaiʻi.

Table 24. Statistical results of estimated (mapped) versus measured (eddy covariance) mean hourly evapotranspiration for four flux tower sites in Hawaiʻi.

STA. ID	N	b	a	r^2	MBE	MBE%	RMSE	RMSE%	MOD.	MEAS.	N_{obs} (mo.)
All	1152	1.13	-6.5	0.91	4	5	33	40	87	83	93
HVT	288	1.14	-3.2	0.90	5	8	24	38	68	62	34
HVO	288	1.07	-7.1	0.96	-1	-1	20	25	80	81	35
A415	288	1.05	-3.9	0.86	1	1	41	45	92	91	12
A905	288	1.25	-12.1	0.93	12	12	43	44	109	97	12

See Table 1 for definitions of column headings.

Discussion

Error Testing

All variables needed for estimating ET were successfully estimated at 250-m resolution, on a mean annual basis (land cover type), for the 24 hourly values of the mean annual diurnal cycle (wind speed), for the 12 monthly values of the mean annual cycle (albedo, leaf area index, vegetation cover fraction, and soil moisture), or for the 12 x 24 hourly values of the mean diurnal cycles of the 12 calendar months (all other variables). Estimates of each variable independently derived from models developed for this project were tested against validation station observations, except for canopy wetness fraction, and biomass and air layer energy storage. Cloud frequency was not rigorously validated, but estimates were compared at airport locations against ground-observed sky cover (Figures 21 and 22). For canopy wetness fraction and biomass and air layer energy storage, so few stations were available, that all were deemed necessary to develop the best predictive model, and therefore, no stations were available for validation purposes.

All variables for which validation data were available were tested by making estimated versus measured scatterplots and by deriving error statistics. For most variables, testing showed that the estimates were reasonable and accurately represented the spatial and temporal variability. In a few cases, such as soil moisture, albedo, soil heat flux, and relative humidity, validation results were not as good. For soil moisture, albedo, and soil heat flux, we believe this is largely explained by the small sample of available validation stations and the effects of small scale spatial variability on these variables. Albedo is used only for estimating net radiation, which validated well with a much larger number of available stations. The error found in the relative humidity results is probably the result of both the difficulty in modeling a variable with such complex spatial and temporal patterns, and the difficulty in accurately measuring relative humidity. In future efforts to update the *ET* estimates, we recommend that significant effort be put into improving the maps of relative humidity.

Direct *ET* measurements are available for only four sites in Hawaiʻi, where eddy covariance flux towers have been install and operated. Two of those tower sites are in forest ecosystems, one native (HVT) and one invaded with the alien tree species, strawberry guava (*Psidium cattleiatum*). The other two towers are located in the Hawaiʻi and California Sugar Company sugarcane plantation on Maui Island (Anderson and Wang 2014). The results, while representing only a small sample of the Hawaiian Islands, are, nevertheless, very encouraging.

Table 25 summarizes the validation results for this study. Note that for the most important variables estimated in this project, solar radiation and evapotranspiration (latent heat flux), validation showed the estimates to be very reliable. For solar radiation (see Figure 27), with all validation stations combined, estimates were highly correlated with observations ($r^2 = 0.82$) and bias and random errors were very low (MBE = 6 W m^{-2} and RMSE = 78 W m^{-2}, Table 4). In the case of *ET*, using latent energy (*ET* in energy units), estimates were highly correlated with observations ($r^2 = 0.91$) and bias and random errors were very low (MBE = 4 W m^{-2} and RMSE = 24 W m^{-2}, Table 24). In water units, the MBE and RMSE are equivalent to 0.1 and 0.8 mm per day, respectively). These results give confidence in the results of the study.

Table 25. Summary of validation results.

Variable	Units	r^2	MBE	MBE%	RMSE	RMSE%	N
Soil Moisture	ratio	0.58	0.24	66	0.27	76	95
Canopy Wetness Fraction	ratio	No validation performed.					
Clear-sky Solar Radiaiton	W m^{-2}	0.96	15	2	30	3	503
Diffuse Solar Radiation	W m^{-2}	0.64	-8	-3	60	24	108
Cloud Frequency	ratio	No validation performed.					
Solar Radiation	W m^{-2}	0.82	6	1	78	15	4095
Albedo	ratio	0.18	0	-3	3	30	156
Downward Longwave Radiation	W m^{-2}	0.77	-9	-2	17	5	167
Upward Longwave Radiation	W m^{-2}	0.91	3	1	15	4	315
Net Radiation	W m^{-2}	0.94	-5	-4	51	42	1722
Soil Heat Flux	W m^{-2}	0.32	0.28	NA	12.3	NA	864
Biomass Heat Storage	W m^{-2}	No validation performed.					
Air Layer Heat Storage	W m^{-2}	No validation performed.					
Air Temperature	°C	0.89	-0.1	0	0.5	3	12096
Relative Humidity	%	0.21	8	11	19	25	3771
Wind speed	m s^{-1}	0.40	-0.1	-3	0.5	15	840
Latent Energy Flux	W m^{-2}	0.91	4	5	33	40	1152

r^2 = coefficient of determination; MBE = mean bias error in same units as the variable; MBE% = mean bias error expressed as a percent of the mean of the observed values; RMSE = root mean square error in same units as the variable; RMSE% = root mean square error expressed as a percent of the mean of the observed values; N = number points in sample.

Sensitivity Analysis

To assess how errors in forcing variables could affect evapotranspiration estimates, a simple first order sensitivity analysis was conducted. For each of the variables, net radiation (R_{net}), air temperature (T), relative humidity (RH), wind speed (U), leaf area index (LAI), vegetation cover fraction (f_c), vegetation height (h), available soil moisture (θ), and canopy wetness fraction (f_w), a linear regression was conducted with latent energy flux (λE) as the dependent variable. Mapped mean annual values were used, and regressions were done separately for each land cover type. Several land cover types were omitted because of the extremely low number of cells occupied by those land covers. The results of that analysis along with regression results for PET variables vs. λE are given in Appendix Table A9. Summarizing those results, the three forcing variables with the highest coefficients of determination (r^2) for each land cover type are listed in Table 26. R_{net}, θ, and LAI appear in the top three more often that the other variables (26, 24, and 24 times, respectively). Soil moisture (θ) is particular important for the dry and mesic land cover categories. The mean r^2 values for each forcing variable are given in Table 27 based on unweighted averaging (each land cover type given equal weight) and area-weighted averaging (each land cover type weighted by the land area it represents). This result shows clearly that soil moisture (θ) is the variable to which evapotranspiration estimates are most sensitive, followed by leaf area index (LAI), and net radiation (R_{net}).

The high sensitivity of ET estimates to θ, LAI, and R_{net} indicates the importance of making accurate estimates of these variables. Error testing shows that R_{net} is modeled with sufficient accuracy (Table 11). The LAI maps used in our analysis were not tested because of the lack of available validation data. Hence, uncertainty in the MODIS-derived LAI estimates for Hawaiʻi is unknown. For θ, testing was limited to only seven stations, five of which had very short records. Based on that analysis (Table 1), error was relatively high (mean bias error: 66%; RMSE: 76%). As previously stated, some of this error can be explained by the small number of validation stations and the inherent small scale spatial variability of soil moisture.

Nevertheless, the accuracy of *ET* estimates is likely to be affected by uncertainty in soil moisture estimates, especially in relatively dry areas.

Spatial Patterns

Results show that across the State of Hawai'i mean annual solar radiation varies from 130 to 296 W m^{-2}. Low solar radiation is found along cloudy windward slopes below the trade-wind inversion level and in terrain-shaded valleys, while the highest values occur at the high mountain summits of Mauna Kea and Mauna Loa. *ET* has a complex spatial pattern reflecting variations in net radiation, moisture availability, and vegetation characteristics. With a few exceptions, annual ET ranged from less than 50 mm at the dry high mountain summits to around 1,700 mm in sunny, irrigated areas. *ET* is exceptionally low in dry, barren areas, especially leeward areas with young substrates, and hence little or no soil, and very sparse vegetation. In general, *ET* increases with increasing mean annual rainfall when moving inland from dry leeward coasts. Maximum *ET* in natural ecosystems is found at locations with intermediate mean annual rainfall (~1000-2000 mm per year). Moving to areas with higher mean annual rainfall, *ET* declines because of the cloudier conditions, which reduce solar radiation. Species also have noticeable effects on the *ET* pattern. Strawberry guava (*Psidium cattleianum*), for example, is known to have relatively high rates of *ET* in comparison with native trees in Hawai'i (Giambelluca et al. 2008). Based on measured leaf characteristics of strawberry guava (Y. Miyazawa, pers. comm. 2013), it was possible to represent the effects of this widespread invasive tree on *ET* in Hawai'i. Along the area upslope of Hilo in the direction of Volcano on Hawai'i Island, for example, extensive areas of forest have been heavily invaded with strawberry guava. This area was identified as “Introduced Wet-Mesic Forest” in the LANDFIRE data set (Comer et al. 2003). Estimated ET is significantly higher for these invaded forest areas than ET of adjacent native forest. These results help to quantify the hydrological impacts of invasive species in Hawaiʻi.

Web Platform

All of the results of this project, including this report, will be made available in digital form on a project web site, currently under development. When complete, the web site will provide access to all maps produced in this study in GIS and image formats, descriptive information on the methods and results of the study, and an interactive map tool similar to the one provided on the Rainfall Atlas of Hawaiʻi website (http://rainfall.geography.hawaii.edu).

Table 26. Forcing variables to which the latent energy flux estimates are most sensitive for each land cover type. Shown are the three forcing variables with the highest coefficients of determination (r^2) values based on linear regression between the mean annual value of each forcing variable and estimated mean annual latent energy flux.

		1st		2nd		3rd	
LC Code	Landcover Type	Var.	r^2	Var.	r^2	Var.	r^2
1	Developed-Open Space	LAI	0.574	f_c	0.340	R_{net}	0.227
2	Developed-Low Intensity	LAI	0.662	f_c	0.389	R_{net}	0.256
3	Developed-Medium Intensity	LAI	0.650	R_{net}	0.281	f_c	0.121
4	Developed-High Intensity	h	0.534	R_{net}	0.243	LAI	0.090
5	Barren	θ	0.874	RH	0.170	f_w	0.124
6	Mixed Agriculture	LAI	0.411	f_w	0.226	R_{net}	0.210
7	Hawai'i Bog	R_{net}	0.660	h	0.500	T	0.464
8	Hawai'i Lowland Rainforest	U	0.561	R_{net}	0.529	LAI	0.215
9	Hawai'i Montane Cloud Forest	R_{net}	0.453	h	0.377	U	0.325
10	Hawai'i Montane Rainforest	U	0.572	R_{net}	0.474	θ	0.326
11	Hawai'i Wet Cliff and Ridge Crest Shrubland	h	0.458	R_{net}	0.355	U	0.354
12	Hawai'i Lowland Dry Forest	θ	0.732	U	0.407	R_{net}	0.392
13	Hawai'i Lowland Mesic Forest	U	0.560	$Rnet$	0.500	θ	0.459
14	Hawai'i Montane-Subalpine Dry Forest and Woodland	θ	0.706	f_c	0.241	LAI	0.237
15	Hawai'i Montane-Subalpine Mesic Forest	θ	0.697	R_{net}	0.690	U	0.541
16	Hawai'i Lowland Dry Shrubland	θ	0.803	R_{net}	0.471	LAI	0.378
17	Hawai'i Lowland Mesic Shrubland	R_{net}	0.488	U	0.248	LAI	0.232
18	Hawai'i Lowland Dry Grassland	θ	0.826	T	0.381	RH	0.335
19	Hawai'i Lowland Mesic Grassland	θ	0.637	R_{net}	0.470	LAI	0.465
20	Hawai'i Montane-Subalpine Dry Shrubland	θ	0.817	RH	0.150	f_c	0.120
21	Hawai'i Montane-Subalpine Dry Grassland	θ	0.772	f_c	0.455	R_{net}	0.426

Table continues on next page.

Table 26. (continued).

		1st		2nd		3rd	
LC Code	Landcover Type	Var.	r^2	Var.	r^2	Var.	r^2
22	Hawai'i Montane-Subalpine Mesic Grassland	LAI	0.830	θ	0.829	T	0.536
23	Hawai'i Alpine Dwarf-Shrubland	U	0.787	θ	0.583	LAI	0.442
24	Hawai'i Dry Cliff	θ	0.671	LAI	0.617	h	0.498
25	Hawai'i Dry Coastal Strand	θ	0.820	T	0.442	RH	0.220
27	Hawai'i Subalpine Mesic Shrubland	θ	0.769	LAI	0.327	R_{net}	0.095
30	Hawaiian Introduced Wetland Vegetation-Herbaceous	R_{net}	0.614	LAI	0.128	U	0.126
31	Hawaiian Introduced Dry Forest	θ	0.618	LAI	0.432	f_c	0.121
32	Hawaiian Introduced Wet-Mesic Forest	LAI	0.435	R_{net}	0.328	f_c	0.238
33	Hawaiian Introduced Deciduous Shrubland	LAI	0.695	θ	0.669	f_c	0.425
34	Hawaiian Introduced Perennial Grassland	θ	0.646	LAI	0.514	f_c	0.275
35	Hawaiian Introduced Evergreen Shrubland	LAI	0.620	h	0.349	f_c	0.300
36	Introduced Coastal Wetland Vegetation - Tree	θ	0.463	h	0.380	LAI	0.235
39	Hawaiian Managed Tree Plantation	R_{net}	0.561	T	0.313	U	0.268
40	Open Water	θ	0.692	f_w	0.293	f_c	0.264
41	Coastal Kiawe	LAI	0.574	θ	0.393	f_c	0.392
42	Agriculture - Sugarcane	R_{net}	0.645	θ	0.344	LAI	0.284
43	Agriculture - Pineapple	R_{net}	0.625	LAI	0.534	f_c	0.517
44	Agriculture - Macadamia Nut	θ	0.740	R_{net}	0.615	f_c	0.539
45	Agriculture - Coffee	U	0.806	R_{net}	0.775	f_w	0.668
46	Agriculture - Taro	R_{net}	0.612	U	0.381	h	0.283

LC Code = Land cover code; R_{net} = net radiation (W m^{-2}); T = air temperature (°C); RH = relative humidity (%); U = wind speed (m s^{-1}); LAI = leaf area index (ratio); f_c = vegetation cover fraction (ratio); h = vegetation height (m); θ = available soil moisture (ratio); f_{wet} = canopy wetness fraction (ratio).

Table 27. Mean coefficients of determination (r^2) based on linear regression of each forcing variable against latent energy flux. Regressions used mean annual values and were conducted separately for each land cover type. Means are derived using unweighted averaging (equal weights for each land cover type) and area-weighted averaging (r^2 of each land cover type weighted by its area).

Unweighted		Weighted by area	
Variable	Mean r^2	Variable	Mean r^2
θ	0.412	θ	0.498
LAI	0.323	LAI	0.309
R_{net}	0.305	R_{net}	0.228
U	0.214	f_c	0.194
f_c	0.202	U	0.191
h	0.157	h	0.108
T	0.148	RH	0.067
RH	0.119	f_w	0.059
f_w	0.116	T	0.047

References Cited

Ackerman, S.A., Holz, R.E., Frey, R., Eloranta, E.W., Maddux, B.C., and McGill, M. 2008. Cloud detection with MODIS. Part II: validation. *Journal of Atmospheric and Oceanic Technology* 25: 1073-1086.

Ackerman, S., Strabala, K., Menzel., P., Frey, R., Moeller, C., Gumley, L., Baum, B., Seeman, S.W., Zhang, H. 2002. Discriminating clear-sky from cloud with MODIS, algorithm theoretical basis document. NASA Goddard Space Flight Cent. Greenbelt, MD, USA, 112 pp.

Allen, R.G., Pereira, L.S., Raes, D., and Smith, M. 1998. Crop evapotranspiration – Guidelines for computing crop water requirements. FAO Irrigation and Drainage Paper no. 56, Food and Agriculture Organization of the United Nations, Rome.

Anderson, R.G. and Wang, D. 2014. Energy budget closure observed in paired Eddy Covariance towers with increased and continuous daily turbulence. *Agricultural and Forest Meteorology* 184: 204-209, doi:10.1016/j.agrformet.2013.09.012.

AWS Truewind. 2004. Wind energy resource maps of Hawaii. AWS Truewind, LLC, Albany, NY, USA.

Barnes, M.L. 2013. An assessment of diurnal and seasonal cloud cover changes over the Hawaiian Islands using Terra and Aqua MODIS. Masters' thesis, Natural Resources and Environmental Management, University of Hawaiʻi at Mānoa, Honolulu, USA.

Bonan, G. 2008. *Ecological climatology, concepts and applications*, second edition. Cambridge University Press, Cambridge, UK, 563 pp.

Cabin, R.J., Weller, S.G., Lorence, D.H., Flynn, T.W., Sakai, A.K., Sandquist, D., and Hadway, L.J. 2000. Effects of long-term ungulate exclusion and recent alien species control on the preservation and restoration of a Hawaiian tropical dry forest. *Conservation Biology* 14: 439-453.

Cao, G., Giambelluca, T.W., Stevens, D., and Schroeder, T. 2007. Inversion variability in the Hawaiian trade wind regime. *Journal of Climate* 20: 1145-1160.

Carmo-Silva, A.E., Powers, S.J., Keys, A.J., Arrabaça, M.C., and Parry, M.A.J. 2008. Photorespiration in C_4 grasses remains slow under drought conditions. *Plant, Cell and Environment* 31: 925-940.

Comer, P., Faber-Langendoen, D., Evans, R., Gawler, S., Josse, C., Kittel, G., Menard, S., Pyne, M., Reid, M., Schulz, K., Snow, K., and Teague, J. 2003. Ecological systems of the United States: A working classification of U.S. terrestrial systems. NatureServe, Arlington, Virginia.

Ekern, P.C., and Chang, J.H. 1985, Pan evaporation; State of Hawaiʻi, 1894–1983: State of Hawaiʻi, Department of Land and Natural Resources, Division of Water and Land Development, Report R74, 172 p.

Engott, J.A., 2011. A water-budget model and assessment of groundwater recharge for the Island of Hawaiʻ i: U.S. Geological Survey Scientific Investigations Report 2011–5078, 53 p.

Ewe, S.M.L., and Sternberg, L.d.S.L. 2003. Seasonal gas exchange characteristics of *Schinus terebinthifolius* in a native and disturbed upland community in Everglades National Park, Florida. *Forest Ecology and Management* 179: 27-36.

Feidas, H., Cartalis, C., and Lagouvardos, C. 2002. Temporal simulation of diurnal temperature and relative humidity evolution at a forested mountainous site in Attica, Greece. *International Journal of Wildland Fire* 11: 95-106.

Frey, R. A., Ackerman, S.A., Liu, Y., Strabala, K.I., Zhang, H., Key, J.R., and Wang, X. 2008. Cloud detection with MODIS. Part I: Improvements in the MODIS cloud mask for collection 5. *Journal of Atmospheric and Oceanic Technology* 25: 1057-1072.

Giambelluca, T.W. 1983. Water balance of the Pearl Harbor-Honolulu basin, Hawaiʻi, 1946–1975. Tech. Rep. No. 151, Water Resources Research Center, University of Hawaiʻi, Honolulu, 151 pp.

Giambelluca, T.W., Nullet, M.A., and Schroeder, T.A. 1986. Rainfall atlas of Hawaiʻi: State of Hawaiʻi, Department of Land and Natural Resources, Division of Water and Land Development, Report R76, 267 pp.

Giambelluca, T.W., DeLay, J.K., Asner, G.P., Martin, R.E., Nullet, M., Huang, M., Mudd, R.G., and Takahashi, M. 2008. Stand structural controls on evapotranspiration in native and invaded tropical montane cloud forest in Hawaiʻi. American Geophysical Union Fall Meeting, San Francisco, December, 2008.

Giambelluca, T.W., Chen, Q., Frazier, A.G., Price, J.P., Chen, Y.-L., Chu, P.-S., Eischeid, J.K., and Delparte, D.M. 2013. Online rainfall atlas of Hawaiʻi. *Bulletin of the American Meteorological Society* 94: 157-160, doi:10.1175/BAMS-D-11-00228.1.

Gon, III, S.M., Allison, A., Cannarella, R.J., Jacodi, J.D., Kido, M.H., Miller, S.E., and Orodenker, D.E. 1999. Hawaiʻi: A tropical insular approach to gap analysis. *GAP Analysis Program Bulletin*, No. 8, December 1999, http://www.gap.uidaho.edu/bulletins/8/gapbulletin8.pdf.

Gotsch, S.G., Crausbay, S.D., Weintraub, A., Giambelluca, T.W., Longman, R., Asbjornsen, H., Hotchkiss, S.C., Dawson, T., and Longman, R.J. In review. Water relations and microclimate around the upper limit of cloud forest in Maui, Hawaiʻi. Submitted to *Tree Physiology*.

Gueymard, C.A. 2008. REST2: High-performance solar radiation model for cloudless-sky irradiance, illuminance, and photosynthetically active radiation – Validation with a benchmark dataset. *Solar Energy* 82: 272-285.

Gueymard, C.A. 2012. Clear-sky irradiance predictions for solar resource mapping and large-scale applications: improved validation methodology and detailed performance analysis of 18 broadband radiative models. *Solar Energy* 86: 2145–2169.

Gutiérrez, M.V., Meinzer, F.C., and Grantz, A. 1994. Regulation of transpiration in coffee hedgerows: covariation of environmental variables and apparent responses of stomata to wind and humidity. *Plant, Cell and Environment* 17: 1305-1313.

Huete, A., Didan, K., Miura, T., Rodriguez, E.P., Gao, X., and Ferreira, L.G. 2002. Overview of the radiometric and biophysical performance of the MODIS vegetation indices. *Remote Sensing of Environment* 83: 195-213.

Izuka, S.K., Oki, D.S., and Chen, C.-H. 2005. Effects of irrigation and rainfall reduction on ground-water recharge in the Lihue Basin, Kauai, Hawaii. Scientific Investigations Report 2005-5146, U.S. Geological Survey, 48 pp.

Jarvis, P.G. 1976. The interpretation of the variations in leaf water potential and stomatal conductance found in canopies in the field. Philosophical Transactions of the Royal Society of London, Series B 273: 593-610.

Kelliher, F.M., Leuning, R., Raupach, M.R., and Schulze, E.-D. 1995. Maximum conductances for evaporation from global vegetation types. *Agricultural and Forest Meteorology* 73: 1-16.

Kraus, K.W., and Allen, J.A. 2003. Influences of salinity and shade on seedling photosynthesis and growth of two mangrove species, *Rhizophora mangle* and *Bruguiera sexangula*, introduced to Hawaiʻi. *Aquatic Botany* 77: 311-324.

La Mer, V.K. and Healy, T.W. 1965. Evaporation of water: Its retardation by monolayers. *Science* 148: 36–41.

Li, S., Reza Pezeshki, S., and Goodwin, S. 2004. Effects of soil moisture regimes on photosynthesis and growth in cattail (*Typha latifolia*). *Acta Oecologia* 25: 17-22.

Lloyd, J. 1991. Modelling stomatal responses to environment in *Macademia integrifolia*. *Australian Journal of Plant Physiology* 18: 649-660.

Longman, R.J. 2012. Homogenization of long-term solar radiation time series using a clear-sky radiation model and assessment of solar radiation variability at upper elevations on Maui, Hawaiʻi. Master's thesis, Geography, University of Hawaiʻi at Mānoa, Honolulu, USA, 86 pp.

Longman, R.J., Giambelluca, T.W, and Nullet, M.A. 2013. Use of a clear-day solar radiation model to homogenize solar radiation measurements in Hawaiʻi. *Solar Energy* 91: 102-110.

Longman, R.J., Giambelluca, T.W., and Frazier, A.G. 2012. Modeling clear sky solar radiation across a range of elevations in Hawaiʻi: Comparing the use of input parameters at different temporal resolutions. *Journal of Geophysical Research-Atmospheres* 117, D02201.

Lowe, P.R. 1977. An approximating polynomial for the computation of saturation vapor pressure. *Journal of Applied Meteorology* 16: 100-103.

Marler, T.E., and Mickelbart, M.V. 1998. Drought, leaf gas exchange, and chlorophyll fluorescence of field-grown papaya. *Journal of the American Society for Horticultural Science* 123: 714-718.

McAlpine, K.G., Jesson, L.K., and Kubien, D.S. 2008. Photosynthesis and water-use efficiency: a comparison between invasive (exotic) and non-invasive (native) species. *Austral Ecology* 33: 10-19.

Meinzer, F.C., and Grantz, D.A. 1989. Stomatal control of transpiration from a developing sugarcane canopy. *Plant, Cell and Environment* 12: 635-642.

Meyers, T.P., and Hollinger, S.E. 2004. An assessment of storage terms in the surface energy balance of maize and soybean. *Agricultural and Forest Meteorology* 125: 105-115.

Michiles, A.A.d.S., and Gielow, R. 2008. Above-ground thermal energy storage rates, trunk heat fluxes and surface energy balance in a central Amazonian rainforest. *Agricultural and Forest Meteorology* 148: 917-930.

Monteith, J.L. 1965. Evaporation and environment. In G.E. Fogg (ed.) Symposium of the Society for Experimental Biology, The State and Movement of Water in Living Organisms, Vol. 19, pp. 205-234, Academic Press, Inc., NY, USA.

Mu, Q., Zhao, M., and Running, S.W. 2007. Improvements to a MODIS global terrestrial evapotranspiration algorithm. *Remote Sensing of Environment* 115: 1781-1800.

Penman, H.L. 1948. Natural evaporation from open water, bare soil and grass. *Proceedings of the Royal Society A* 193: 120-145.

Neales, T.F., Sale, P.J.M., and Meyer, C.P. 1980. Carbon dioxide assimilation by pineapple plants, *Ananas comosus* (L.) Merr. II. Effects of variation of the day/night temperature regime. *Australian Journal of Plant Physiology* 7: 375-285.

Nilsen, E.T., Sharifi, M.R., Rundel, P.W., Jarrell, W.M., and Virgina, R.A. 1983. Diurnal and seasonal water relations of the desert phreatophyte *Prosopis glandulosa* (honey mesquite) in the Sonoran Desert of California. *Ecology* 64: 1381-1393.

NOAA. 2011. Earth System Research Laboratory Global Monitoring Division. National Oceanic and Atmospheric Adiminstration. Retrieved 10/01/2010, http://www.esrl.noaa.gov/gmd/ozwv/.

Norman, J.M., Kustas, W.P., and Humes, K.S. 1995. Source approach for estimating soil and vegetation energy fluxes in observations of directional radiometric surface temperature. *Agricultural and Forest Meteorology* 77: 263-293.

Ohkubo, S., Kosugi, Y., Takanashi, S., Matsuo, N., Tani, M., and Nik, A.R. 2008. Vertical profiles and storage fluxes of CO_2, heat and water in a tropical rainforest at Pasoh, Peninsular Malaysia. *Tellus* 60B: 569-582.

Oki, D.S. 2002. Reassessment of ground-water recharge and simulated ground-water availability for the Hawi area of north Kohala, Hawai‘i. Water-Resources Investigations Report 02-4006, U.S. Geological Survey, 62 pp.

Pasquet-Kok, J., Creese, C., and Sack, L. 2010. Turning over a new ‘leaf’: multiple functional singifcances of leaves versus phyllodes in Hawaiian *Acacia koa*. *Plant, Cell and Environment* 33: 2084-2100.

Priestley, C.H.B., and Taylor, R.J. 1972. On the assessment of surface heat flux and evaporation using large-scale parameters. *Monthly Weather Review* 100: 81–92.

Pugnaire, F.I., Haase, P., Incoll, L.D., and Clark, S.C. 1996. Response of the tussock grass *Stipa tenacissima* to watering in a semi-arid environment. *Functional Ecology* 10: 265-274.

Robinson, J.C., and Bower, J.P. 1988. Transpiration from banana leaves in the subtropics in response to diurnal and seasonal factors and high evaporative demand. *Scientia Horticulturae* 37: 129-143.

Samson, R., and Lemeur, R. 2001. Energy balance storage terms and big-leaf evapotranspiration in a mixed deciduous forest. *Annals of Forest Science* 58: 529-541.

Santiago, L.S., Goldstein, G., Meinzer, F.C., Fownes, J., and Mueller-Dombois, D. 2000. Transpiration and forest structure in relation to soil waterlogging in a Hawaiian montane cloud forest. *Tree Physiology* 20: 673-681

Shade, P.J., and Nichols, W.D. 1996. Water budget and the effects of land-use changes on groundwater recharge, Oahu, Hawaii. Professional Paper 1412-C, U.S. Geological Survey, 38 pp.

Shade, P.J., and Nichols, W.D. 1996. Water budget and the effects of land-use changes on ground-water recharge, Oahu, Hawaii: U.S. Geological Survey Professional Paper 1412–C, 38 p.

Shuttleworth, W.J. 2012. *Terrestrial hydrometeorology*. John Wiley and Sons, Ltd., Chichester, UK, 448 pp.

Silberstein, R., Held, A., Hatton, T., Viney, N., Sivapalan, M. 2001. Energy balance of a natural jarrah (*Eucaliptus marginata*) forest in Western Australia: measurements during the spring and summer. *Agricultural and Forest Meteorology* 109: 79–104.

Sims, D.A., and Pearcy, R.W. 1989. Photosynthetic characteristics of a tropical forest understory herb, *Alocasia macrorrhiza*, and a related crop species, *Colocasia esculenta* grown in contrasting light environments. *Oecologia* 79, 53-59.

Stewart, J.B. 1988. Modelling surface conductance of pine forest. Agricultural and *Forest Meteorology* 43: 19-35.

Strabala, K. 2005. *MODIS cloud mask user's guide*. Retrieved January 2012 from http://modis-atmos.gsfc.nasa.gov/_docs/CMUSERSGUIDE.pdf .

Sugita, M., and Brutsaert, W. 1993. Cloud effect in the estimation of instantaneous downward longwave radiation. *Water Resources Research* 29: 599-605.

Tuberosa, R., Sanguineti, M.C., and Landi, P. 1994. Abscisic acid concentration in leaf and xylem sap, leaf water potential, and stomatal conductance in maize. *Crop Science* 34: 1557-1563.

U.S. Naval Observatory. N.D. Sun or moon rise/set table for one year. Astronomical Applications Department, U.S. Naval Observatory, Washington, DC, USA. http://aa.usno.navy.mil/data/docs/RS_OneYear.php

van de Griend, A.A. and Owe, M. 1994. Bare soil surface resistance to evaporation by vapor diffusion under semiarid conditions. *Water Resources Research* 30: 181-188.

Vancutsem, C., Pekel, J.F., Bogaert, P., and Defourny, P. 2007. Mean compositing, an alternative strategy for producing temporal syntheses. Concepts and performance assessment for SPOT VEGETATION time series. *International Journal of Remote Sensing* 28: 5123-5141.

Wang, R., and Zhang, Q. 2011. An assessment of storage terms in the surface energy balance of a subalpine meadow in northwest China. *Advances in Atmospheric Sciences* 28: 691-698.

Wilcox, S., and Andreas, A. 2010. Solar resource & meteorological assessment project (SOLRMAP): Kalaeloa Oahu, Hawaii rotating shadowband radiometer

(RSR). Report NREL/DA-5500-56497, National Renewable Energy Laboratory, Golden, CO, USA.

Williams, D.G., and Baruch, Z. 2000. African grass invasion in the Americas: ecosystem consequences and the role of ecophysiology. *Biological Invasions* 2: 123-140.

Williams, D.G., Mack, R.N., and Black, R.A. 1995. Ecophysiology of introduced *Pennisetum setaceum* on Hawaiʻi: the role of phenotypic plasticity. *Ecology* 76: 1569-1580.

Yang, W., Shabanov, N.V., Huang, D., Wang, W., Dickinson, R.E., Nemani, R. ., Knyazikhin, Y., and Myneni, R.B. 2006. Analysis of prototype collection 5 products of leaf area index from Terra and Aqua MODIS sensors. *Remote Sensing of Environment* 104: 297–312.

Yang, Y., Xie, S.P., Hafner, J. 2008a. The thermal wake of Kauai Island: satellite observations and numerical simulations. *Journal of Climate* 21: 4568-4586.

Yang, Y., Xie, S.-P., and Hafner, J. 2008b. Cloud patterns lee of Hawaii Island: A synthesis of satellite observations and numerical simulation. *Journal of Geophysical Research* 113: D15126.

Appendix Tables

Appendix Table A1. Stations used develop monthly temperature model.

Station Name	Network	ID	Isle.	El. (m)	Start	End
Aloha Stadium Halawa	NCDC	172	Oa	12	Sep-71	Apr-77
Byu Laie 903.1	NCDC	242	Oa	6	Sep-71	Dec-94
Camp Mokuleia 841.16	NCDC	305	Oa	2	Jul-77	Jan-97
Church College Laie	NCDC	340	Oa	6	Jun-69	May-71
Coconut Island 840.1	NCDC	350	Oa	5	May-53	Jan-73
Eleele 927	NCDC	470	Ka	46	Sep-45	Jan-66
Ewa Plantation 741	NCDC	507	Oa	6	Sep-45	Jan-74
Haiku 490	NCDC	832	Ma	149	Sep-45	Nov-47
Haina 214	NCDC	840	Ha	141	Sep-45	Apr-71
Haleakala Exp Farm 434	NCDC	995	Ma	640	Sep-45	Jan-70
Haleakala R S 338	NCDC	1004	Ma	2122	Sep-45	Nov-97
Haleakala Summit 338	NCDC	1008	Ma	3038	Mar-53	Jul-71
Hana 354	NCDC	1122	Ma	37	Sep-45	Nov-56
Hana 354 Airport 355	NCDC	1125	Ma	23	Nov-46	Nov-97
Hawaii Volcns Np Hq 54	NCDC	1303	Ha	1211	Sep-45	Nov-97
Hawi 168	NCDC	1339	Ha	177	Feb-89	Nov-97
Hilo 86a	NCDC	1484	Ha	12	Sep-45	May-57
Hilo Nternational Ap	NCDC	1492	Ha	12	Sep-45	Nov-97
Homestead Field 524	NCDC	1598	Mo	138	Nov-45	Dec-52
Honolulu INTL AP 703	NCDC	1919	Oa	2	Sep-45	Nov-97
Honolulu Observ 702.2	NCDC	1918	Oa	2	Jul-58	Nov-97
Honolulu Subst. 407	NCDC	1924	Oa	4	Sep-45	Oct-72
Honomu Mauka 138	NCDC	1960	Ha	335	Sep-45	Mar-59
Kaanapali Airport 453.1	NCDC	2307	Ma	2	Apr-64	Dec-81
Kaanapali Ap 453.1	NCDC	2317	Ma	3	Sep-45	Mar-59
Kahoolawe 499.6	NCDC	2558	Ko	366	Jul-87	Nov-97
Kahuku 912	NCDC	2570	Oa	5	Sep-45	Dec-68
Kahului Wso Ap 398	NCDC	2572	Ma	16	Mar-50	Nov-97
Kailua 446	NCDC	2679	Ma	213	Sep-45	Nov-97
Kainaliu 73.2	NCDC	2751	Ha	457	Sep-45	Nov-97
Kalaupapa 563	NCDC	2896	Mo	9	Sep-45	Nov-97
Kamuela 192.2	NCDC	3077	Ha	814	Oct-46	Feb-76
Kamuela Airport 191	NCDC	3078	Ha	813	Apr-49	Sep-66
Kanalohuluhulu 1075	NCDC	3099	Ka	1098	Aug-61	Nov-97
Kaneohe 838.1	NCDC	3118	Oa	18	Jun-93	Nov-97
Kaneohe Mauka 781	NCDC	3113	Oa	58	Sep-45	Mar-94
Kaneohe Ranch 838	NCDC	3123	Oa	113	Sep-45	Feb-66

Table continues on following page.

Appendix Table A1. (continued)

Station Name	Network	ID	Isle.	El. (m)	Start	End
Kapaka Farm 904.1	NCDC	3208	Oa	3	Jan-95	Nov-97
Kapalua W Maui Ap 462	NCDC	3317	Ma	73	Feb-83	Nov-97
Kapoho Beach 93.11	NCDC	3368	Ha	3	May-73	Feb-81
Keaau 92	NCDC	3872	Ha	67	Jan-77	Nov-97
Ke-Ahole Point 68.13	NCDC	3911	Ha	6	Dec-58	Mar-74
Kealakekua 26.2	NCDC	3977	Ha	451	Jun-57	Nov-97
Kealia 1112	NCDC	3982	Ka	3	Sep-45	May-60
Keawakapu Beach 260.2	NCDC	4193	Ma	6	Jun-64	Jan-78
Kekaha 944	NCDC	4272	Ka	3	Aug-76	Sep-96
Kepuhi Sheraton 550.2	NCDC	4400	Mo	43	Apr-95	Sep-97
Kii-Kahuku 911	NCDC	4500	Oa	5	Feb-76	Nov-97
Kilauea 1134	NCDC	4561	Ka	98	Sep-45	Nov-97
Kilauea Point 1133	NCDC	4568	Ka	55	Dec-45	Dec-80
Kohala 179.1	NCDC	4670	Ha	95	Sep-45	Mar-59
Kohala Mission 175.1	NCDC	4680	Ha	165	Sep-45	Mar-74
Kole Kole	NCDC	4725	Ma	3057	Jul-48	Aug-54
Koloa 936	NCDC	4742	Ka	73	Sep-45	Nov-50
Kona Airport 68.3	NCDC	4764	Ha	9	Sep-45	Dec-75
Kualapuu 534	NCDC	4778	Mo	252	Sep-45	Jan-73
Kukuihaele Mill 206	NCDC	4938	Ha	91	Sep-45	Jun-72
Kula Brch Stn 324.5	NCDC	5000	Ma	930	Mar-75	Nov-97
Kula Hospital 267	NCDC	5004	Ma	916	Apr-75	Nov-97
Kula Sanatorium 267	NCDC	5006	Ma	915	Sep-45	Feb-77
Kulani Camp 79	NCDC	5011	Ha	1576	Sep-47	Jul-94
Kulani Mauka 76	NCDC	5018	Ha	2530	Dec-50	Apr-75
Lahaina 361	NCDC	5177	Ma	12	Sep-45	Sep-00
Lalamilo Fld Of 191.1	NCDC	5260	Ha	797	Apr-76	Nov-00
Lanai Airport 656	NCDC	5275	La	396	Sep-45	Nov-97
Lanai City 672	NCDC	5286	La	494	Sep-45	Nov-97
Lihue 1020	NCDC	5575	Ka	63	Sep-45	Mar-59
Lihue Wso Ap 1020.1	NCDC	5580	Ka	31	Jan-46	Nov-97
Lualualei 804	NCDC	5647	Oa	34	Apr-46	Jul-72
Lunalilo Home 724.2	NCDC	5675	Oa	12	Sep-53	Mar-59
Mahaulepu 941.1	NCDC	5710	Oa	24	Mar-76	Nov-97
Mahinahina 466	NCDC	5715	Ma	220	Nov-52	Mar-59
Mahukona 159	NCDC	5721	Ha	3	Sep-45	Nov-51
Makaha CTRY Club 800.3	NCDC	5758	Oa	76	Aug-93	Nov-97
Makaha Valley 800.1	NCDC	5781	Oa	49	Dec-53	Mar-59

Table continues on following page.

Appendix Table A1. (continued)

Station Name	Network	ID	Isle.	El. (m)	Start	End
Makahuena Pt 940.1	NCDC	5785	Ka	16	Dec-53	Feb-72
Makapuu Point 724	NCDC	5800	Oa	164	Sep-46	Nov-69
Makaweli 965	NCDC	5864	Ka	43	Sep-45	Nov-97
Makena Golf Crs 249.1	NCDC	5842	Ma	30	Apr-78	Nov-97
Mana 1026	NCDC	6082	Ka	6	Sep-45	Mar-74
Manoa Lyon Arboretum	NCDC	6128	Oa	152	Feb-71	Nov-97
Matsonia Drive 720	NCDC	6169	Oa	250	Sep-45	Oct-57
Mauna Kea Obs 1	NCDC	6183	Ha	4199	Jan-73	Dec-77
Mauna Loa 511	NCDC	6190	Ha	326	Sep-45	Jan-73
Mauna Loa Slope Obs	NCDC	6198	Ha	3399	Dec-50	Nov-00
Molokai AP 524	NCDC	6534	Mo	137	Jan-53	Nov-97
Mtn VIEW #3 91.9	NCDC	6546	Ha	584	Sep-86	Oct-94
Mountain View 91	NCDC	6552	Ha	466	Sep-45	Sep-81
Mountain View No 2	NCDC	6560	Ha	482	Nov-81	Nov-85
Naalehu 14	NCDC	6588	Ha	244	Aug-50	Nov-97
Napoopoo 28	NCDC	6697	Ha	122	Sep-45	Jul-57
Niu Ridge 1035	NCDC	6850	Ka	381	Sep-45	Jun-76
Niulii 179	NCDC	6806	Ha	24	Sep-45	Oct-64
Ohe'o 258.6	NCDC	7000	Ma	37	Oct-94	Nov-97
Olaa 92	NCDC	7023	Ha	85	Sep-45	Nov-58
Ookala 223	NCDC	7131	Ha	131	Sep-45	Aug-89
Opaeula 870	NCDC	7150	Oa	305	Sep-45	Nov-97
Opihihale 2 24.1	NCDC	7166	Ha	415	May-52	Nov-97
Paakea 350	NCDC	7194	Ma	384	Sep-45	Dec-54
Pahala 21	NCDC	7421	Ha	256	Sep-45	Mar-74
Pauwela 490	NCDC	7857	Ma	149	Dec-47	Mar-59
Pepeekeo Makai 144	NCDC	8000	Ha	31	Sep-45	Mar-59
Pri Wahiwa 820.2	NCDC	8172	Oa	214	May-62	Apr-72
Princeville Rch 1117	NCDC	8165	Ka	66	Mar-95	Nov-97
Puako 95.1	NCDC	8186	Ha	15	Mar-66	Dec-71
Puhi 1013	NCDC	8217	Ka	100	Sep-45	Feb-73
Punchbowl Crater 709	NCDC	8316	Oa	110	Dec-46	Mar-51
Puu Manawahua 725.6	NCDC	8500	Oa	510	Sep-75	Nov-97
Puukohola Heiau 98.1	NCDC	8422	Ha	43	Mar-66	Nov-97
Puukolii 457.1	NCDC	8407	Ma	152	Dec-72	Nov-97
Puunene	NCDC	8547	Ma	40	May-82	Nov-97
Puu-O-Hoku Ranch 542.1	NCDC	8549	Mo	213	Sep-45	Nov-54
Sea Mountain 12.15	NCDC	8600	Ha	24	May-78	Nov-97

Table continues on following page.

Appendix Table A1. (continued)

Station Name	Network	ID	Isle.	El. (m)	Start	End
South Kona 2 2.32	NCDC	8652	Ha	720	Dec-72	Mar-85
South Kona 2.31	NCDC	8650	Ha	823	May-85	Nov-97
Tantalus 714	NCDC	8734	Oa	427	Sep-45	Oct-51
Tantalus Mauka	NCDC	8736	Oa	488	Jul-53	Jul-58
Univ Of Hawaii 713	NCDC	8815	Oa	24	Sep-54	Mar-59
Upolu Pt USCG 159.2	NCDC	8830	Ha	19	Apr-52	Nov-88
Upper Wahiwa 874.3	NCDC	8838	Oa	319	Oct-68	Nov-97
US Magnetic Obs	NCDC	8805	Oa	3	Sep-45	May-56
US Magnetic Obs	NCDC	8806	Oa	3	Jun-56	May-58
Waiahi Lower 1054	NCDC	8958	Ka	172	Nov-50	Nov-82
Waialee 896.3	NCDC	9190	Oa	9	Nov-67	Sep-75
Waialua 847	NCDC	9195	Oa	10	Sep-45	Aug-96
Waikiki 717.2	NCDC	9397	Oa	3	Dec-60	Nov-97
Wailuku 386	NCDC	9484	Ma	165	Sep-45	Mar-74
Waimea 947	NCDC	9629	Ka	6	Aug-65	Nov-97
Waimanalo EXP F 795.1	NCDC	9523	Oa	18	Sep-65	Nov-97
Waimea Arb 892.2	NCDC	9603	Oa	12	Aug-79	Nov-97
Waipahu 750	NCDC	9738	Oa	18	Sep-45	Dec-72

Appendix Table A2. Stations used for model development and validation for solar radiation and other variables.

Station Name	Network	Sta. ID	Isle.	El. (m)	Start	End
Barking Sands	NCDC	22501	Ka	4	Dec-68	Oct-97
Barbers Point	NCDC	22514	Oa	7	Sep-45	Nov-97
AeroNet MLO	AeroNet	AN-MLO	BI	3397	Jul-96	Mar-04
AeroNet Lānaʻi	AeroNet	AN-Lanai	La	20	Jul-96	Mar-04
Kalaeloa1	NREL	NK1	Oa	11	Mar-10	Oct-11
Kalaeloa2	NREL	NK2	Oa	11	Mar-10	Oct-11
La Ola1	NREL	NL1	La	382	Jul-09	Dec-11
La Ola2	NREL	NL2	La	382	Jul-09	Dec-11
CFHT	IFA	IFA	Ha	4200	Jan-93	Dec-04
Hakioawa	RAWS	R-1	Ko	366	Oct-01	Dec-11
Hakalau	RAWS	R-2	BI	1951	May-02	Dec-11
Kahuku-Train	RAWS	R-3	Oa	182	Jun-00	Dec-11
Kaneloa	RAWS	R-4	BI	248	Oct-01	Dec-11
Kaupo Gap	RAWS	R-5	Ma	1228	Dec-05	Dec-11
Kii	RAWS	R-6	Oa	2	Aug-02	Dec-11
Kealialalo	RAWS	R-7	Ko	251	Oct-01	Dec-11
Lānaʻi-1	RAWS	R-8	La	387	May-03	Dec-11
Lua Makika	RAWS	R-9	Ko	335	Oct-01	Dec-11
Makua Valley	RAWS	R-12	Oa	158	Jan-00	May-08
Makua Range	RAWS	R-13	Oa	6	Jan-00	Dec-11
Molokai-1	RAWS	R-14	Mo	833	May-03	Jan-05
Moloaa Dairy	RAWS	R-15	Ka	85	May-02	Dec-11
Makua Ridge	RAWS	R-16	Oa	533	Jan-00	Nov-07
PTA Range 17	RAWS	R-17	BI	1734	Apr-04	Dec-11
Pali-2	RAWS	R-18	BI	847	Jan-00	Dec-11
PTA-Kipuka	RAWS	R-19	BI	1641	Jan-00	Nov-09
PTA Portable	RAWS	R-20	BI	1756	Jun-00	Dec-11
PTA WEST	RAWS	R-21	BI	1308	Jan-00	Dec-11
Puʻuanahulu	RAWS	R-22	BI	831	May-05	Dec-11
Puʻu Waʻawaʻa	RAWS	R-23	BI	709	May-03	Dec-11
Schofield	RAWS	R-24	Oa	299	Jan-00	Oct-09
Schofield Fire	RAWS	R-25	Oa	347	Jul-07	May-09
Waianae Valley	RAWS	R-26	Oa	292	May-03	Dec-11
NE Ridge	CAPS	CAPS1	Ma	1884	Jan-98	Jun-03
Koolau Gap	CAPS	CAPS2	Ma	1915	Dec-97	Jun-03
Hanakauhi	CAPS	CAPS3	Ma	2568	Jan-98	Jun-03
Haleakala	CAPS	CAPS5	Ma	2295	Jan-98	Jun-03
South	CAPS	CAPS6	Ma	1337	Jan-98	Jun-03

Table continues on following page.

Appendix Table A2. (continued).

Station Name	Network	Sta. ID	Isle.	El. (m)	Start	End
SW Ridge	CAPS	CAPS7	Ma	1350	Jan-98	Jun-03
North	CAPS	CAPS8	Ma	760	Jan-98	Jun-03
Summit	CAPS	CAPS10	Ma	3030	Nov-97	Jun-03
Puu Pahu	HaleNet	HN106	Ma	1643	Jun-88	Oct-03
Kula Ag	HaleNet	HN119	Ma	965	Jun-88	Dec-11
Auwahi	HaleNet	HN141	Ma	1166	Dec-00	Nov-11
Waikamoi	HaleNet	HN142	Ma	1935	Aug-01	Aug-03
Park HQ	HaleNet	HN151	Ma	2120	Jun-88	Dec-11
Nene Nest	HaleNet	HN152	Ma	2590	Mar-90	Dec-11
Summit	HaleNet	HN153	Ma	2990	Apr-90	Dec-11
Pohaku Palaha	HaleNet	HN161	Ma	2460	Jun-92	Dec-11
Tree Line	HaleNet	HN162	Ma	2195	Jun-92	Dec-11
Horshoe Puʻu	HaleNet	HN163	Ma	1935	Jun-92	Nov-96
Big Bog	HaleNet	HN164	Ma	1650	Jun-92	Nov-11
Thurston	HavoNet	HVT	BI	1202	Feb-05	Feb-10
Olaʻa	HavoNet	HVO	BI	1040	Feb-06	Apr-10
IPIF	EPSCoR	E281	BI	111	May-10	Dec-12
Spencer	EPSCoR	E282	BI	454	Apr-10	Dec-12
Laupahoehoe	EPSCoR	E283	BI	1145	May-09	Dec-12
Hakalau	EPSCoR	E284	BI	1665	Oct-09	Dec-12
KiholoBay	EPSCoR	E285	BI	2	May-10	Dec-12
Palamanui	EPSCoR	E286	BI	297	Oct-09	Dec-12
Mamalahoa	EPSCoR	E287	BI	636	Mar-11	Dec-12
Campbell	Corrosion	CIP	Oa	3	Apr-11	Mar-13
Coconut Island	Corrosion	CI	Oa	1	Jun-11	Mar-13
Ewa Nui	Corrosion	EN	Oa	56	Apr-11	Mar-13
Kahuku	Corrosion	KAH	Oa	1	Apr-11	Mar-13
Kilauea	Corrosion	KIL	BI	568	Feb-11	Mar-13
Lyon	Corrosion	LA	Oa	150	May-11	Mar-13
MCBH	Corrosion	MCBH	Oa	3	Apr-11	Jan-13
Waipahu	Corrosion	WP	Oa	13	Jun-11	Mar-13
Lee	USDA	A415	Ma	454	Jul-11	Nov-12
Windy	USDA	A905	Ma	45	Jul-11	Apr-13

Appendix Table A3. Stations used for model development.

Station ID	$K_{clear\text{-}sky}$	$K_{diffuse}$	C_{solar}	C_{LW}	L_{up}	G	Qb	Qa	Monthly T_{air}	Diurnal T_{air}	Monthly RH	Diurnal RH	SM	Diurnal WS	f_w
172									x						
242									x						
305									x						
340									x						
350									x						
470									x						
507									x						
832									x						
840									x						
995									x						
1004									x						
1008									x						
1122									x						
1125									x						
1303									x						
1339									x						
1484									x						
1492									x		x	x			
1598									x						
1918									x						
1919									x		x	x		x	
1924									x						
1960									x						
2307									x						
2317									x						
2558									x						
2570									x						
2572									x		x				
2679									x						
2751									x						
2896									x						
3077									x						
3078									x						
3099									x						

Table continues on following page.

Appendix Table A3. (continued).

Station ID	$K_{clear\text{-}sky}$	$K_{diffuse}$	C_{solar}	C_{LW}	L_{up}	G	Qb	Qa	Monthly T_{air}	Diurnal T_{air}	Monthly RH	Diurnal RH	SM	Diurnal WS	f_w
3118											x				
3113									x						
3123									x						
3208									x						
3317									x						
3368									x						
3872									x						
3911									x						
3977									x						
3982									x						
4193									x						
4272									x						
4400									x						
4500									x						
4561									x						
4568									x						
4670									x						
4680									x						
4725									x						
4742									x						
4764									x						
4778									x						
4938									x						
5000									x						
5004									x						
5006									x						
5011									x						
5018									x						
5177									x						
5260									x						
5275									x						
5286									x						

Table continues on following page.

Appendix Table A3. (continued).

Station ID	$K_{clear\text{-}sky}$	$K_{diffuse}$	C_{solar}	C_{LW}	L_{up}	G	Qb	Qa	Monthly T_{air}	Diurnal T_{air}	Monthly RH	Diurnal RH	SM	Diurnal WS	f_w
5575									x						
5580									x		x				
5647									x						
5675									x						
5710									x						
5715									x						
5721									x						
5758									x						
5781									x						
5785									x						
5800									x						
5842									x						
5864									x						
6082									x						
6128									x						
6169									x						
6183									x						
6190									x						
6198									x						
6534									x						
6546									x						
6552									x						
6560									x						
6588									x						
6697									x						
6806									x						
6850									x						
7000									x						
7023									x						
7131									x						
7150									x						
7166									x						
7194									x						
7421									x						

Table continues on following page.

Appendix Table A3. (continued).

Station ID	$K_{clear\text{-}sky}$	$K_{diffuse}$	C_{solar}	C_{LW}	L_{up}	G	Qb	Qa	Monthly T_{air}	Diurnal T_{air}	Monthly RH	Diurnal RH	SM	Diurnal WS	f_w
7857									x						
8000									x						
8165									x						
8172									x						
8186									x						
8217									x						
8316									x						
8407									x						
8422									x						
8500									x						
8547									x						
8549									x						
8600									x						
8650									x						
8652									x						
8734									x						
8736									x						
8805									x						
8806									x						
8815									x						
8830									x						
8838									x						
8958									x						
9190									x						
9195									x						
9397									x						
9484									x						
9523									x						
9603									x						
9629									x						
9738									x						
22501											x				
22551											x				
AN-MLO	x														

Table continues on following page.

Appendix Table A3. (continued).

Station ID	$K_{clear\text{-}sky}$	$K_{diffuse}$	C_{solar}	C_{LW}	L_{up}	G	Qb	Qa	Monthly T_{air}	Diurnal T_{air}	Monthly RH	Diurnal RH	SM	Diurnal WS	f_w
AN-Lanai	x														
NK1		x													
NK2															
NL1		x													
NL2															
IFA											x				
R-1															
R-2															
R-3															
R-4															
R-5															
R-6															
R-7															
R-8															
R-9															
R-12															
R-13															
R-14															
R-15															
R-16															
R-17															
R-18															
R-19															
R-20															
R-21															
R-22															
R-23															
R-24															
R-25															
R-26															
CAPS1											x				
CAPS2											x				
CAPS3											x				
CAPS5											x				

Table continues on following page.

Appendix Table A3. (continued).

Station ID	$K_{clear\text{-}sky}$	$K_{diffuse}$	C_{solar}	C_{LW}	L_{up}	G	Qb	Qa	Monthly T_{air}	Diurnal T_{air}	Monthly RH	Diurnal RH	SM	Diurnal WS	f_w
CAPS6											x				
CAPS7											x				
CAPS8											x				
CAPS100											x				
HN106			x								x	x		x	
HN119			x	x	x	x				x	x	x	x	x	
HN141				x		x					x	x		x	
HN142											x	x		x	
HN151			x	x	x	x					x	x	x	x	
HN152			x	x	x	x					x	x	x	x	
HN153			x	x	x	x				x	x	x	x	x	
HN161			x	x	x	x					x	x	x	x	
HN162			x	x		x				x	x	x	x	x	
HN163												x		x	
HN164			x	x	x	x				x	x	x	x	x	
HVT		x			x	x	x	x							
HVO		x			x	x	x	x							
E281															
E282															
E283					x										
E284															
E285															
E286					x										
E287					x										
E288															
CIP															x
CI															x
EN															x
KAH															x
KIL															x
LA															x
MCBH															x

Table continues on following page.

Appendix Table A3. (continued).

Station ID	$K_{clear\text{-}sky}$	$K_{diffuse}$	C_{solar}	C_{LW}	L_{up}	G	Qb	Qa	Monthly T_{air}	Diurnal T_{air}	Monthly RH	Diurnal RH	SM	Diurnal WS	f_w
WP															x
A415															
A905															
Lit1[1]							x								
Lit2[2]							x								
Lit3[3]							x								
Lit4[4]								x							
Lit5[5]							x	x							
Lit6[6]							x	x							
Lit7[7]							x	x							

[1]Meyers and Hollinger (2004) maize site; [2]Meyers and Hollinger (2004) soybean site; [3]Michiles and Gielow (2008); [4]Ohkubo et al. (2008); [5]Samson and Lemeur (2001); [6]Silberstein et al. (2001); [7]Wang and Zhang (2011).

Appendix Table A4. Stations used for validation.

Station ID	$K_{clear\text{-}sky}$	$K_{diffuse}$	K_{global}	*Albedo*	L_{down}	L_{up}	R_{net}	G	T_{air}	RH	WS	SM	LE
NK1	x	x	x						x	x	x		
NK2	x		x										
NL1	x	x	x						x	x	x		
NL2	x		x										
R-1			x						x	x	x		
R-2			x						x	x	x		
R-3			x						x	x	x		
R-4			x						x	x	x		
R-5			x						x	x	x		
R-6			x						x	x	x		
R-7			x						x	x	x		
R-8			x						x	x	x		
R-9			x						x	x	x		
R-12			x						x	x	x		
R-13			x						x	x	x		
R-14			x						x	x	x		
R-15			x						x	x	x		
R-16			x						x	x	x		
R-17			x						x	x	x		
R-18			x						x	x	x		
R-19			x						x	x	x		
R-20			x						x	x	x		
R-21			x						x	x	x		
R-22			x						x	x	x		
R-23			x						x	x	x		
R-24			x						x	x	x		
R-25			x						x	x	x		
R-26			x						x	x	x		
HN106	x								x				
HN119				x									
HN141			x	x		x	x		x				
HN142	x		x				x		x				
HN151	x			x					x				
HN152	x			x					x				

Table continues on following page.

Appendix Table A4. (continued).

Station ID	$K_{clear\text{-}sky}$	$K_{diffuse}$	K_{global}	$Albedo$	L_{down}	L_{up}	R_{net}	G	T_{air}	RH	WS	SM	LE
HN153				x									
HN161	x			x					x				
HN162	x			x		x							
HN163			x				x		x				
HN164				x									
HVT				x	x				x	x	x	x	x
HVO	x			x	x				x	x	x	x	x
E281			x						x	x	x	x	
E282			x					x	x	x	x	x	
E283			x	x	x		x	x	x	x	x	x	
E284			x					x	x	x	x	x	
E285			x						x	x	x		
E286			x	x	x		x		x	x	x	x	
E287			x	x	x		x		x	x	x	x	
A415													x
A905													x

Appendix Table A5. Landcover classification used in all analysis except albedo, adapted from LANDFIRE 2008 existing vegetation classes (Comer et al. 2003; http://landfire.gov).

LC Code	Landcover Type
1	Developed-Open Space
2	Developed-Low Intensity
3	Developed-Medium Intensity
4	Developed-High Intensity
5	Barren
6	Mixed Agriculture*
7	Hawaiʻi Bog
8	Hawaiʻi Lowland Rainforest
9	Hawaiʻi Montane Cloud Forest
10	Hawaiʻi Montane Rainforest
11	Hawaiʻi Wet Cliff and Ridge Crest Shrubland
12	Hawaiʻi Lowland Dry Forest
13	Hawaiʻi Lowland Mesic Forest
14	Hawaiʻi Montane-Subalpine Dry Forest and Woodland
15	Hawaiʻi Montane-Subalpine Mesic Forest
16	Hawaiʻi Lowland Dry Shrubland
17	Hawaiʻi Lowland Mesic Shrubland
18	Hawaiʻi Lowland Dry Grassland
19	Hawaiʻi Lowland Mesic Grassland
20	Hawaiʻi Montane-Subalpine Dry Shrubland
21	Hawaiʻi Montane-Subalpine Dry Grassland
22	Hawaiʻi Montane-Subalpine Mesic Grassland
23	Hawaiʻi Alpine Dwarf-Shrubland
24	Hawaiʻi Dry Cliff
25	Hawaiʻi Dry Coastal Strand
26	Hawaiʻi Wet-Mesic Coastal Strand
27	Hawaiʻi Subalpine Mesic Shrubland
28	Hawaiian Introduced Wetland Vegetation-Tree
29	Hawaiian Introduced Wetland Vegetation-Shrub
30	Hawaiian Introduced Wetland Vegetation-Herbaceous
31	Hawaiian Introduced Dry Forest
32	Hawaiian Introduced Wet-Mesic Forest
33	Hawaiian Introduced Deciduous Shrubland
34	Hawaiian Introduced Perennial Grassland
35	Hawaiian Introduced Evergreen Shrubland
36	Introduced Coastal Wetland Vegetation - Tree
37	Introduced Coastal Wetland Vegetation - Shrub

Table continues on next page.

Appendix Table A5. (continued).

LC Code	Landcover Type
38	Introduced Coastal Wetland Vegetation - Herbaceous
39	Hawaiian Managed Tree Plantation
40	Open Water
41	Coastal Kiawe**
42	Agriculture – Sugarcane*
43	Agriculture – Pineapple*
44	Agriculture - Macadamia Nut*
45	Agriculture – Coffee*
46	Agriculture – Taro*

*Agricultural areas in the LANDFIRE classification were subdivided into crop types (indicated below with an asterisk) based on visual examination of GoogleEarth imagery. **Coastal kiawe was defined as Hawaiian Introduced Dry Forest areas with elevations of 12 m above sea level or lower.

Appendix Table A6. HIGAP land cover classes (Gon, III et al. 1999; http://gis1.usgs.gov/csas/gap/viewer/land_cover/Map.aspx).

Code	HIGAP Land Cover Category	Code	HIGAP Land Cover Category
0	Ocean	19	Native Wet Forest and Shrubland
1	Mixed Native-Alien Forest	20	ʻŌhiʻa Forest
2	Mixed Native-Alien Shrubs and Grasses	21	Olopua-Lama Forest
3	Native Coastal Vegetation	22	Open Koa-Māmane Forest
4	Deschampsia Grassland	23	Open Koa-ʻŌhiʻa Forest
5	ʻAʻaliʻi Shrubland	24	Open ʻŌhiʻa Forest
6	Bog Vegetation	25	Water
7	Native Dry Cliff Vegetation	26	Wetland Vegetation
8	Native Shrubland / Sparse ʻŌhiʻa (native shrubs)	27	Agriculture
9	Native Wet Cliff Vegetation	28	High Intensity Developed
10	Open Maʻo Shrubland	29	Low Intensity Developed
11	Uluhe Shrubland	30	Alien Grassland
12	Closed Hala Forest	31	Alien Shrubland
13	Closed Koa-ʻŌhiʻa Forest	32	Alien Forest
14	Closed ʻŌhiʻa Forest	33	Kiawe Forest and Shrubland
15	Closed *Pouteria* Forest	34	Uncharacterized Forest
16	Koa Forest (native shrubs)	35	Uncharacterized Open-Sparse Vegetation
17	Māmane / Naio / Native Trees	36	Uncharacterized Shrubland
18	Native Mesic to Dry Forest and Shrubland	37	Very Sparse Vegetation to Unvegetated

Appendix Table A7. Mean periods of record of data used to develop and validate models.

Category	Variable	Model development			Validation			External Reference
		Start	End	Mid	Start	End	Mid	
Solar Radiation	$K_{clear-sky}$	See constituent variables w, AOD, a, and $K_{diffuse}$.			Mar-03	Mar-10	Sep-06	
	w	Nov-04	Feb-07	Dec-05	See validation for resultant variable $K_{clear-sky}$.			Longman et al. (2012)
	AOD and a	Jul-95	Aug-07	Jul-01	See validation for resultant variable $K_{clear-sky}$.			Longman et al. (2012)
	$K_{diffuse}$	Sep-07	Dec-10	May-09	May-09	Dec-12	Feb-11	
	CF	Jan-01	Dec-11	Jun-06	See validation for resultant variable K_{global}.			
	C_{solar}	Jul-98	Nov-10	Sep-04	See validation for resultant variable K_{global}.			
	K_{global}	See constituent variables $K_{clear-sky}$, $K_{diffuse}$, CF, and C_{solar}.			Nov-03	Nov-10	May-07	
Net Radiation	$Albedo$	Jan-00	Dec-04	Jun-02	Mar-03	Nov-11	Jul-07	
	C_{LW}	Jan-11	Dec-12	Dec-11	See validation for resultant variable L_{down}.			
	L_{down}	See constituent variables w, T_{air}, CF, and $Cloud\text{-}L_{down}$.			Apr-08	Oct-11	Jan-10	
	L_{up}	Oct-03	Nov-11	Oct-07	Jan-00	Nov-11	Dec-05	
	R_{net}	See constituent variables K_{global}, $Albedo$, L_{down}, and L_{up}.			Jan-04	Jul-08	Apr-06	

Table continues on the following page.

Appendix Table A7. (continued)

Category	Variable	Model development			Validation			External Reference
		Start	End	Mid	Start	End	Mid	
Heat Storage	G	Feb-01	Jul-11	May-06	Oct-09	Dec-12	May-11	
	Q_b	Aug-01	Jan-03	May-02	Insufficient data available.			
	Q_a	Apr-02	Apr-04	Apr-03	Insufficient data available			
Air Temperature	Monthly T_{air}	Mar-57	Jan-81	Feb-69	See validation for resultant variable T_{air}.			
	Diurnal T_{air}	Dec-90	Dec-05	Jun-98	See validation for resultant variable T_{air}.			
	T_{air}	See constituent variables Monthly T_{air} and Diurnal T_{air}.			Jan-03	Sep-10	Nov-06	
Relative Humidity	Monthly RH	Feb-85	Jan-03	Jan-94	See validation for resultant variable RH_{air}.			
	Diurnal RH	Jun-86	Feb-04	Apr-95	See validation for resultant variable RH_{air}.			
	RH	See constituent variables Monthly RH_{air} and Diurnal RH_{air}.			Feb-04	May-11	Oct-07	
Wind Speed	Mean Ann. WS	See external reference.			See validation for resultant variable WS.			AWS Truewind (2004)
	Diurnal WS	Aug-99	May-09	Jun-04	See validation for resultant variable WS.			
	WS	See constituent variables Mean Annual WS and Diurnal WS.			Feb-04	May-11	Oct-07	

Table continues on the following page.

Appendix Table A7. (continued)

Category	Variable	Model development			Validation			External Reference
		Start	End	Mid	Start	End	Mid	
Land Characteristics	Land Cover	2008	2008	2008	NA	NA	NA	http://landfire.gov
	Agric. LC	Jan-13	Jan-13	Jan-13	NA	NA	NA	http://www.google.com/earth
	Veg. Height	2008	2008	2008	NA	NA	NA	http://landfire.gov
	LAI	Jul-02	Dec-12	Sep-07	Insufficient data available.			
	f_c	Jul-02	Mar-09	Oct-05	Insufficient data available.			
Water storage	f_w	Apr-11	Feb-13	Mar-12	Insufficient data available.			
	SM	Jan-00	Nov-11	Dec-05	Nov-07	Mar-12	Jan-10	
Evapotranspiration	*LE*	See constituent variables (all of the above).			Jul-08	Aug-11	Jan-10	

$K_{clear\text{-}sky}$ = clear sky solar radiation; *w* = precipitable water; *AOD* = aerosol optical depth; *a* is the Angström exponent; $K_{diffuse}$ = diffuse solar radiation; *CF* = cloud frequency; C_{solar} = the ratio of solar radiation to clear-sky solar radiation estimated as a function of *CF*; K_{global} = global solar radiation; *Albedo* = the proportion of solar radiation reflected by the surface; C_{LW} = the ratio of downward longwave radiation to clear-sky downward longwave radiation estimated as a function of *CF*; L_{down} = downward longwave radiation; L_{up} = upward longwave radiation; R_{net} = net radition; *G* = soil heat flux; Q_b = energy storage in aboveground biomass; Q_a = energy storage in air layer below reference height; T_{air} = air temperature;*RH* = mean monthly relative humidity; Diurnal *RH* = relative humidity; *WS* = wind speed; f_c = vegetation cover fraction f_w = canopy wetness fraction; *SM* = soil moisture; *LE* = latent energy flux.

Appendix Table A8. Maximum stomatal conductance of each land cover class.

Land Cover Classification (EVT Name)	g_{s_max} (m s^{-1})	Reference Species
Open Water	NA[a]	NA[1]
Developed-Open Space	0.0100[b]	*Cynodon dactylon*[2]
Developed-Low Intensity	0.0100[b]	*Cynodon dactylon*[2]
Developed-Medium Intensity	0.0100[b]	*Cynodon dactylon*[2]
Developed-High Intensity	0.0100[b]	*Cynodon dactylon*[2]
Barren	0.0029[b]	*Metrosideros polymorpha*[3]
Bog	0.0055[b]	*Metrosideros polymorpha*[4]
Lowland Rainforest	0.0031[b]	*Coprosma grandifolia*[5]
Montane Cloud Forest	0.0030[b]	*Metrosideros polymorpha*[6]
Montane Rainforest	0.0038[b]	*Metrosideros polymorpha*[7]
Wet Cliff and Ridge Crest Shrubland	0.0038[b]	*Metrosideros polymorpha*[7]
Lowland Dry Forest	0.0029[b]	*Metrosideros polymorpha*[3]
Lowland Mesic Forest	0.0028[b]	*Metrosideros polymorpha*[8], *Acacia koa*[9], *Diopyros sandwicensis*[10]
Montane-Subalpine Dry Forest/Woodland	0.0027[b]	*Metrosideros polymorpha*[3], *Acacia koa*[9]
Montane-Subalpine Mesic Forest	0.0018[b]	*Metrosideros polymorpha*[6]
Lowland Dry Shrubland	0.0029[b]	*Metrosideros polymorpha*[3]
Lowland Mesic Shrubland	0.0034[b]	*Metrosideros polymorpha*[8]
Lowland Dry Grassland	0.0083[b]	*Heteropogon contortus*[11]
Lowland Mesic Grassland	0.0083[b]	*Heteropogon contortus*[11]
Montane-Subalpine Dry Shrubland	0.0018[b]	*Metrosideros polymorpha*[6]
Montane-Subalpine Dry Grassland	0.0048[b]	*Deschampsia australis*[e]
Montane-Subalpine Mesic Grassland	0.0048[b]	*Deschampsia australis*[e]
Alpine Dwarf-Shrubland	0.0018[b]	*Metrosideros polymorpha*[6]
Dry Cliff	0.0029[b]	*Metrosideros polymorpha*[3]
Dry Coastal Strand	0.0029[b]	*Metrosideros polymorpha*[3]
Wet-Mesic Coastal Strand	0.0038[b]	*Metrosideros polymorpha*[7]
Subalpine Mesic Shrubland	0.0018[b]	*Metrosideros polymorpha*[6]
Alpine Bedrock and Scree	0.0030[b]	*Metrosideros polymorpha*[6]
Dry-Site Lava Flow	0.0029[b]	*Metrosideros polymorpha*[3]
Introduced Wetland Vegetation-Tree	0.0093[b]	*Rhizophora mangle*[13]
Introduced Wetland Vegetation-Shrub	0.0093[b]	*Rhizophora mangle*[13]
Introduced Wetland Vegetation-Herb.	0.0113[b]	*Typha latifolia*[14]
Introduced Dry Forest	0.0068[b]	*Prosopis palida*[f,15]
Introduced Wet-Mesic Forest	0.0066[b]	*Psidium cattleianum*[7]
Introduced Decid. Shrubland (wet-mesic)	0.0066[b]	*Psidium cattleianum*[7]
Introduced Deciduous Shrubland (dry)	0.0095[b]	*Leucaena leucocephala*[16]
Introduced Perennial Grassland	0.0048[b]	*Pennisetum setaceum*[17]

Table continues on the following page.

Appendix Table A8. (continued).

Land Cover Classification (EVT Name)	g_{s_max} (m s^{-1})	Reference Species
Introduced Evergreen Shrubland	0.0092 [b]	*Psidium cattleianum; Schinus terebinthifolius*[18]
Introduced Coastal Wetland Veg. - Tree	0.0093 [b]	*Rhizophora mangle*[13]
Introduced Coastal Wetland Veg. - Shrub	0.0093 [b]	*Rhizophora mangle*[13]
Introduced Coastal Wetland Veg. - Herb.	0.0113 [b]	*Typha latifolia*[14]
Managed Tree Plantation	0.0057 [b]	*Eucalyptus spp.* [g, 19]
Sugarcane	0.0071[c]	*Saccharum spp. hybrid*[20]
Pineapple	0.0003[d]	*A. comosus*[21]
Macadamia	0.0062 [b]	*M. integrifolia*[22]
Coffee	0.0048 [b]	*C. arabica*[23]
Taro	0.0167 [b]	*C. esculenta*[24]
Mixed Agriculture	0.0084 [b]	Various[h, 25]

[a] g_{c_max} = 0.1000 m s^{-1}; [b] g_{c_max} from Eq. (51) (Kelliher et al. 1995, their eq. 6, with Q_{a50} set to 100 and c_Q set to 0.6); [c] g_{c_max} = 0.0200 m s^{-1}; [d] $g_{c\_max} = g_{s\_max} * LAI$; [e]substitute for *Deschampsia australis*; [f]substitute for *Prosopis palida*; [g]average of *Eucalyptus camaldulensis*, *Eucalyptus leucoxylon*, and *Eucalyptus platypus*; [h]average of other listed agricultural species and banana (*Musa acuminata*), papaya (*Carica papaya*), and maize (*Zea mays*). Stomatal conductance references: [1]Open water surface diffusion (La Mer and Healy 1965; van de Griend and Owe 1994); [2]Carmo-Silva et al. (2008); [3]S. Cordell (pers. comm. 2013); [4]adapted from Santiago et al. (2000); [5]McAlpine et al. (2008); [6]Gotsch et al. (in review); [7]Y. Miyazawa (pers. comm. 2013); [8]average of wet (Y. Miyazawa, pers. comm. 2013), and dry (S. Cordell, pers. comm. 2013) values; [9]Pasquet-Kok et al. (2010); [10]Cabin et al. (2000); [11]Williams and Baruch (2000); [12]Pugnaire et al. (1996); [13]Kraus and Allen (2003); [14]Li et al. (2004); [15]Nilsen et al. (1983); [16]Huang et al. (1985); [17]Williams et al. (1995); [18]average of *P. cattleianum* (Y. Miyazawa, pers. comm. 2013), and *S. terebinthifolius* (Ewe et al. 2003); [19]average of three eucalyptus species (White et al. 2000); [20]Meinzer and Grantz (1989); [21]Neals et al. (1980); [22]Lloyd (1991); [23]Gutiérrez et al. (1994); [24]Sims and Pearcy (1989); [25]average of sugarcane (Meinzer and Grantz 1989), pineapple (Neals et al. 1980), macadamia (Lloyd 1991), coffee (Gutiérrez et al. 1994), taro (Sims and Pearcy 1989), banana (g_{s_max} = 0.0159 m s^{-1}; Robinson and Bower 1988), papaya (g_{s_max} = 0.0112 m s^{-1}; Marler and Mickelbart 1998), and maize (g_{s_max} = 0.0051 m s^{-1}; Tuberosa et al. 1994).

Appendix Table A9. Statistical relationships for mean annual values of forcing variables and *PET* vs. mean annual latent energy flux for each land cover type.

LC Type	Forcing	Slope	Intercept	r^2	RSE	P value	N
1. Developed-Open Space							
	R_{net}	0.427	15.416	0.227	14.608	0.0000	7830
	T	1.232	45.714	0.025	16.406	0.0000	7830
	RH	-0.301	95.383	0.009	16.539	0.0000	7830
	U	2.466	65.920	0.022	16.434	0.0000	7830
	LAI	15.845	38.961	0.574	10.847	0.0000	7830
	f_c	52.725	33.921	0.340	13.504	0.0000	7830
	h	1.224	69.377	0.057	16.135	0.0000	7830
	θ	94.493	20.530	0.169	15.152	0.0000	7830
	f_w	-20.291	78.361	0.019	16.456	0.0000	7830
	$PET_{Penman\text{-}Monteith}$	0.007	55.041	0.119	15.593	0.0000	7830
	ET_0	0.005	62.269	0.027	16.395	0.0000	7830
	$PET_{Priestley\text{-}Taylor}$	0.041	7.662	0.295	13.951	0.0000	7830
2. Developed-Low Intensity							
	R_{net}	0.365	5.764	0.256	10.895	0.0000	6463
	T	0.798	35.467	0.015	12.539	0.0000	6463
	RH	-0.227	70.116	0.008	12.582	0.0000	6463
	U	4.605	43.973	0.060	12.244	0.0000	6463
	LAI	12.127	28.430	0.662	7.344	0.0000	6463
	f_c	45.053	19.838	0.389	9.870	0.0000	6463
	h	-0.196	53.930	0.000	12.630	0.2261	6463
	θ	72.163	12.811	0.170	11.507	0.0000	6463
	f_w	-16.356	57.458	0.018	12.519	0.0000	6463
	$PET_{Penman\text{-}Monteith}$	0.003	40.392	0.072	12.166	0.0000	6463
	ET_0	0.006	41.466	0.040	12.373	0.0000	6463
	$PET_{Priestley\text{-}Taylor}$	0.032	3.521	0.288	10.661	0.0000	6463
3. Developed-Medium Intensity							
	R_{net}	0.226	-4.773	0.281	5.706	0.0000	2949
	T	-0.804	42.663	0.014	6.683	0.0000	2949
	RH	0.169	11.938	0.007	6.706	0.0000	2949
	U	2.479	18.554	0.043	6.584	0.0000	2949
	LAI	6.426	16.350	0.650	3.983	0.0000	2949
	f_c	14.775	14.964	0.121	6.310	0.0000	2949
	h	-0.137	24.747	0.002	6.724	0.0271	2949
	θ	22.009	12.508	0.019	6.666	0.0000	2949
	f_w	8.191	22.362	0.006	6.709	0.0000	2949
	$PET_{Penman\text{-}Monteith}$	0.000	24.610	0.000	6.729	0.5135	2949
	ET_0	0.000	23.543	0.000	6.729	0.4991	2949
	$PET_{Priestley\text{-}Taylor}$	0.017	-2.421	0.203	6.008	0.0000	2949

Table continues on next page.

Appendix Table A9. (continued).

LC Type	Forcing variable	Slope	Intercept	r^2	RSE	P value	N
4. Developed-High Intensity							
	R_{net}	0.230	-21.111	0.243	5.563	0.0000	2024
	T	0.673	-6.651	0.006	6.374	0.0008	2024
	RH	-0.221	24.801	0.008	6.365	0.0000	2024
	U	2.067	3.219	0.034	6.282	0.0000	2024
	LAI	2.431	7.109	0.090	6.099	0.0000	2024
	f_c	-6.719	12.418	0.031	6.292	0.0000	2024
	h	-0.860	30.087	0.534	4.365	0.0000	2024
	θ	8.299	4.702	0.003	6.382	0.0131	2024
	f_w	-9.728	10.986	0.006	6.373	0.0006	2024
	$PET_{Penman\text{-}Monteith}$	-0.004	30.906	0.191	5.750	0.0000	2024
	ET_0	0.003	1.675	0.015	6.343	0.0000	2024
	$PET_{Priestley\text{-}Taylor}$	0.009	-5.602	0.047	6.240	0.0000	2024
5. Barren							
	R_{net}	-0.031	36.734	0.002	13.358	0.0000	50792
	T	0.344	27.348	0.029	13.177	0.0000	50792
	RH	0.329	10.867	0.170	12.186	0.0000	50792
	U	2.794	23.364	0.048	13.051	0.0000	50792
	LAI	9.243	30.572	0.085	12.793	0.0000	50792
	f_c	28.776	28.121	0.108	12.628	0.0000	50792
	h	1.730	32.047	0.001	13.368	0.0000	50792
	θ	112.916	-11.710	0.874	4.748	0.0000	50792
	f_w	28.158	26.566	0.124	12.519	0.0000	50792
	$PET_{Penman\text{-}Monteith}$	-0.003	37.620	0.006	13.334	0.0000	50792
	ET_0	-0.007	42.744	0.063	12.948	0.0000	50792
	$PET_{Priestley\text{-}Taylor}$	0.006	22.782	0.005	13.338	0.0000	50792
6. Mixed Agriculture							
	R_{net}	0.517	33.351	0.210	13.031	0.0000	4871
	T	4.910	-9.640	0.178	13.293	0.0000	4871
	RH	-1.693	226.510	0.204	13.077	0.0000	4871
	U	7.672	81.105	0.143	13.573	0.0000	4871
	LAI	15.093	62.624	0.411	11.256	0.0000	4871
	f_c	39.490	68.258	0.146	13.546	0.0000	4871
	h	0.907	98.550	0.016	14.542	0.0000	4871
	θ	18.368	85.589	0.025	14.480	0.0000	4871
	f_w	-88.774	122.997	0.226	12.899	0.0000	4871
	$PET_{Penman\text{-}Monteith}$	0.012	68.967	0.265	12.569	0.0000	4871
	ET_0	0.019	59.560	0.260	12.610	0.0000	4871
	$PET_{Priestley\text{-}Taylor}$	0.053	17.239	0.330	11.997	0.0000	4871

Table continues on next page.

Appendix Table A9. (continued).

LC Type	Forcing variable	Slope	Intercept	r^2	RSE	P value	N
7. Hawai'i Bog							
	R_{net}	0.864	-18.800	0.660	7.135	0.0000	35
	T	2.903	27.029	0.464	8.955	0.0000	35
	RH	2.359	-129.184	0.218	10.817	0.0046	35
	U	3.131	55.411	0.031	12.045	0.3123	35
	LAI	10.752	52.452	0.440	9.158	0.0000	35
	f_c	-2.680	67.806	0.003	12.218	0.7616	35
	h	2.475	50.671	0.500	8.648	0.0000	35
	θ			0.000			
	f_w	91.275	25.659	0.206	10.902	0.0062	35
	$PET_{Penman\text{-}Monteith}$	0.020	24.334	0.560	8.114	0.0000	35
	ET_0	0.059	17.932	0.533	8.365	0.0000	35
	$PET_{Priestley\text{-}Taylor}$	0.064	-1.999	0.762	5.969	0.0000	35
8. Hawai'i Lowland Rainforest							
	R_{net}	0.454	3.464	0.529	6.086	0.0000	38978
	T	1.203	35.926	0.076	8.528	0.0000	38978
	RH	-0.601	107.984	0.067	8.567	0.0000	38978
	U	8.343	40.714	0.561	5.877	0.0000	38978
	LAI	8.464	37.966	0.215	7.858	0.0000	38978
	f_c	29.848	31.361	0.086	8.481	0.0000	38978
	h	0.512	52.981	0.024	8.765	0.0000	38978
	θ	30.550	36.911	0.094	8.446	0.0000	38978
	f_w	-25.796	69.749	0.074	8.537	0.0000	38978
	$PET_{Penman\text{-}Monteith}$	0.012	32.378	0.571	5.813	0.0000	38978
	ET_0	0.009	47.320	0.117	8.336	0.0000	38978
	$PET_{Priestley\text{-}Taylor}$	0.034	11.213	0.484	6.371	0.0000	38978
9. Hawai'i Montane Cloud Forest							
	R_{net}	0.376	19.384	0.453	5.145	0.0000	469
	T	0.406	54.578	0.012	6.911	0.0163	469
	RH	0.106	51.345	0.001	6.950	0.4751	469
	U	5.377	42.261	0.325	5.713	0.0000	469
	LAI	4.693	53.759	0.061	6.738	0.0000	469
	f_c	-10.700	66.206	0.094	6.618	0.0000	469
	h	1.787	46.291	0.377	5.489	0.0000	469
	θ	-11.790	68.800	0.021	6.880	0.0016	469
	f_w	3.275	58.676	0.001	6.951	0.5631	469
	$PET_{Penman\text{-}Monteith}$	0.013	31.242	0.566	4.582	0.0000	469
	ET_0	0.024	40.497	0.058	6.749	0.0000	469
	$PET_{Priestley\text{-}Taylor}$	0.024	31.641	0.354	5.591	0.0000	469

Table continues on next page.

Appendix Table A9. (continued).

LC Type	Forcing variable	Slope	Intercept	r^2	RSE	P value	N
10. Hawai'i Montane Rainforest							
10	R_{net}	0.461	0.623	0.474	5.672	0.0000	12455
	T	-0.653	65.494	0.008	7.790	0.0000	12455
	RH	0.140	44.930	0.002	7.814	0.0000	12455
	U	6.858	42.927	0.572	5.116	0.0000	12455
	LAI	8.825	41.030	0.081	7.497	0.0000	12455
	f_c	36.004	29.677	0.137	7.265	0.0000	12455
	h	1.284	44.217	0.028	7.712	0.0000	12455
	θ	51.550	23.440	0.326	6.422	0.0000	12455
	f_w	6.407	53.642	0.003	7.812	0.0000	12455
	$PET_{Penman-Monteith}$	0.018	22.183	0.592	4.994	0.0000	12455
	ET_0	-0.029	83.877	0.057	7.598	0.0000	12455
	$PET_{Priestley-Taylor}$	0.043	-1.160	0.468	5.704	0.0000	12455
11. Hawai'i Wet Cliff and Ridge Crest							
	R_{net}	0.369	12.500	0.355	7.503	0.0000	1667
	T	-0.086	55.368	0.001	9.341	0.3599	1667
	RH	-0.067	59.486	0.000	9.342	0.4095	1667
	U	6.337	38.971	0.354	7.511	0.0000	1667
	LAI	7.496	41.530	0.308	7.775	0.0000	1667
	f_c	-0.264	54.056	0.000	9.344	0.9004	1667
	h	1.996	42.513	0.458	6.879	0.0000	1667
	θ	-17.839	65.449	0.026	9.222	0.0000	1667
	f_w	-0.517	54.083	0.000	9.344	0.8692	1667
	$PET_{Penman-Monteith}$	0.015	23.934	0.571	6.120	0.0000	1667
	ET_0	0.002	51.437	0.005	9.321	0.0043	1667
	$PET_{Priestley-Taylor}$	0.026	20.709	0.295	7.843	0.0000	1667
12. Hawai'i Lowland Dry Forest							
	R_{net}	0.551	-25.284	0.392	10.019	0.0000	3016
	T	0.383	35.718	0.002	12.842	0.0165	3016
	RH	-0.233	62.701	0.004	12.827	0.0003	3016
	U	8.534	24.682	0.407	9.900	0.0000	3016
	LAI	10.323	31.568	0.286	10.859	0.0000	3016
	f_c	45.853	16.490	0.284	10.878	0.0000	3016
	h	2.154	30.683	0.225	11.315	0.0000	3016
	θ	127.550	-11.587	0.732	6.651	0.0000	3016
	f_w	-10.881	48.151	0.006	12.816	0.0000	3016
	$PET_{Penman-Monteith}$	0.008	22.780	0.305	10.713	0.0000	3016
	ET_0	0.007	33.712	0.033	12.643	0.0000	3016
	$PET_{Priestley-Taylor}$	0.042	-19.137	0.361	10.277	0.0000	3016

Table continues on next page.

Appendix Table A9. (continued).

LC Type	Forcing variable	Slope	Intercept	r^2	RSE	P value	N
13. Hawai'i Lowland Mesic Forest							
	R_{net}	0.484	-7.826	0.500	7.905	0.0000	10986
	T	0.044	52.403	0.000	11.177	0.4688	10986
	RH	-0.383	84.707	0.023	11.046	0.0000	10986
	U	9.304	33.280	0.560	7.413	0.0000	10986
	LAI	5.682	40.376	0.136	10.389	0.0000	10986
	f_c	22.811	34.859	0.077	10.740	0.0000	10986
	h	1.083	45.544	0.099	10.610	0.0000	10986
	θ	100.101	0.351	0.459	8.221	0.0000	10986
	f_w	-15.242	59.811	0.021	11.059	0.0000	10986
	$PET_{Penman\text{-}Monteith}$	0.010	28.051	0.457	8.238	0.0000	10986
	ET_0	0.006	44.684	0.047	10.910	0.0000	10986
	$PET_{Priestley\text{-}Taylor}$	0.038	-3.334	0.462	8.195	0.0000	10986
14. Hawai'i Montane-Subalpine Dry							
	R_{net}	0.007	29.169	0.000	6.202	0.2256	6388
	T	0.607	22.752	0.045	6.062	0.0000	6388
	RH	0.243	12.051	0.090	5.916	0.0000	6388
	U	2.594	26.183	0.036	6.089	0.0000	6388
	LAI	16.825	24.414	0.237	5.419	0.0000	6388
	f_c	33.320	18.799	0.241	5.403	0.0000	6388
	h	0.683	26.702	0.065	5.997	0.0000	6388
	θ	99.910	-4.952	0.706	3.364	0.0000	6388
	f_w	11.449	26.920	0.059	6.017	0.0000	6388
	$PET_{Penman\text{-}Monteith}$	0.003	23.694	0.033	6.099	0.0000	6388
	ET_0	-0.014	45.808	0.074	5.968	0.0000	6388
	$PET_{Priestley\text{-}Taylor}$	0.004	23.585	0.009	6.176	0.0000	6388
15. Hawai'i Montane-Subalpine Mesic							
	R_{net}	0.519	-20.553	0.690	5.311	0.0000	10336
	T	0.190	41.526	0.001	9.530	0.0005	10336
	RH	0.200	28.171	0.009	9.494	0.0000	10336
	U	10.944	27.679	0.541	6.459	0.0000	10336
	LAI	7.904	36.179	0.103	9.033	0.0000	10336
	f_c	26.745	28.134	0.092	9.084	0.0000	10336
	h	0.848	37.691	0.048	9.305	0.0000	10336
	θ	89.785	0.628	0.697	5.251	0.0000	10336
	f_w	9.442	40.543	0.009	9.490	0.0000	10336
	$PET_{Penman\text{-}Monteith}$	0.022	0.710	0.550	6.400	0.0000	10336
	ET_0	0.028	15.866	0.036	9.365	0.0000	10336
	$PET_{Priestley\text{-}Taylor}$	0.051	-25.877	0.755	4.718	0.0000	10336

Table continues on next page.

Appendix Table A9. (continued).

LC Type	Forcing variable	Slope	Intercept	r^2	RSE	P value	N
16. Hawai'i Lowland Dry Shrubland							
	R_{net}	0.528	-30.877	0.471	8.873	0.0000	1793
	T	0.871	19.415	0.053	11.870	0.0000	1793
	RH	0.286	11.931	0.013	12.115	0.0000	1793
	U	7.507	19.585	0.344	9.878	0.0000	1793
	LAI	14.917	26.154	0.378	9.621	0.0000	1793
	f_c	54.937	8.854	0.360	9.758	0.0000	1793
	h	2.303	27.972	0.139	11.316	0.0000	1793
	θ	132.660	-15.529	0.803	5.417	0.0000	1793
	f_w	12.669	29.948	0.013	12.118	0.0000	1793
	$PET_{Penman\text{-}Monteith}$	0.011	12.383	0.383	9.583	0.0000	1793
	ET_0	0.007	25.987	0.045	11.918	0.0000	1793
	$PET_{Priestley\text{-}Taylor}$	0.038	-19.721	0.431	9.202	0.0000	1793
17. Hawai'i Lowland Mesic Shrubland							
	R_{net}	0.531	-13.699	0.488	8.256	0.0000	776
	T	-0.012	53.879	0.000	11.534	0.9608	776
	RH	-0.455	91.787	0.020	11.418	0.0001	776
	U	4.979	40.306	0.248	10.002	0.0000	776
	LAI	6.404	45.159	0.232	10.111	0.0000	776
	f_c	26.858	34.951	0.121	10.813	0.0000	776
	h	1.349	47.507	0.146	10.660	0.0000	776
	θ	46.876	26.885	0.185	10.414	0.0000	776
	f_w	-16.306	61.279	0.015	11.444	0.0005	776
	$PET_{Penman\text{-}Monteith}$	0.013	24.862	0.481	8.310	0.0000	776
	ET_0	0.006	46.355	0.027	11.376	0.0000	776
	$PET_{Priestley\text{-}Taylor}$	0.040	-5.823	0.437	8.656	0.0000	776
18. Hawai'i Lowland Dry Grassland							
	R_{net}	0.046	52.902	0.001	16.683	0.5976	316
	T	-5.162	166.633	0.381	13.130	0.0000	316
	RH	1.581	-66.699	0.335	13.610	0.0000	316
	U	6.800	36.224	0.111	15.735	0.0000	316
	LAI	1.331	58.139	0.002	16.676	0.4525	316
	f_c	-14.108	63.704	0.041	16.348	0.0003	316
	h	1.800	55.970	0.038	16.368	0.0005	316
	θ	112.108	0.313	0.826	6.966	0.0000	316
	f_w	70.798	32.701	0.324	13.724	0.0000	316
	$PET_{Penman\text{-}Monteith}$	-0.005	72.127	0.046	16.303	0.0001	316
	ET_0	-0.017	88.922	0.325	13.709	0.0000	316
	$PET_{Priestley\text{-}Taylor}$	-0.013	79.603	0.012	16.588	0.0494	316

Table continues on next page.

Appendix Table A9. (continued).

LC Type	Forcing variable	Slope	Intercept	r^2	RSE	P value	N
19. Hawai'i Lowland Mesic Grassland							
	R_{net}	0.930	-56.951	0.470	16.460	0.0000	113
	T	2.945	21.166	0.435	16.999	0.0000	113
	RH	-1.725	203.890	0.212	20.072	0.0000	113
	U	-7.926	92.328	0.109	21.335	0.0003	113
	LAI	16.893	35.649	0.465	16.535	0.0000	113
	f_c	52.464	45.739	0.224	19.911	0.0000	113
	h	-0.284	75.050	0.001	22.588	0.6841	113
	θ	186.822	-34.192	0.637	13.622	0.0000	113
	f_w	-80.903	97.154	0.222	19.942	0.0000	113
	$PET_{Penman\text{-}Monteith}$	0.030	2.695	0.409	17.373	0.0000	113
	ET_0	0.029	26.316	0.632	13.714	0.0000	113
	$PET_{Priestley\text{-}Taylor}$	0.086	-65.663	0.719	11.983	0.0000	113
20. Hawai'i Montane-Subalpine Dry							
	R_{net}	-0.036	45.202	0.002	10.600	0.0000	11363
	T	1.355	24.988	0.080	10.178	0.0000	11363
	RH	0.442	8.997	0.150	9.781	0.0000	11363
	U	1.484	36.586	0.015	10.532	0.0000	11363
	LAI	7.843	37.674	0.050	10.345	0.0000	11363
	f_c	30.103	30.415	0.120	9.955	0.0000	11363
	h	0.892	38.276	0.032	10.441	0.0000	11363
	θ	97.131	-4.067	0.817	4.542	0.0000	11363
	f_w	25.650	34.309	0.110	10.010	0.0000	11363
	$PET_{Penman\text{-}Monteith}$	0.000	40.020	0.000	10.612	0.9706	11363
	ET_0	-0.027	71.720	0.155	9.755	0.0000	11363
	$PET_{Priestley\text{-}Taylor}$	0.003	35.632	0.001	10.605	0.0001	11363
21. Hawai'i Montane-Subalpine Dry							
	R_{net}	-0.351	76.764	0.426	5.155	0.0000	385
	T	1.698	4.922	0.084	6.510	0.0000	385
	RH	0.404	-4.927	0.075	6.542	0.0000	385
	U	-5.705	34.735	0.123	6.370	0.0000	385
	LAI	11.278	21.645	0.268	5.818	0.0000	385
	f_c	27.333	19.758	0.455	5.022	0.0000	385
	h	2.295	21.833	0.135	6.326	0.0000	385
	θ	99.877	-6.688	0.772	3.245	0.0000	385
	f_w	29.464	17.487	0.095	6.470	0.0000	385
	$PET_{Penman\text{-}Monteith}$	0.000	23.725	0.000	6.802	0.8971	385
	ET_0	-0.031	59.429	0.111	6.414	0.0000	385
	$PET_{Priestley\text{-}Taylor}$	-0.032	74.939	0.368	5.407	0.0000	385

Table continues on next page.

Appendix Table A9. (continued).

LC Type	Forcing variable	Slope	Intercept	r^2	RSE	P value	N
22. Hawai'i Montane-Subalpine Mesic							
	R_{net}	-0.139	83.556	0.007	9.758	0.6468	32
	T	-12.715	178.003	0.536	6.669	0.0000	32
	RH	-1.730	175.793	0.296	8.217	0.0013	32
	U	5.810	48.166	0.094	9.322	0.0881	32
	LAI	20.718	38.186	0.830	4.036	0.0000	32
	f_c	-31.077	71.938	0.234	8.570	0.0050	32
	h	-1.537	67.256	0.179	8.874	0.0159	32
	θ	117.792	-13.038	0.829	4.055	0.0000	32
	f_w	-157.340	83.108	0.327	8.036	0.0006	32
	$PET_{Penman\text{-}Monteith}$	-0.003	70.671	0.029	9.649	0.3492	32
	ET_0	0.070	-18.455	0.205	8.730	0.0092	32
	$PET_{Priestley\text{-}Taylor}$	-0.037	117.665	0.062	9.486	0.1704	32
23. Hawai'i Alpine Dwarf-Shrubland							
	R_{net}	-0.033	45.299	0.003	6.044	0.8017	25
	T	-2.238	59.002	0.083	5.797	0.1634	25
	RH	-0.320	57.913	0.058	5.875	0.2473	25
	U	12.520	13.525	0.787	2.791	0.0000	25
	LAI	-19.541	43.039	0.442	4.521	0.0003	25
	f_c	-20.895	44.334	0.207	5.390	0.0223	25
	h	-2.292	41.146	0.035	5.947	0.3727	25
	θ	109.769	-8.759	0.583	3.909	0.0000	25
	f_w	-42.417	42.353	0.104	5.730	0.1163	25
	$PET_{Penman\text{-}Monteith}$	0.000	39.049	0.000	6.052	0.9576	25
	ET_0	0.010	26.069	0.023	5.984	0.4725	25
	$PET_{Priestley\text{-}Taylor}$	-0.006	49.401	0.007	6.032	0.6942	25
24. Hawai'i Dry Cliff							
	R_{net}	0.338	-4.236	0.144	13.887	0.0000	243
	T	-6.810	190.473	0.497	10.649	0.0000	243
	RH	2.097	-120.615	0.436	11.274	0.0000	243
	U	6.185	27.535	0.211	13.333	0.0000	243
	LAI	14.014	23.167	0.617	9.290	0.0000	243
	f_c	36.767	23.123	0.211	13.331	0.0000	243
	h	3.398	30.648	0.498	10.635	0.0000	243
	θ	138.614	-14.624	0.671	8.606	0.0000	243
	f_w	90.352	13.363	0.441	11.221	0.0000	243
	$PET_{Penman\text{-}Monteith}$	0.007	23.406	0.124	14.048	0.0000	243
	ET_0	-0.022	83.035	0.311	12.462	0.0000	243
	$PET_{Priestley\text{-}Taylor}$	0.023	5.338	0.095	14.282	0.0000	243

Table continues on next page.

Appendix Table A9. (continued).

LC Type	Forcing variable	Slope	Intercept	r^2	RSE	P value	N
25. Hawai'i Dry Coastal Strand							
	R_{net}	0.150	5.919	0.030	13.483	0.0020	312
	T	-21.931	549.765	0.442	10.224	0.0000	312
	RH	3.765	-234.198	0.220	12.093	0.0000	312
	U	-0.749	35.405	0.004	13.668	0.2964	312
	LAI	8.324	25.256	0.127	12.796	0.0000	312
	f_c	15.341	26.246	0.054	13.317	0.0000	312
	h	1.510	29.869	0.053	13.326	0.0000	312
	θ	112.072	-0.401	0.820	5.815	0.0000	312
	f_w	217.135	-8.667	0.208	12.188	0.0000	312
	$PET_{Penman\text{-}Monteith}$	0.002	23.613	0.022	13.543	0.0091	312
	ET_0	-0.030	111.509	0.201	12.242	0.0000	312
	$PET_{Priestley\text{-}Taylor}$	0.008	15.606	0.011	13.617	0.0647	312
27*. Hawai'i Subalpine Mesic Shrubland							
	R_{net}	0.449	-3.533	0.095	11.933	0.0000	242
	T	-4.984	105.889	0.062	12.152	0.0001	242
	RH	0.379	32.402	0.011	12.475	0.1043	242
	U	-6.037	72.534	0.056	12.185	0.0002	242
	LAI	17.071	34.132	0.327	10.290	0.0000	242
	f_c	-16.985	62.834	0.059	12.169	0.0001	242
	h	-0.199	58.683	0.002	12.533	0.5267	242
	θ	97.569	-3.581	0.769	6.030	0.0000	242
	f_w	25.119	54.058	0.008	12.492	0.1583	242
	$PET_{Penman\text{-}Monteith}$	-0.005	68.331	0.015	12.449	0.0569	242
	ET_0	-0.004	62.992	0.001	12.539	0.6829	242
	$PET_{Priestley\text{-}Taylor}$	0.043	-3.989	0.079	12.040	0.0000	242
30. Hawaiian Introduced Wetland Veg.-							
	R_{net}	0.837	9.445	0.614	8.251	0.0000	78
	T	9.867	-111.712	0.033	13.059	0.1141	78
	RH	-9.229	766.112	0.105	12.560	0.0038	78
	U	7.369	102.097	0.126	12.410	0.0014	78
	LAI	3.405	106.843	0.128	12.399	0.0013	78
	f_c	-3.317	120.787	0.005	13.243	0.5342	78
	h	0.454	117.429	0.010	13.209	0.3798	78
	θ			0.000			
	f_w	-656.235	236.254	0.104	12.568	0.0040	78
	$PET_{Penman\text{-}Monteith}$	0.011	86.442	0.256	11.451	0.0000	78
	ET_0	0.028	51.359	0.190	11.946	0.0001	78
	$PET_{Priestley\text{-}Taylor}$	0.067	11.070	0.618	8.211	0.0000	78

Table continues on next page.

Appendix Table A9. (continued).

LC Type	Forcing variable	Slope	Intercept	r^2	RSE	P value	N
31. Hawaiian Introduced Dry Forest							
	R_{net}	0.178	15.301	0.040	14.189	0.0000	8440
	T	-0.459	50.424	0.004	14.452	0.0000	8440
	RH	0.180	26.502	0.004	14.450	0.0000	8440
	U	4.522	28.348	0.106	13.693	0.0000	8440
	LAI	15.521	24.323	0.432	10.916	0.0000	8440
	f_c	35.218	17.934	0.121	13.572	0.0000	8440
	h	1.462	33.787	0.083	13.868	0.0000	8440
	θ	121.250	-0.899	0.618	8.945	0.0000	8440
	f_w	8.374	37.798	0.004	14.453	0.0000	8440
	$PET_{Penman-Monteith}$	0.003	29.252	0.058	14.053	0.0000	8440
	ET_0	0.001	39.318	0.000	14.477	0.1268	8440
	$PET_{Priestley-Taylor}$	0.014	16.720	0.036	14.216	0.0000	8440
32. Hawaiian Introduced Wet-Mesic							
	R_{net}	0.571	9.783	0.328	13.051	0.0000	22722
	T	2.347	35.201	0.085	15.232	0.0000	22722
	RH	-0.763	144.075	0.052	15.502	0.0000	22722
	U	7.233	65.720	0.123	14.909	0.0000	22722
	LAI	11.314	46.663	0.435	11.972	0.0000	22722
	f_c	60.539	29.395	0.238	13.901	0.0000	22722
	h	1.580	68.688	0.169	14.513	0.0000	22722
	θ	57.210	50.136	0.109	15.028	0.0000	22722
	f_w	-36.062	96.462	0.062	15.419	0.0000	22722
	$PET_{Penman-Monteith}$	0.013	45.881	0.375	12.584	0.0000	22722
	ET_0	0.012	63.074	0.110	15.020	0.0000	22722
	$PET_{Priestley-Taylor}$	0.047	11.395	0.349	12.844	0.0000	22722
33. Hawaiian Introduced Deciduous							
	R_{net}	0.047	39.072	0.002	16.978	0.0000	17881
	T	-2.585	103.018	0.055	16.518	0.0000	17881
	RH	0.596	0.341	0.020	16.821	0.0000	17881
	U	0.566	43.958	0.001	16.988	0.0001	17881
	LAI	17.774	23.949	0.695	9.380	0.0000	17881
	f_c	72.686	-2.289	0.425	12.889	0.0000	17881
	h	3.880	32.505	0.394	13.226	0.0000	17881
	θ	114.677	1.090	0.669	9.777	0.0000	17881
	f_w	28.193	37.621	0.020	16.825	0.0000	17881
	$PET_{Penman-Monteith}$	0.002	37.657	0.015	16.863	0.0000	17881
	ET_0	-0.007	59.195	0.023	16.795	0.0000	17881
	$PET_{Priestley-Taylor}$	0.003	41.133	0.001	16.987	0.0000	17881

Table continues on next page.

Appendix Table A9. (continued).

LC Type	Forcing variable	Slope	Intercept	r^2	RSE	P value	N
34. Hawaiian Introduced Perennial							
	R_{net}	0.253	12.488	0.076	13.929	0.0000	50958
	T	0.234	40.184	0.004	14.460	0.0000	50958
	RH	0.099	36.759	0.002	14.477	0.0000	50958
	U	1.420	40.540	0.012	14.398	0.0000	50958
	LAI	17.660	21.526	0.514	10.105	0.0000	50958
	f_c	60.269	2.136	0.275	12.339	0.0000	50958
	h	2.729	39.393	0.208	12.897	0.0000	50958
	θ	90.482	5.629	0.646	8.617	0.0000	50958
	f_w	2.710	43.609	0.001	14.484	0.0000	50958
	$PET_{Penman\text{-}Monteith}$	0.005	33.238	0.084	13.864	0.0000	50958
	ET_0	0.001	42.724	0.002	14.473	0.0000	50958
	$PET_{Priestley\text{-}Taylor}$	0.020	14.630	0.077	13.921	0.0000	50958
35. Hawaiian Introduced Evergreen							
	R_{net}	-0.042	80.137	0.003	12.622	0.1538	736
	T	1.121	51.874	0.093	12.036	0.0000	736
	RH	0.663	22.655	0.105	11.955	0.0000	736
	U	4.298	62.530	0.098	12.005	0.0000	736
	LAI	11.349	49.651	0.620	7.794	0.0000	736
	f_c	45.928	36.696	0.300	10.571	0.0000	736
	h	2.103	62.091	0.349	10.201	0.0000	736
	θ	46.673	51.144	0.051	12.312	0.0000	736
	f_w	28.788	64.608	0.094	12.033	0.0000	736
	$PET_{Penman\text{-}Monteith}$	0.004	61.094	0.087	12.076	0.0000	736
	ET_0	0.000	74.545	0.000	12.639	0.9883	736
	$PET_{Priestley\text{-}Taylor}$	0.005	67.091	0.006	12.604	0.0433	736
36. Introduced Coastal Wetland							
	R_{net}	1.456	-113.793	0.147	25.003	0.0003	84
	T	-38.194	1026.445	0.026	26.721	0.1447	84
	RH	31.977	-	0.106	25.593	0.0025	84
	U	-12.132	147.401	0.068	26.134	0.0165	84
	LAI	16.913	76.657	0.235	23.680	0.0000	84
	f_c	-10.396	120.945	0.006	26.995	0.4952	84
	h	5.244	94.418	0.380	21.325	0.0000	84
	θ	129.313	7.593	0.463	19.835	0.0000	84
	f_w	2277.544	-287.943	0.102	25.651	0.0030	84
	$PET_{Penman\text{-}Monteith}$	0.007	91.547	0.023	26.757	0.1671	84
	ET_0	0.059	-32.578	0.021	26.786	0.1884	84
	$PET_{Priestley\text{-}Taylor}$	0.192	-252.543	0.479	19.532	0.0000	84

Table continues on next page.

Appendix Table A9. (continued).

LC Type	Forcing variable	Slope	Intercept	r^2	RSE	P value	N
39. Hawaiian Managed Tree Plantation							
	R_{net}	0.693	-9.690	0.561	9.487	0.0000	3555
	T	3.476	13.294	0.313	11.869	0.0000	3555
	RH	-1.303	186.954	0.137	13.296	0.0000	3555
	U	8.879	58.655	0.268	12.243	0.0000	3555
	LAI	9.716	47.084	0.194	12.849	0.0000	3555
	f_c	31.366	51.249	0.057	13.901	0.0000	3555
	h	1.271	69.596	0.069	13.814	0.0000	3555
	θ	27.304	63.050	0.041	14.021	0.0000	3555
	f_w	-60.722	105.715	0.174	13.007	0.0000	3555
	$PET_{Penman\text{-}Monteith}$	0.012	47.282	0.555	9.548	0.0000	3555
	ET_0	0.024	45.721	0.398	11.107	0.0000	3555
	$PET_{Priestley\text{-}Taylor}$	0.054	-1.869	0.590	9.164	0.0000	3555
40. Open Water							
	R_{net}	0.201	22.631	0.010	38.221	0.0000	2423
	T	-28.152	711.340	0.247	33.340	0.0000	2423
	RH	7.640	-489.889	0.204	34.267	0.0000	2423
	U	11.515	15.705	0.117	36.096	0.0000	2423
	LAI	3.143	50.358	0.005	38.323	0.0006	2423
	f_c	91.748	15.556	0.264	32.966	0.0000	2423
	h	-1.869	59.288	0.098	36.484	0.0000	2423
	θ	147.390	-18.990	0.692	21.329	0.0000	2423
	f_w	464.586	-38.385	0.293	32.303	0.0000	2423
	$PET_{Penman\text{-}Monteith}$	-0.013	100.666	0.212	34.095	0.0000	2423
	ET_0	-0.035	139.549	0.052	37.410	0.0000	2423
	$PET_{Priestley\text{-}Taylor}$	0.032	-4.179	0.027	37.901	0.0000	2423
41. Coastal Kiawe							
	R_{net}	-0.032	53.650	0.001	16.947	0.3960	974
	T	-74.734	1821.601	0.275	14.433	0.0000	974
	RH	-10.099	756.584	0.007	16.893	0.0088	974
	U	3.253	39.699	0.020	16.782	0.0000	974
	LAI	18.651	25.764	0.574	11.061	0.0000	974
	f_c	62.601	11.965	0.392	13.214	0.0000	974
	h	-1.222	53.798	0.036	16.642	0.0000	974
	θ	118.743	13.341	0.393	13.211	0.0000	974
	f_w	-768.847	185.763	0.007	16.894	0.0092	974
	$PET_{Penman\text{-}Monteith}$	-0.002	55.642	0.009	16.874	0.0025	974
	ET_0	0.014	12.430	0.008	16.884	0.0047	974
	$PET_{Priestley\text{-}Taylor}$	-0.002	53.270	0.001	16.948	0.4340	974

Table continues on next page.

Appendix Table A9. (continued).

LC Type	Forcing variable	Slope	Intercept	r^2	RSE	P value	N
42. Agriculture - Sugarcane							
	R_{net}	0.952	-27.118	0.645	6.394	0.0000	2826
	T	-0.222	116.856	0.000	10.736	0.5148	2826
	RH	-0.355	137.856	0.008	10.695	0.0000	2826
	U	10.767	78.533	0.260	9.238	0.0000	2826
	LAI	15.939	68.475	0.284	9.085	0.0000	2826
	f_c	104.839	24.398	0.280	9.109	0.0000	2826
	h	-4.069	119.278	0.043	10.501	0.0000	2826
	θ	154.515	-5.666	0.344	8.697	0.0000	2826
	f_w	-20.250	116.504	0.008	10.693	0.0000	2826
	$PET_{Penman\text{-}Monteith}$	0.009	83.063	0.145	9.931	0.0000	2826
	ET_0	0.009	91.352	0.044	10.500	0.0000	2826
	$PET_{Priestley\text{-}Taylor}$	0.077	-25.159	0.635	6.491	0.0000	2826
43. Agriculture - Pineapple							
	R_{net}	0.372	-7.726	0.625	2.049	0.0000	372
	T	-3.595	120.276	0.332	2.736	0.0000	372
	RH	0.915	-29.912	0.317	2.766	0.0000	372
	U	3.375	33.099	0.126	3.129	0.0000	372
	LAI	3.901	35.329	0.534	2.284	0.0000	372
	f_c	42.769	9.272	0.517	2.326	0.0000	372
	h	1.053	39.940	0.246	2.907	0.0000	372
	θ			0.000			
	f_w	43.996	27.463	0.353	2.693	0.0000	372
	$PET_{Penman\text{-}Monteith}$	0.007	25.083	0.408	2.575	0.0000	372
	ET_0	-0.012	63.658	0.272	2.856	0.0000	372
	$PET_{Priestley\text{-}Taylor}$	0.032	-9.334	0.625	2.051	0.0000	372
44. Agriculture - Macadamia Nut							
	R_{net}	0.771	-25.494	0.615	9.735	0.0000	1581
	T	3.899	-16.855	0.118	14.728	0.0000	1581
	RH	-1.808	207.568	0.330	12.839	0.0000	1581
	U	2.384	61.337	0.005	15.642	0.0036	1581
	LAI	13.656	28.424	0.146	14.495	0.0000	1581
	f_c	147.520	-66.222	0.539	10.651	0.0000	1581
	h	0.760	63.381	0.009	15.616	0.0002	1581
	θ	119.023	0.239	0.740	7.992	0.0000	1581
	f_w	-79.407	92.708	0.322	12.912	0.0000	1581
	$PET_{Penman\text{-}Monteith}$	0.016	33.632	0.278	13.330	0.0000	1581
	ET_0	0.020	32.736	0.262	13.475	0.0000	1581
	$PET_{Priestley\text{-}Taylor}$	0.059	-17.436	0.559	10.419	0.0000	1581

Table continues on next page.

Appendix Table A9. (continued).

LC Type	Forcing variable	Slope	Intercept	r^2	RSE	P value	N
45. Agriculture - Coffee							
	R_{net}	0.777	-16.365	0.775	5.478	0.0000	382
	T	8.112	-92.285	0.663	6.702	0.0000	382
	RH	-2.378	267.827	0.646	6.860	0.0000	382
	U	9.357	60.205	0.806	5.081	0.0000	382
	LAI	7.956	70.200	0.136	10.725	0.0000	382
	f_c	7.947	84.035	0.005	11.507	0.1632	382
	h	-3.156	97.964	0.393	8.989	0.0000	382
	θ	-128.693	196.961	0.178	10.456	0.0000	382
	f_w	-112.261	119.223	0.668	6.652	0.0000	382
	$PET_{Penman\text{-}Monteith}$	0.012	54.087	0.594	7.348	0.0000	382
	ET_0	0.023	39.567	0.735	5.939	0.0000	382
	$PET_{Priestley\text{-}Taylor}$	0.059	-8.586	0.792	5.256	0.0000	382
46. Agriculture - Taro							
	R_{net}	1.165	-18.605	0.612	13.900	0.0000	79
	T	-7.665	313.172	0.049	21.756	0.0510	79
	RH	1.192	53.291	0.014	22.148	0.2993	79
	U	31.247	78.925	0.381	17.551	0.0000	79
	LAI	11.534	102.831	0.221	19.686	0.0000	79
	f_c	91.010	59.664	0.228	19.603	0.0000	79
	h	3.197	118.009	0.283	18.886	0.0000	79
	θ			0.000			
	f_w	69.472	124.518	0.014	22.143	0.2922	79
	$PET_{Penman\text{-}Monteith}$	0.029	53.145	0.635	13.482	0.0000	79
	ET_0	0.036	57.979	0.132	20.784	0.0010	79
	$PET_{Priestley\text{-}Taylor}$	0.098	-21.641	0.610	13.937	0.0000	79

Note that land cover types 26 (Wet-Mesic Coastal Strand), 28 (Hawaiian Introduced Wetland Vegetation-Tree), 29 (Hawaiian Introduced Wetland Vegetation—Shrub), 37 (Introduced Coastal Wetland Vegetation—Shrub), and 38 (Introduced Coastal Wetland Vegetation—Herbaceous) are omitted because of the extremely small number of cells occupied by these land covers. LC Type = Land cover type; RSE = residual standard error; P value = test statistic for significance; N = number of cells; R_{net} = net radiation (W m^{-2}); T = air temperature (°C); RH = relative humidity; U = wind speed (m s^{-1}); LAI = leaf area index (ratio); f_c = vegetation cover fraction (ratio); h = vegetation height (m); θ = available soil moisture (ratio); f_w = canopy wetness fraction (ratio); $PET_{Penman\text{-}Monteith}$ = Penman-Monteith potential evapotranspiration (mm yr^{-1}); ET_0 = grass reference surface potential evapotranspiration (mm yr^{-1}); $PET_{Priestley\text{-}Taylor}$ = Priestley-Taylor potential evapotranspiration (mm yr^{-1}).